# Batch-Microfabricated Miniaturized Planar Arrays of Langmuir Probes for Reentry Plasma Diagnostics and Nanosatellites

by

Ella Suzanne Field

MASSACHUSETTS INSTITUTE
OF TECHNOLOGY
NOV 0 1 2011
LIBRARIES

ARCHIVES

Submitted to the Department of Mechanical Engineering
in partial fulfillment of the requirements for the degree of

Master of Science in Mechanical Engineering

at the

MASSACHUSETTS INSTITUTE OF TECHNOLOGY

September 2011

© Massachusetts Institute of Technology 2011, All Rights Reserved.

Author____________________________________________
Department of Mechanical Engineering
August 5, 2011

Certified by____________________________________________
Luís F. Velásquez-García
Principle Research Scientist of the Microsystems Technology Laboratory
Thesis Supervisor

Certified by____________________________________________
Carol Livermore
Professor of Mechanical Engineering

Accepted by____________________________________________
David E. Hardt
Professor of Mechanical Engineering
Chairman, Committee for Graduate Students

# Batch-Microfabricated Miniaturized Planar Arrays of Langmuir Probes for Reentry Plasma Diagnostics and Nanosatellites

by
Ella Suzanne Field

Submitted to the Department of Mechanical Engineering on August 5, 2011, in partial fulfillment of the requirements for the degree of Master of Science in Mechanical Engineering

## Abstract

One of the most important technical goals in spacecraft design is maintaining the vehicle's integrity under the extreme conditions encountered during reentry to the Earth's atmosphere. When a hypersonic vehicle travels through the atmosphere, a high-density and low-temperature plasma sheath forms around it due to shock heating of the surrounding air and ablation of the heat shield material, which leads to the dissociation and ionization of the background atmosphere. The plasma sheath that surrounds the spacecraft affects the heat transfer to the spacecraft, its aerodynamics, and its capability to communicate.

A thorough knowledge of reentry plasma sheath properties is needed to effectively develop reentry vehicles capable of maintaining structural integrity, aerodynamic stability, and communications during reentry. This thesis reports the preliminary development of a novel plasma diagnostics technology that is modular and that can be used to both monitor the reentry of a spacecraft and serve as a scientific payload in a miniaturized satellite. The technology utilizes planar arrays of batch-fabricated micro Langmuir probes that can be surface-mounted on a reentry vehicle or miniaturized satellite as a sensorial skin to perform time-resolved measurements of the electron temperature and number density of the surrounding plasma sheath. These low-cost, miniaturized plasma sensors align with the paradigm shift in space technology, where missions are visibly smaller, inexpensive, and high performance.

A rough analysis of the reentry heat transfer and plasma data, and our own microfabrication capabilities, led to the design and batch-fabrication process of the micro Langmuir probes. The micro Langmuir probes were constructed by filling-in with electroless nickel 100 $\mu$m-diameter tapered vias machined into a Pyrex substrate, resulting in individually addressable probes having 600 $\mu$m-diameter tips. The highest density arrays that were fabricated consist of 25 probes per 1 cm-square tile, having 1.6 mm separation between probes and square packing, though up to 39 probes per 1 cm-square are possible. The MEMS Langmuir probes were preliminarily tested in a plasma environment similar to atmospheric reentry at MIT's Versatile Toroidal Facility (VTF). The MEMS Langmuir probes were operated as a current-mode triple probe to obtain real-time estimates of the electron temperature, number density, and Debye length. The performance of the MEMS Langmuir probes as a triple probe was benchmarked using a homemade conventional triple Langmuir probe. The plasma parameters measured by the MEMS Langmuir probe were within the range of VTF's reported plasma parameters, but the estimates of the electron density and Debye length were not within the range of the estimates from the conventional triple Langmuir probe using identical plasma. Therefore, we believe that better driving circuitry is needed to increase the signal-to-noise ratio in the MEMS probe data. Nonetheless, these preliminary results suggest that the MEMS Langmuir probe technology has a promising role for conducting reentry plasma diagnostics and serving as nanosatellite scientific payload.

Thesis Supervisor: Luis F. Velasquez Garcia
Title: Principle Research Scientist, Microsystems Technology Laboratories

# Acknowledgements

I owe sincerest gratitude to my thesis supervisor, Dr. Luis Velasquez-Garcia, for giving me the opportunity to succeed in grad school, and for conferring his vast knowledge about microfabrication. I would also like to thank my thesis reviewer, Professor Carol Livermore, for giving me positive reinforcement to solve a challenging problem in a research area that was completely new to me.

This research would not have been possible without the support of technical staff at the Microsystems Technology Laboratory (MTL). In particular, I would like to thank Dennis Ward, Donal Jamieson, Eric Lim, Paul Tierney, and Kurt Broderick for providing training and technical guidance in our microfabrication facilities. I also wish to acknowledge my appreciation for the friendly support and technical advice I received from Professor Tayo Akinwande, and my fellow students Eric Heubel, Stephen Guerrera, Michael Swanwick, Melissa Smith, Dr. Kevin Ryu, Dr. Kerry Cheung, Dan Jang, Vivi Jayanty, and Dr. Annie Wang. Additionally, I owe my sincerest gratitude to Debb Hodges-Pabon for her concern about the well-being of all students at MTL.

I would like to thank Professor Jan Egedal for granting permission to test my devices at MIT's Versatile Toroidal Facility (VTF). I would also like to thank VTF students Ari Le and Arturs Vrublevskis for their willingness to spend many hours operating VTF for my experiments.

I owe a large debt of gratitude to Dan Baker at MIT Lincoln Laboratory. Dan provided access to a gold electroplating tool without charge, and valuable microfabrication advice.

I am grateful for the interest and support that my friends and parents have shown me throughout this entire journey. Most of all, I would like to thank my best friend and fiancé Richard Heller, for always knowing how to make me smile.

Finally, I would like to acknowledge the financial support that made this research possible: NASA grant NNC09CA14C.

## Table of Contents

1 Introduction ---------- 15

1.1 Reentry Plasma Diagnostics: Review of Experimental Investigations ---------- 17

1.2 MEMS Langmuir Probes: Review of Experimental Investigations ---------- 20

1.3 Thesis Objectives and Methodology ---------- 21

1.4 Chapter Summary and Thesis Roadmap ---------- 22

2 Langmuir Probes: Theory, Operation, and Experimental Facility ---------- 23

2.1 Plasma Diagnostics ---------- 23

2.2 Single Langmuir Probe Theory: Thin-Sheath, Collisionless Plasma ---------- 26

2.3 Experimental Facility ---------- 29

2.3.1 Single Langmuir Probe Experimental Investigations ---------- 30

2.4 Triple Langmuir Probe Theory ---------- 34

2.4.1 Current-Mode Operation ---------- 34

2.4.2 Voltage-Mode Operation ---------- 36

2.5 Chapter 2 Summary ---------- 37

3 MEMS Langmuir Probe Design ---------- 39

3.1 Heat Transfer Considerations ---------- 39

3.2 Thermal Expansion Considerations ---------- 43

3.3 Plasma Dynamics Considerations ---------- 46

3.4 Batch-Microfabrication Considerations ---------- 47

3.5 Chapter 3 Summary ---------- 51

4 Fabrication of the MEMS Langmuir Probe Arrays ---------- 53

4.1 Pyrex Substrate Design and Processing ---------- 53

4.2 Via Metallization Process Development ---------- 54

4.2.1 Exploration of Silicon Carbide Coatings for Metalized Vias ---------- 55

4.2.2 Exploration of Electroplated Gold for Metalized Vias ---------- 57

4.2.3 Exploration of Electroless Nickel for Metalized Vias ---------- 60

4.3 Fabrication Process Flow of the MEMS Langmuir Probe Arrays ---------- 62

4.4 Chapter 4 Summary ---------- 64

5 Experimental Characterization of Multiplexed MEMS Langmuir Probes ---------- 65

5.1 Experimental Apparatus ---------- 65

5.1.1 Macro Triple Langmuir Probe Design and Fabrication ---------- 65

5.1.2 MEMS Triple Langmuir Probe Test Fixture and VTF Installation ---------------------------------66
5.1.3 VTF Plasma Parameters and Experimental Considerations ---------------------------------------67
5.1.4 Driving Electronics------------------------------------------------------------------------------68
5.2 Experimental Setup and Procedure------------------------------------------------------------------71
5.3 Data Analysis ----------------------------------------------------------------------------------71
5.3.1 Data Analysis Procedure -------------------------------------------------------------------------71
5.3.2 Results---------------------------------------------------------------------------------------72
5.4 Discussion ------------------------------------------------------------------------------------77
5.5 Chapter 5 summary------------------------------------------------------------------------------78
6 Summary, Conclusions, and Recommendations for Future Work ------------------------------------------79
6.1 Summary of MEMS Langmuir Probe Fabrication and Experimental Setup -------------------------79
6.2 Summary of Experimental Setup, Procedure, Data Analysis, and Results---------------------------79
6.3 Conclusions and Recommendations for Future Work--------------------------------------------------79
7 References------------------------------------------------------------------------------------------81

# Table of Figures

Figure 1.1: The reentry electron number density, calculated from the RAM-CII Langmuir probe data [18]. ------- 18

Figure 1.2: The reentry electron temperature, calculated from the RAM-CII Langmuir probe data [18]. ----------- 19

Figure 2.1: Schematic of the electric potential versus distance from the surface of a negatively biased Langmuir probe. The bias voltage is $V_0$, the plasma potential is approximately $V_s$, and the sheath thickness is $x_s$ [31]. ------- 24

Figure 2.2: Characteristic Debye lengths of various plasmas versus plasma electron temperature and number density [21]. ------- 24

Figure 2.3: Typical schematic of a single Langmuir probe experimental setup. The bias voltage to the probe is supplied by $V_{bias}$, and probe current is measured as a voltage across the resistor $R$ by $V_R$ [32]. ------- 25

Figure 2.4: Langmuir probe operating regimes in terms of probe diameter $r_p$, mean free path $l$, and Debye length $\lambda_D$ for cylindrical probes [34]. ------- 26

Figure 2.5: Schematic I-V characteristics of a single Langmuir probe in the thin-sheath collisionless operating regime. The I-V characteristics have three distinct regions: Region I is dominated by ion current, Region III is dominated by electron current, and Region II is a transition region where the net current is a combination of ion and electron current. $V_f$ is the floating potential, and $V_p$ is the plasma potential [34]. 27

Figure 2.6: The anatomy of a tokamak, illustrating the magnetic confinement of plasma within a vacuum vessel. ------- 29

Figure 2.7: (A) The Versatile Toroidal Facility (VTF) at MIT has an outer diameter of 3.5 m. (B) The author is pictured beside VTF to provide a sense of scale. ------- 30

Figure 2.8: Photograph of the single Langmuir probe constructed in-house. The probe tip consisted of a 1 mm-diameter stainless steel hypodermic needle soldered to a thin copper wire and fed through alumina and stainless steel housing. ------- 31

Figure 2.9: An image of the Langmuir probe in plasma within VTF. ------- 31

Figure 2.10: Circuitry to acquire digitized voltage across $R_2$ from the single Langmuir probe operating in plasma at VTF. The voltage across $R_2$ was converted into probe current using equation 2.10. The bias voltage $V_{bias}$ was supplied to the probe using a power supply. ------- 32

Figure 2.11: Voltage across $R_2$ vs. time during one of the 20 ms plasma shots. The single Langmuir probe was biased at -90 V. ------- 32

Figure 2.12: The I-V characteristics of a single Langmuir probe operated in argon plasma at VTF. The electron current is shown as positive current. At least 5 current measurements were taken at each applied voltage. The average ion saturation current is approximately -0.012 Amps, shown at a value of -90 V. ------- 33

Figure 2.13: Triple Langmuir probe configuration in current-mode operation [33]. ------- 35

Figure 2.14: Triple Langmuir probe configuration in voltage-mode operation [33]. ------- 37

Figure 3.1: Diagram of transient heat flux into semi-infinite solid. ------- 39

Figure 3.2: Results from the reentry heat transfer analysis: (A) Surface temperature vs. time due to constant peak reentry heat flux measured on the leading edge of the Space Shuttle's wing; (B) Surface temperature vs. time due to average constant heat flux on the windward side of the Space Shuttle. ------- 41

Figure 3.3: Results from the reentry heat transfer model, where a cooling system was implemented to prevent materials from melting: (A) Surface temperature vs. time due to constant peak reentry heat flux measured on the leading edge of the Space Shuttle's wing; (B) Surface temperature vs. time due to average constant heat flux on the windward side of the Space Shuttle. ------- 42

Figure 3.4: The linear expansion of MEMS Langmuir probe materials during the reentry conditions modeled in Figure 3.3. ---- 44

Figure 3.5: RAM-C Experimental Reentry Vehicle with Langmuir Probes in Aft Flow Field [18]. ---- 47

Figure 3.6: The electron Debye length calculated from the RAM-CII Langmuir probe reentry data [18]. ---- 47

Figure 3.7: MEMS Langmuir probe design concept showing 9 holes in an electrically insulating flat plate that have been filled in with an electrically conductive material. Each filled hole is an individual MEMS Langmuir probe. ---- 48

Figure 4.1: Schematic cross section of a Langmuir probe array in plasma with pogo pin electrical connectors on the opposite side. The taper of the vias facilitates the deposition of the seed metal into the vias. ---- 53

Figure 4.2: Pyrex wafer after die-sawing. As reference, each die is a square, 1 cm-wide. The dies appear attached to each other because the wafer was attached to an adhesive backing during the die-sawing process. ---- 54

Figure 4.3: Aluminum shadow mask for sputtering titanium and gold into the Pyrex vias (A). The shadow mask worked together with a fastening plate (B). ---- 55

Figure 4.4: Cross section of the concept of using a shadow mask to fill in vias with a metal seed. ---- 55

Figure 4.5: Doped silicon carbide film could be used to protect the metallization against the harsh reentry plasma. ---- 56

Figure 4.6: Doped and un-doped SiC films were deposited at various thicknesses and annealed at various temperatures for 30 minutes. A total of 18 samples were processed. ---- 56

Figure 4.7: SEM of electroplated gold inside a via as seen from the plasma side from the first electroplating experiment, demonstrating the conformality of the deposited film. ---- 58

Figure 4.8: (A) Sample used in the second experiment before plating. (B) Sample used in the second experiment after plating and removal of the electroplating tape. Electroplating occurred in some of the areas masked by the tape. ---- 58

Figure 4.9: Dies with exposed titanium film due to etching of the gold electroplating seed layer. ---- 59

Figure 4.10: SEM of the gold metallization inside a via produced by the fourth electroplating experiment. The rough appearance of the gold is a result of the depletion of gold in the electroplating solution. ---- 60

Figure 4.11: Laboratory setup of electroless nickel plating process from Caswell, Inc. ---- 61

Figure 4.12: SEM of a 200 μm-diameter metalized via as seen from the plasma side of the probe. The via was partially filled with electroplated gold from the fourth gold electroplating experiment, and then partially filled with electroless nickel deposition. ---- 62

Figure 4.13: Process flow to fabricate arrays of MEMS Langmuir probes (A) Ultrasonic drilling of the Pyrex wafer; (B) Transfer of die-saw lines using contact lithography; (C) Die-sawing of Pyrex wafer; (D) Dies cleaned using a piranha bath; (E) Sputtered Ti/Au film stack is deposited into the vias using a shadow mask; (F) Electroless nickel plating of vias. ---- 63

Figure 4.14: Various array sizes of MEMS Langmuir probes. ---- 63

Figure 4.15: SEM of the plasma side view of a 600-μm diameter MEMS Langmuir probe from a 2×2 array containing 100 μm- diameter vias. The smudge on the nickel probe is residue from graphite tape that was used for taking other SEMs. ---- 64

Figure 4.16: Cross section view of a MEMS Langmuir probe part of a 2×2 probe array. The titanium adhesion layer remained attached to the electroless nickel on the pogo-pin side of the probe when the die was broken to create this cross section view. The titanium adhesion layer is the lighter colored inner circle on the pogo pin side. ---- 64

**Figure 5.1:** The primary components of the conventional triple Langmuir probe. ---------- 65

**Figure 5.2:** Completed conventional triple Langmuir probe (top), and detail of the tungsten probe tips (bottom). ---------- 66

**Figure 5.3:** The test fixture for the MEMS Langmuir probes. ---------- 66

**Figure 5.4:** (A) Schematic of the MEMS Langmuir probe test fixture; (B) Cross-section of the MEMS probe test fixture. ---------- 67

**Figure 5.5:** (A) The brown vespel pogo pin fixture and gold pogo pins are shown within the die holder before the die was installed; (B) The MEMS die installed into the die holder and secured with the faceplate. ---------- 67

**Figure 5.6:** Schematic of the circuit used to drive the conventional and MEMS triple Langmuir probes at VTF. -- 69

**Figure 5.7:** Conventional triple probe raw voltage data corresponding to each value of $R_1$=$R_6$ in the driving circuitry. ---------- 73

**Figure 5.8:** MEMS probe raw voltage data corresponding to each value of $R_1$=$R_6$ in the driving circuitry. Each plot contains data from 5 plasma shots, except for the noise plot on the lower right, which contains 1 shot. --- 73

**Figure 5.9:** Conventional probe currents $I_1$, $I_2$, and $I_3$, corresponding to each value of $R_1$=$R_6$ in the driving circuitry. Each plot contains data from 5 plasma shots. ---------- 74

**Figure 5.10:** MEMS probe currents $I_1$, $I_2$, and $I_3$, corresponding to each value of $R_1$=$R_6$ in the driving circuitry. Each plot contains data from 5 plasma shots. ---------- 74

**Figure 5.11:** The average and standard deviation of the electron temperature of five plasma shots from the conventional probe and MEMS probe data, corresponding to $R_1$=$R_6$=10k Ω in the driving circuitry. ---------- 76

**Figure 5.12:** The average and standard deviation of the electron temperature of five plasma shots from the conventional probe and MEMS probe data, corresponding to $R_1$=$R_6$=10k Ω in the driving circuitry. ---------- 76

**Figure 5.13:** The average and standard deviation of the electron Debye length of five plasma shots from the conventional probe and MEMS probe data, corresponding to $R_1$=$R_6$=10k Ω in the driving circuitry. ---------- 77

## List of Tables

Table 3.1: Thermophysical Constants Utilized in Heat Transfer Model ........ 40

Table 3.2: Time Before Melting During Reentry ........ 41

Table 3.3: Reentry Heat Flux Tolerance and Cooling System Requirements ........ 42

Table 3.4: Coefficients of Thermal Expansion ........ 43

Table 3.5: Net Strain Between Candidate MEMS Langmuir Probe Materials ........ 44

Table 3.6: Tensile Strength, Compressive Strength, Young's Modulus, and Failure Strains ........ 45

Table 3.7: Structural Failure due to Thermal Mismatch from Peak Reentry Heat Flux ........ 45

Table 3.8: Materials and Geometry Selections of the MEMS Langmuir Probes ........ 51

Table 4.1: Components of Electroless Nickel Solution ........ 61

Table 5.1: Comparison of Conventional and MEMS Triple Probe Dimensions ........ 66

Table 5.2: Estimation of Ion Saturation Current Collected by the Conventional and MEMS Triple Probes ........ 68

Table 5.3: Applied current-to-measured current ratio for $I_2$ and $I_3$. Combinations where the measured current is within 10% of the applied current are shown in black ........ 70

Table 5.4: Average Plasma Parameters from the 10k Ω Data ........ 77

# 1 Introduction

One of the most important technical goals in spacecraft design is maintaining the vehicle's integrity under the extreme conditions encountered during reentry to the Earth's atmosphere [1]. When a hypersonic vehicle travels through the atmosphere, a high-density and low-temperature plasma sheath forms around it due to shock heating of the surrounding air and ablation of the heat shield material, which leads to the dissociation and ionization of the background atmosphere [2]. The plasma sheath that surrounds the spacecraft affects the heat transfer to the spacecraft, its aerodynamics, and its capability to communicate.

The reentry plasma sheath can induce a communications blackout. Signal attenuation in plasma is caused by the existence of a cut-off frequency (i.e., plasma frequency) due to the presence of free electrons in the plasma. The communications blackout occurs when the plasma frequency is greater than the radio wave frequency [3]. A communications blackout poses a major concern because it causes the loss of voice communication, data telemetry, and any kind of support/feedback provided to the spacecraft by mission control on the ground. In addition, the reentry plasma sheath could eliminate electronic countermeasure capabilities during the reentry of military ballistic missile payloads such as Lockheed Martin's Trident II D5 intercontinental ballistic missile (ICBM), and Boeing's LGM-30G Minuteman III ICBM [4,5,6].

The communications blackout phenomena reached public awareness in the 1960's when manned space missions first commenced [7]. A notable cry for concern was raised during Apollo 13's failed attempt to land on the moon. During the return to Earth, NASA engineers were unsure whether the Apollo capsule was reentering the atmosphere at the correct angle. The communications blackout persisted longer than expected, and during this time it was not possible for mission control to assess what was happening onboard the capsule, including the status of the crew [3]. However, a communications blackout can cause far more serious problems. An example of a disastrous reentry due to a communications blackout occurred at the end of the Genesis mission in 2004. Upon reentry, a sensor failure prevented the drogue parachute from opening. Therefore, the capsule could not decelerate and it crashed into the Utah desert. This failure could have been mitigated by mission control if they had been in constant contact with the vehicle throughout reentry [3].

The communications blackout problem was solved for NASA's Space Shuttle Orbiter program, a reusable manned spacecraft for spaceflight into near-Earth orbit. Due to its complex geometry, the Space Shuttle was not fully encapsulated by a plasma sheath during reentry, and thus communications antennas were strategically installed in areas that were relatively plasma-free. Radio communications during reentry were maintained using the Tracking and Data Relay Satellite (TDRS) system [2]. Otherwise, the Space Shuttle would have endured approximately 16 minutes of communications blackout [3]. However, with the retirement of the shuttles in 2011 and the return to Apollo-like capsule reentry vehicles, communications blackouts remain a pressing problem.

Besides the problem of the communications blackout, the reentry plasma sheath can threaten the aerodynamic stability and structural integrity of a vehicle due to heat transfer. A near-disaster due to heat transfer from the reentry plasma sheath was encountered by the Soyuz 5 capsule in 1969. During the reentry procedure, the service module of the Soyuz 5 failed to separate after retrofire, but by that point it was too late to abort the maneuver. When the Soyuz 5 began aerobraking in the higher altitudes of the atmosphere, the combined spacecraft arranged itself in the most aerodynamically stable position, i.e., nose forward. Thus, the Soyuz 5 capsule was facing directly into the hot plasma stream with only its light metal entry hatch at the front to protect it. The gaskets sealing the hatch began to burn, filling the passenger compartment with dangerous fumes. The deceleration, while normal for reentry, pulled the cosmonaut Boris Volynov outward against his harness rather than against the padded seat. Fortunately, as the thermal and aerodynamic stresses on the combined craft increased, struts between the Soyuz 5 capsule and service module broke off or burned through before the hatch failed. Then, the Soyuz 5 capsule immediately righted itself once the service module was removed, with the nose backward and the heat shield forward to handle the brunt of reentry. Unfortunately, the reentry problems did not stop here. The capsule's parachute lines tangled and the soft-landing rockets failed, resulting in a hard landing which remarkably only broke Volynov's teeth. The capsule landed in the Ural Mountains 2 km southwest of Kustani, near Orenburg, Russia, far from its target landing site in Kazakhstan. The local temperature was −38 °C. Knowing that many hours would pass before rescue teams could reach him, Volynov abandoned the capsule and hiked several kilometers to seek shelter at a local peasant's house [8].

The Space Shuttle Columbia STS-107 reentry disaster on February 1, 2003 is a crucial example of how heat transfer from the reentry plasma sheath can destroy the structural integrity of a reentry vehicle. The loss of Columbia began as a result of damage incurred by its thermal protection system (TPS) on the leading edge of its left wing when a piece of foam insulation the size of a small briefcase broke off from the Space Shuttle external tank (the main propellant tank) due to the aerodynamic forces during launch. The Space Shuttle's TPS shields the spacecraft from the heat generated during atmospheric reentry. However, the breach in Columbia's TPS allowed superheated air to penetrate through the leading edge insulation on the left wing during reentry, progressively melting the wing's aluminum structure, until increasing aerodynamic forces caused loss of control, failure of the wing, and ultimately the break-up of Columbia over the southern United States. Unfortunately, this break-up occurred during a flight regime in which, given the design of the Space Shuttle, there was no possibility for the crew to survive [9].

A thorough knowledge of reentry plasma sheath properties is needed to effectively develop reentry vehicles capable of maintaining structural integrity, aerodynamic stability, and communications during reentry. However, the fundamental processes that control the reentry plasma sheath are still not well understood. Furthermore, the conditions of the plasma sheath rapidly change throughout reentry, which introduce additional complications. Analytical approaches alone are not enough to gain a complete understanding of the plasma sheath. For example, the electron density profile is highly dependent on the angle of attack and the precise shape of the vehicle, and becomes extremely challenging to compute for complex shapes. Therefore, instrumentation must be developed to measure in real-time the transient properties of the plasma sheath during reentry, in as many locations as possible on the spacecraft [6].

In a standard space mission, low-cost instrumentation has not been an obvious necessity because space missions usually cost about US$ 10,000 per pound of payload. For the case of the Space Shuttle, the cost of each mission is about US$ 450 million when all expenses are considered [10]. However, using batch-fabrication technology to manufacture miniaturized high-performance and modular plasma sensors with tight specs is very desirable as it can be used to implement a 'sensorial skin' that blends with the spacecraft body without changing its aerodynamic attributes. This can certainly be achieved through the utilization of microfabrication techniques. In addition, low-cost high-performance instrumentation aligns with a new paradigm for space missions where the cost of a mission becomes mainstream affordable by developing mass-fabricated miniaturized & autonomous hardware.

A very exciting research trend in spacecraft design for affordable space missions is the development of satellites having wet masses on the order of a few tens of kilograms and below [11] – orders of magnitude smaller and lighter than the typical 500-kg satellites used in communications or weather monitoring. The motivation for developing miniaturized satellites is driven by the mission costs:

bulky satellites are more expensive to launch than light satellites because they require more powerful rockets that consume visibly more propellant. On the one hand, a standard satellite costs about US$ 100 million and requires a dedicated rocket launch that costs about US$ 50 million. On the other hand, miniaturized satellites can be made at a tiny fraction of the cost of a standard satellite, and groups of miniaturized satellites can share a standard rocket, similar to the way tens to hundreds of passengers share a commercial airplane to arrive at their destination while paying a small fraction of the operation costs. In addition, miniaturized spacecraft are also compatible with mass production, which would further reduce mission costs and result in tighter specs, igniting a space revolution with many commercial applications.

Spacecraft miniaturization will also make possible missions that cannot be accomplished by a standard satellite. For example, a constellation of miniaturized spacecraft can be used to chart regions of space [12], or as a phased antenna array for high-resolution radar observation of objects of the Earth's surface [13]; in addition, a miniaturized satellite can be used to inspect and repair in-orbit larger satellites at a fraction of the cost that a standard repair mission would entail. The use of spacecraft constellations will also benefit the missions by providing hardware redundancy, which results in increased mission reliability. However, miniaturized spacecraft require radically new approaches at the system level as well as the component level to develop spacecraft that are as capable as the macro counterparts. In particular, scientific payloads compatible to miniaturized satellites need to be developed. Miniaturized plasma sensors can be used to monitor the plasma sheath surrounding the satellite, similarly to the sensorial skin concept that was discussed for macro-spacecraft such as manned reentry capsules, or as a scientific instrument to locally characterize the Earth's ionosphere [14]. The use of microfabrication technologies allows the development of plasma sensors at low cost with tight specs that are light and small, in resonance with the idea of low-cost/mass-production of spacecraft hardware.

This thesis reports the development of a novel plasma diagnostics technology that is modular and that can be used to both monitor the reentry of a spacecraft and serve as a scientific payload in a miniaturized satellite. The technology utilizes planar arrays of batch-fabricated micro Langmuir probes. These sensing tiles can be surface-mounted to perform time-resolved measurements of the electron temperature and number density of the reentry plasma sheath across the entire surface of the reentry vehicle. Also, the miniaturized probes can provide plasma diagnostics of the miniaturized spacecraft surroundings or be used as a scientific instrument to characterize the Earth's ionosphere. The technology is indeed applicable to characterizing plasmas not just in space, but in almost in any plasma source. However, the focus of this thesis relies upon the particular case of demonstrating low-cost, miniaturized plasma sensors for space applications to contribute to the paradigm shift in space technology, where missions are visibly smaller, inexpensive, and high performance. The remainder of this chapter consists of a review of reentry plasma diagnostics and Langmuir probes, highlighting the necessary areas of improvement where the proposed miniaturized Langmuir probes could help enhance the current state of the art. Accordingly, the objectives of this thesis were established, and have been listed towards the end of this chapter. Finally, a thesis roadmap was presented to briefly introduce the topics of the remaining chapters.

## 1.1 Reentry Plasma Diagnostics: Review of Experimental Investigations

Langmuir probes are relatively simple to construct and can be operated to measure the electron temperature and number density of a plasma. The use of Langmuir probes for plasma diagnostics in space began soon after World War II, when they were implemented on V-2 rockets. Over the years, Langmuir probes have been used extensively on rockets, satellites, and reentry vehicles [15,16,17]. In most cases, the Langmuir probes were mounted on fins, protruding symmetrically. Unfortunately, the fins were generally required to retract at an altitude of about 60 km because the severe heating that occurs at lower altitude would result in non-symmetrical burn-up of the probes, and because of aerodynamic instability concerns [6]. Therefore, while Langmuir probes have been useful for characterizing the plasma in the early stages of reentry, they have not been used at the lower altitudes where the most severe plasma conditions occur. Nonetheless, if the Langmuir probes were flush-mounted to the spacecraft's exterior, they would be more likely to survive reentry [6] and they would not modify the flow field, leaving unaffected the heat transfer and aerodynamic properties of the spacecraft. The downside of flush-mounted probes is that they would only determine the plasma properties at the surface of the reentry vehicle. Estimates of the properties of the plasma sheath further away from the spacecraft's surface could be extrapolated, but it may not be possible to generate these estimates with a high degree of accuracy. Consequently, non-invasive methods such as antenna impedance measurements, spectroscopy, and microwave interferometry would need to be included along with the flush-mounted Langmuir probes to obtain a more complete understanding of the reentry plasma sheath.

The plasma data from the RAM-CII reentry vehicle is often considered the benchmark for other reentry plasma experiments and simulations. The RAM-CII had eight Langmuir probes that were mounted on an aerodynamic fin to measure the ion densities in the flow field to a distance of approximately 0.07 m from the reentry vehicle [6]. The probe fin was retracted at an altitude of approximately 55 km due to severe heating. The plasma temperature and number density computed from the RAM-CII Langmuir probe data is presented in Figures 1.1 and 1.2.

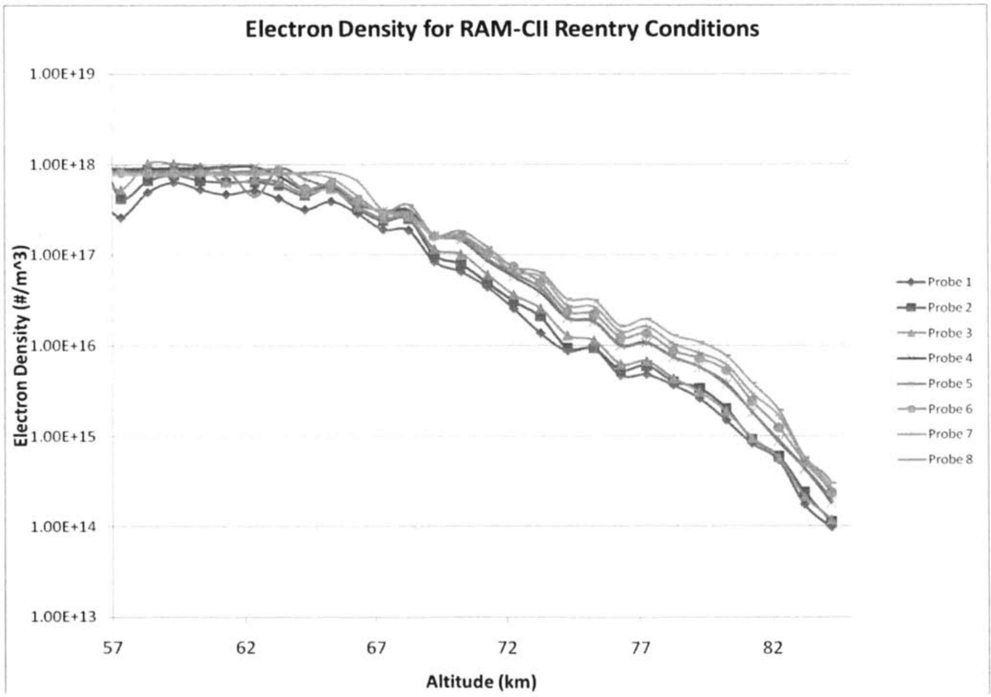

**Figure 1.1: The reentry electron number density, calculated from the RAM-CII Langmuir probe data [18].**

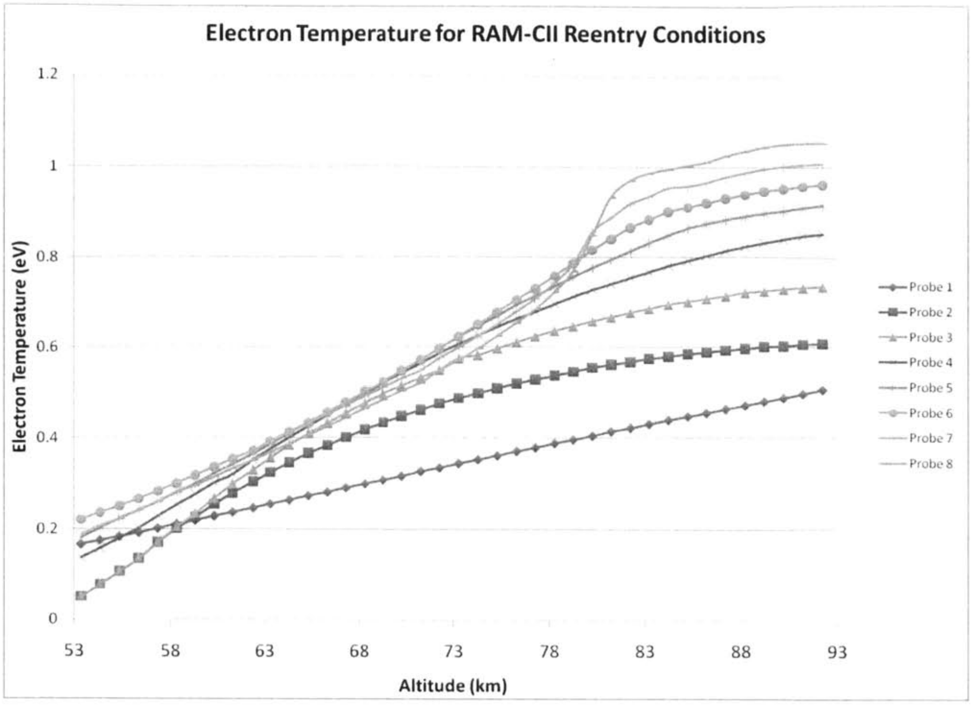

**Figure 1.2: The reentry electron temperature, calculated from the RAM-CII Langmuir probe data [18].**

During the Mercury and Gemini missions, estimates of electron number density were made, assuming a pure air plasma environment to compensate for the lack of experimental data from altitudes below 60 km. Unfortunately, the results showed no correlation with signal attenuation measurements that were recorded below 60 km. This result suggested that a pure-air plasma was not responsible for the observed reentry signal attenuation at the lower altitudes. It was therefore necessary to consider the possible influence of the ablation products of the heat shield. In general, many reentry vehicles are constructed with a heat shield that is meant to partially ablate during reentry, and the ablation products have been known to ionize easily. In this case, the heat flux to the surface of the reentry vehicle is dissipated in ablating the surface while transmitting zero heat to the interior of the spacecraft; this physical phenomenon is described by Crocco's relationship [19]. Better estimates indicated that the ionized ablation products have a significant impact on reentry communications, which was corroborated by an experiment performed during the reentry of the Gemini GT-3 capsule. Water was injected into the plasma flow field, which resulted in large decreases in electron temperature and number density, and created a window at the antenna locations for RF transmissions [6].

During the apogee of the space race, atmospheric reentry plasmas were extensively studied both in laboratories and around reentry vehicles. However, most of the laboratory work concentrated on simulating thermal and chemical phenomena that occur on the reentry vehicle's surface in order to test heat shields [2]. Until recently, not much work had been done to simulate actual plasma temperatures or densities encountered during atmospheric reentry. One example of simulating the temperatures and densities of reentry was developed by K.M. Lemmer, et al [2]. A 150 mm diameter helicon source at the University of Michigan Plasmadynamics and Electric Propulsion Laboratory (PEPL) was setup to simulate atmospheric reentry plasma densities and temperatures in a laboratory setting. They operated the helicon source with argon gas at a background pressure of 0.6 mTorr, and used a commercial RF-compensated Langmuir probe to measure ion density and electron temperature in a region downstream of the helicon source, where conditions created were similar to those found during hypersonic flight within the atmosphere. Langmuir probe measurements were taken with and without the presence of a 450 mm wide by 550 mm long dielectric surface downstream in the horizontal plane, in order to simulate a reentry vehicle surrounded by plasma. They found that the presence of a surface downstream of the helicon source lowered the downstream plasma electron density range from 1.7 x $10^{17}$ and 3.3 x $10^{17}$ $m^{-3}$ down to 0.55 x $10^{17}$ and 1.3 x $10^{17}$ $m^{-3}$. In addition, the peak plasma potential decreased from 65 to 55 V, while the electron temperature remained unchanged between 1.5 and 6.5 eV. Their results corroborate earlier numerical models that predicted that the shape of a reentry vehicle can have a significant effect on the density of the surrounding plasma sheath, but not the temperature, which is an important finding to understand how the reentry plasma would attenuate RF signals [1,20].

In general, the results obtained from reentry plasma diagnostics and simulations have been very useful, but less than sufficient, because the problem of the communications blackout still persists, and reentry vehicles have been damaged or destroyed due to aerodynamic instabilities and heat transfer effects. Instruments for performing in-flight measurements of the reentry plasma parameters are still in an elementary stage of development. Also, the performance of surface-mounted, microfabricated sensors in reentry conditions has yet to be tested, and could provide a wealth of data spanning a large area on the surface of a reentry vehicle. This is where it is believed that surface-mounted microfabricated Langmuir probes can make a great contribution.

However, it is important to note that the utility of Langmuir probe technology is tremendous not just in space, but on Earth as well. Plasmas underline the US$ 250 billion semiconductor processing industry, bolster the US$ 2 trillion telecommunications industry, and are becoming ever more valuable for lighting, medicine and consumer products [21]. Fortunately, Langmuir probes can be adapted to measure almost any type of plasma. Hence, the discussion about applications to reentry plasma diagnostics and miniaturized satellites merely scratches the surface of the potential utility of the microfabricated Langmuir probes described in this thesis.

## 1.2 MEMS Langmuir Probes: Review of Experimental Investigations

To the best of the knowledge of this author, microelectromechanical systems (MEMS), i.e. microfabricated devices, have not been applied to the problem of reentry plasma diagnostics. This is clearly an unfulfilled opportunity because the implementation of MEMS Langmuir probes could offer several advantages over other approaches. First, the small size of MEMS Langmuir probes implies that they would be less likely to disturb the plasma, and that they would be able to resolve plasmas with very small Debye Lengths. Second, MEMS Langmuir probes can be monolithically constructed in planar arrays (tiles) that could be incorporated onto the exterior surface of a reentry vehicle, acting as a sensorial skin; the monolithic nature of the probes eliminates the problems related with array integration. Third, microfabrication technologies can yield low-cost mass-produced devices with very tight specs; the fabrication of MEMS Langmuir probes follows a change in paradigm for the space industry by making missions mainstream affordable. Low-cost missions can be achieved by mass-producing space hardware and by miniaturizing the spacecraft whenever possible (for example in satellites) to then share the takeoff of a standard rocket. MEMS technologies have been used to develop proof-of-concept spacecraft components such as inertial guidance [22], scientific instruments (X-rays spectrometer [23], back-up vacuum pumps [24]), actuators for height and angle control [25], and thrusters for low-Isp [26] and high-Isp missions [27,28]. MEMS could certainly provide a solution for miniaturized low-cost plasma diagnostics.

At present, the fabrication of MEMS Langmuir probes has been reported in two publications, both by Pribyl et al from UCLA [29]. Linear arrays of probes were fabricated primarily using polyimide and gold as structural materials. The probe tips ranged from 8 to 20 μm wide by 2.5 μm thick, and were spaced between 20 and 52 μm apart. The small signals generated by the probes necessitated the use of a local amplifier for each probe to assist data collection. The amplifiers, Texas Instruments THS4303, provided a voltage gain of 10 V and a flat frequency response from approximately 5 MHz to 18 GHz. The probes were tested in plasma at UCLA's Large Plasma Device machine (LAPD). In LAPD, the plasma electron Debye length varied from 20 to 200 $\mu$m, hence the probes were smaller than the electron Debye length and should not disturb the plasma. The probes successfully measured the plasma's electric field, but additional measurements, including electron temperature and number density, have yet to be reported.

A clear disadvantage of the MEMS probes reported by Pribyl et al is that the probes were not designed to operate in high temperature environments such as spacecraft reentry. For example, the peak temperature experienced by the Space Shuttle Orbiter during reentry is approximately 1650 $^0$C [30]. However, polyimide has a glass transition temperature of 350 $^0$C, and begins to physically degrade at 620 $^0$C. Gold has a melting temperature of approximately 1064 $^0$C., but in a reentry scenario, by the time the gold melts, the physical integrity of the probe would have been compromised as the insulating polyimide material between the probes would have become conductive through carbonization. More resilient materials such as tungsten and silicon carbide should be used to fabricate probes compatible with reentry conditions. These materials have melting temperatures of about 3422 $^0$C and 2700 $^0$C, respectively, which are less than the 1650 $^0$C peak temperature experience by the Space Shuttle Orbiter.

Another desirable improvement would involve the fabrication of MEMS probes in level, planar arrays (like tiles), unlike the reported linear arrays that resembled cantilever beams. Planar arrays could be flush-mounted to the exterior surface of a spacecraft, functioning as a sensorial skin to collect data over a widespread area. This flat configuration would also help eliminate the aerodynamic disturbances that protruding sensors may induce due to being incinerated by the high temperatures. In addition, a linear array of probes has a higher surface to volume ratio that would make the probes visibly less resistant to ablation.

## 1.3 Thesis Objectives and Methodology

The primary goal of this thesis was to design, develop, and test a planar array of batch-fabricated MEMS Langmuir probes for operation in high-temperature conditions such as spacecraft reentry, for which time resolved measurements of the electron temperature and number density could be determined. The knowledge created in demonstrating MEMS Langmuir probes that can measure reentry conditions can certainly be leveraged to implement a scientific payload for a miniaturized spacecraft. The specific goals of this thesis are:

- Demonstrate MEMS Langmuir probe technology
    - Establish design requirements for MEMS Langmuir probes
    - Design and fabricate MEMS Langmuir probes
    - Design and construct an experimental setup for testing the MEMS Langmuir probes in plasma
    - Establish procedures for testing, and related tasks
    - Acquire test data from MEMS Langmuir probes operating in plasma
- Analyze the test results of the MEMS Langmuir probes, and conduct an error analysis
    - Design, construct and test a macro Langmuir probe to benchmark the performance of the MEMS probes
    - Estimate the effect of errors and uncertainties on the MEMS probes results

  - Assess the correspondence between theoretical models and data including a quantitative explanation of any discrepancies.
- Propose recommendations for future work
  - Describe additional applications for developed MEMS Langmuir probes
  - Suggest methods to improve the current MEMS fabrication process and experimental setup

## 1.4 Chapter Summary and Thesis Roadmap

Despite many developments in the areas of reentry plasma modeling, simulation, and diagnostics, many reentry vehicles are still affected by critical problems such as communications blackouts, heat transfer effects, and aerodynamic instabilities. A literature review of reentry plasma diagnostics revealed that the reentry plasma sheath could be better understood through the implementation of surface-mounted Langmuir probes, having the ability to perform measurements in many locations during harsh reentry conditions. Planar arrays of high-temperature resistant MEMS Langmuir probes were proposed as a solution to perform plasma diagnostics during reentry. The planar construction of the probes would allow them to be blended onto the outer surface of a reentry vehicle in many locations, as a sensorial skin. This plasma sensor technology is compatible with low-cost mass-production of hardware with tight specs, which corresponds with the new paradigm to make space missions mainstream affordable. As an extension of this idea, miniaturized spacecraft could be developed to visibly reduce the hardware costs and the lunch costs. The probes that were developed in this thesis can be used in miniaturized spacecraft, either as a constitutive element of a sensorial skin for reentry, similarly to the macro-spacecraft case, or as a scientific instrument to characterize the spacecraft surroundings. Following this proposal, the objectives of this thesis were established. The subsequent chapters in this thesis include the following topics:

- Chapter 2 introduces the theory of operation of Langmuir probes as single and triple probes.
- Chapter 3 concerns the selection of the design requirements of the MEMS Langmuir probes, based on considerations such as reentry temperature analysis, reentry plasma Debye length, and microfabrication constraints.
- Chapter 4 describes the fabrication of the MEMS Langmuir probes.
- Chapter 5 describes the apparatus we used in the characterization of the devices (including the fabrication and validation of a macro Langmuir probe that was used to benchmark the MEMS probes), presents and interprets MEMS Langmuir probes data as single probes and triple probes, and provides quantitative explanations of the differences between models and data.
- Chapter 6 provides a summary and conclusion of the thesis work, in addition to recommendations for future work.

# 2 Langmuir Probes: Theory, Operation, and Experimental Facility

This chapter provides a general overview on Langmuir probe plasma diagnostics. The principles and equations presented in this chapter allow an understanding of how to design and operate Langmuir probes, as well as how to analyze and interpret the MEMS Langmuir probe data. In addition, this chapter presents an overview of the experimental facility that was used to test the MEMS Langmuir probes.

## 2.1 Plasma Diagnostics

Plasma is generally defined as a state of matter similar to a gas in which a portion of its constituents is charged particles, typically due to heating. The presence of charge carriers, i.e. positive ions and negative electrons, makes the plasma electrically conductive. Since the amount of positive ions and negative electrons in plasma are roughly equal, the net charge density of a plasma is about zero. Thus, the term "quasi-neutral" is often used to describe the charge neutrality of plasma. Plasmas tend to shield quasi-static to time-varying electric fields with frequencies up to the plasma frequency; the plasma frequency is related to the characteristic response time of the plasma to the external fields. The plasma frequency $\omega_p$ is given by [31]

$$\omega_p = \sqrt{\frac{n_e e^2}{\varepsilon_0 m_e}} \qquad 2.1$$

where $n_e$ is the electron density, $e$ is the electron's charge, $\varepsilon_0$ is the permittivity of free-space, and $m_e$ is the mass of an electron. Shielding of an external electric field occurs across a characteristic distance called Debye length $\lambda_D$, defined as [31]

$$\lambda_D = \sqrt{\frac{\varepsilon_0 k T_e}{n_e e^2}} \qquad 2.2$$

where $T_e$ is the electron temperature, $n_e$ is the electron density, $k$ is Boltzmann's constant, $e$ is the electron's charge, and $\varepsilon_0$ is the permittivity of free-space. The Debye length characterizes the size of the primary sheath region surrounding an object inserted into a plasma; inside the plasma sheath there is a significant deviation from charge neutrality compared to the bulk of the plasma. For example, if a Langmuir probe is biased negatively, the plasma sheath will attract positive ions so that the density of the ions in the sheath is greater than the ion density in the bulk plasma. A schematic of the potential of the sheath region surrounding a negatively biased Langmuir probe is shown in Figure 2.1. Also, Figure 2.2 displays the Debye length of various plasmas over a range of different temperatures and densities. For Debye lengths smaller than about $10^{-4}$ m (100 $\mu$m), the construction of sub-Debye sized Langmuir probes with tight specs would be facilitated if microfabrication techniques were used.

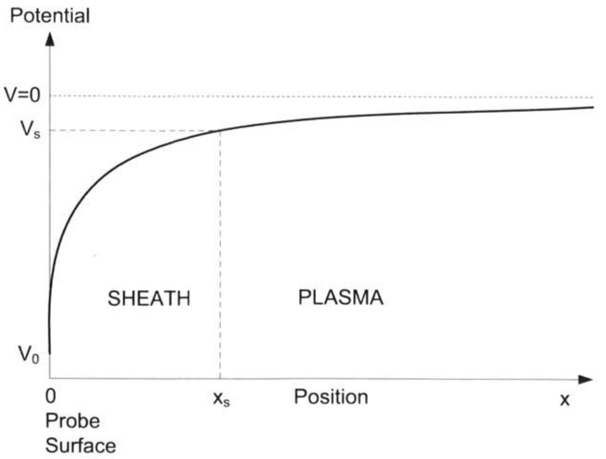

**Figure 2.1: Schematic of the electric potential versus distance from the surface of a negatively biased Langmuir probe. The bias voltage is $V_0$, the plasma potential is approximately $V_s$, and the sheath thickness is $x_s$ [31].**

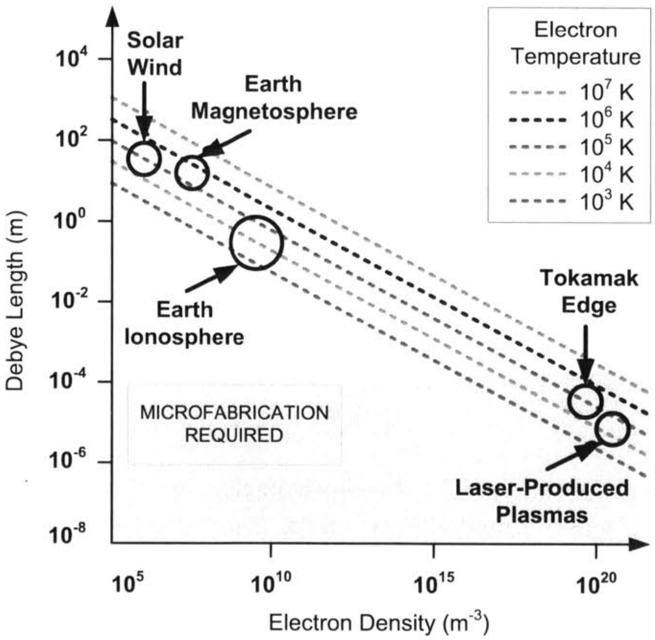

**Figure 2.2: Characteristic Debye lengths of various plasmas versus plasma electron temperature and number density [21].**

The simplest approach to measure the electron temperature and number density of a plasma involves the use of invasive diagnostics, that is, the insertion of a sensor directly into the plasma such as in the case of a Langmuir probe. Langmuir probes are the simplest plasma diagnostic instruments in existence [31] and they are named after the Nobel Prize winning physicist Irving Langmuir, whom extensively used these probes in his research. Langmuir probes can be used to estimate plasma parameters such as the electron temperature, the number density, and the floating potential.

A Langmuir probe consists of one or more electrodes inserted into plasma, with a constant or time-varying electric potential between the various electrodes, or between an electrode and the surrounding plasma vessel. Each electrode has an insulating jacket so that only the tip of the electrode interacts with the plasma. The basic setup of a single Langmuir probe is shown in Figure 2.3. Due to the applied electric potential, Langmuir probes attract or repel ions and electrons, producing a net electric current that can be measured. For a single Langmuir probe, the data is typically presented as I-V characteristics; using known physical relationships from a model that assumes certain properties of the plasma, the I-V characteristics can be analyzed to determine plasma parameters.

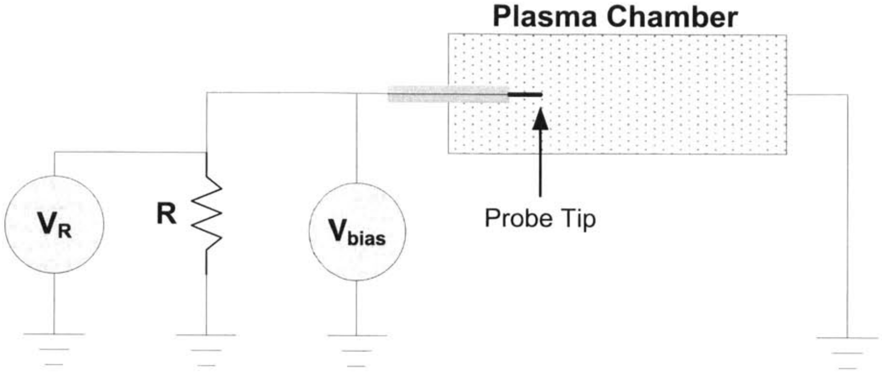

**Figure 2.3: Typical schematic of a single Langmuir probe experimental setup. The bias voltage to the probe is supplied by $V_{bias}$, and probe current is measured as a voltage across the resistor $R$ by $V_R$ [32].**

Langmuir probes are relatively simple to construct and operate; the difficulty in Langmuir probe plasma diagnostics entails understanding how a probe locally perturbs the plasma, and how the local plasma parameters are related to the unperturbed plasma far from the probe. The relationship between the measured plasma parameters and the unperturbed plasma parameters is the subject of several theories based on different sets of assumptions. Nonetheless, the general rule is that a probe is less likely to perturb the plasma if it is smaller than the plasma Debye length [29]. In theory, it is possible to insert an arbitrary number of sub-Debye length probes into plasma and not disturb it. Moreover, small sub-Debye length probes could be used to maximize the number of measurement sites. In this case, adjacent probes would need to be spaced several Debye lengths apart to avoid interference between adjacent Langmuir probes.

The sampling speed and size of the Langmuir probes must be compatible with the phenomena of interest. Regarding the probe size, it had been suggested to implement sub-Debye length Langmuir probes to minimize plasma perturbations and maximize the localization of the measurements [21]. Regarding the sampling speed, the Langmuir probe circuitry needs to sweep the probe's bias voltage at a frequency above the plasma fluctuation frequency intended to be measured. Otherwise, the resulting I-V characteristics would consist of the average current as a function of voltage, which could result in systematic errors if the I-V characteristics were treated as real-time data [33].

However, in many circumstances it is not feasible, or practical, to construct sub-Debye length Langmuir probes due to physical constraints. For example, miniaturized Langmuir probes have sensing tips with larger surface-to-volume ratio than the macro probe counterparts; smaller Debye lengths are usually related to higher number densities, resulting in higher erosion rates and probe reliability issues. It is certainly possible to estimate plasma parameters from data taken using Langmuir probes that are larger or smaller than the Debye length, but these estimates are based on theoretical models with assumptions that require validation through data analysis, as different physical phenomena dominate in the calculations of the plasma parameters, according to the size of the Langmuir probe and the Debye length. Therefore, the same probe will show different operating regimes depending on the relationship between the probe dimensions and the Debby length. If the size of the probe is much smaller than the Debye length, the sheath will be "thick" relative to the probe and the current collection is describe by the orbital motion limited regime (OML)[1]. If the probe is much larger than the Debye-length, then the sheath will be "thin" relative to the probe and one can assume that the plasma sheath can be modeled as a 1D phenomenon. Furthermore, if the Debye length is much smaller than the mean free path of the plasma, particles crossing the sheath will not undergo collisions (collisionless sheath regime). However, if the mean free path is much smaller than the Debye length, the particles will undergo many collisions as they cross the sheath (collisional sheath regime) [34]. The mean free path of a plasma *l*, is given by [35]

$$l = \frac{1}{ns} \qquad 2.3$$

where *n* is the particle number density and *s* is the momentum transfer scattering cross section for the particles. A schematic plot of the Langmuir probe operating regimes is presented in Figure 2.4.

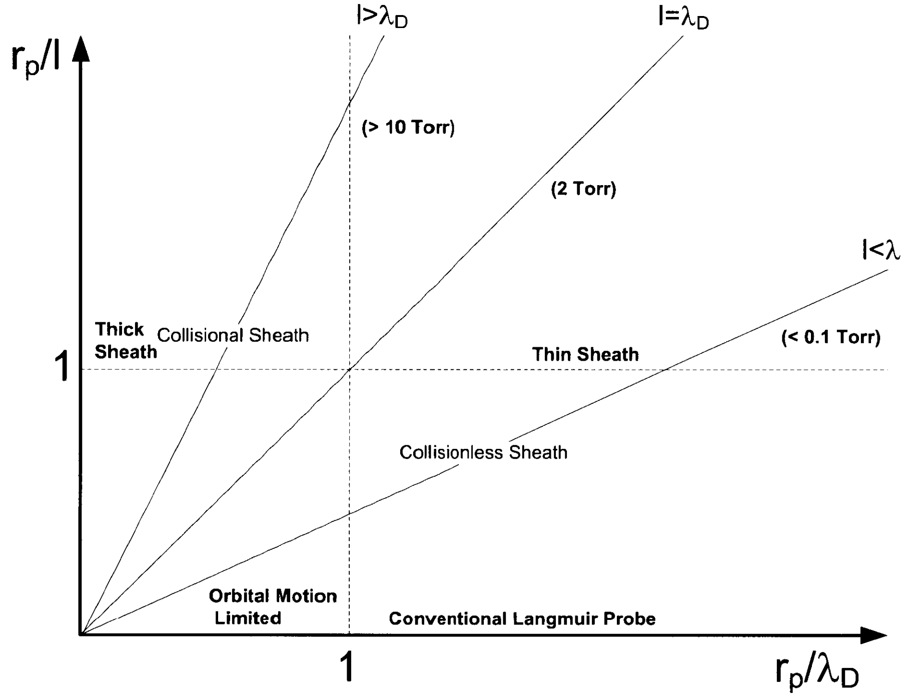

**Figure 2.4: Langmuir probe operating regimes in terms of probe diameter $r_p$, mean free path *l*, and Debye length $\lambda_D$ for cylindrical probes [34].**

## 2.2 Single Langmuir Probe Theory: Thin-Sheath, Collisionless Plasma

The MEMS multiplexed Langmuir probe technology that was developed in this thesis was tested in a thin-sheath collisionless plasma because the characteristic length of the Langmuir probes that were microfabricated was visibly larger than the Debye length of the plasma (about 4 – 90 μm), which was visibly smaller than the mean free-path of the plasma (5 – 10 m for electrons, and 3 m for ions) [36]. The I-V characteristics of a Langmuir probe operated in a thin-sheath collisionless plasma have three distinct regions (Figure 2.5). Region I is dominated by the ion current as the probe is biased at negative voltages (in the figure, a positive current is electron current); in Region III the collected current is mainly composed of electrons, corresponding to biasing the probe at positive voltages; Region II is a transition region where the net current is a combination of ion and electron currents and it contains critical information about the plasma parameters.

---

[1] The name of the regime reflects the similarity in the description of the dynamics of the charged particles under the influence of electrostatic forces and the dynamics of mass particles under the influence of gravitational forces.

In Region II, the floating potential $V_f$ corresponds to the voltage at which the net current through the Langmuir probe is zero (i.e., the $V$-axis intercept of the I-V characteristics); when the bias voltage of the Langmuir probe is equal to the plasma potential $V_p$, there is neither a retarding nor an accelerating field acting on the ions or electrons in the vicinity of the probe. Therefore, the current collected by the probe is related to its surface area (if the shape of the sensing area is convex) and the random flux of particles incident on the probe. If we assume that both the electron and ion densities are equal (quasi-neutrality), and that both electrons and ion energies are Maxwellian, then the total current is the sum of the electron current and the ion current (equation 2.4), where the electron current $I_e$ may be calculated using equation 2.5, and the ion current $I_i$ may be calculated using equation 2.6 [34]

$$I = I_e - I_i \tag{2.4}$$

$$I_e = \frac{1}{4} A_p ne \left(\frac{8kT_e}{\pi m_e}\right)^{1/2} \tag{2.5}$$

$$I_i = \frac{1}{4} A_p ne \left(\frac{8kT_i}{\pi m_i}\right)^{1/2} \tag{2.6}$$

where the surface area of the probe is $A_p$, the plasma density is $n$, Boltzmann's constant is $k$, the electron's mass is $m_e$, the ion's mass is $m_i$, the electron temperature is $T_e$, and the ion temperature is $T_i$.

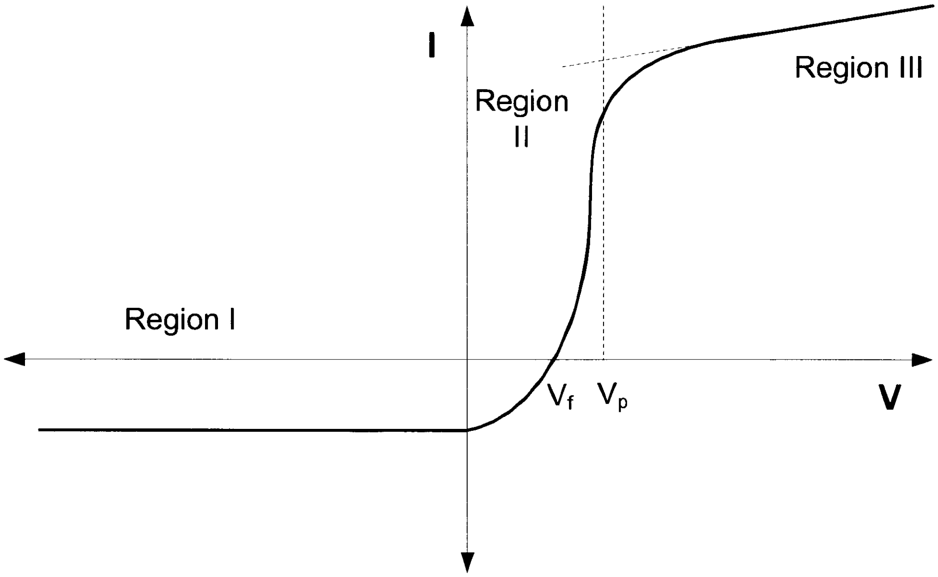

**Figure 2.5: Schematic I-V characteristics of a single Langmuir probe in the thin-sheath collisionless operating regime. The I-V characteristics have three distinct regions: Region I is dominated by ion current, Region III is dominated by electron current, and Region II is a transition region where the net current is a combination of ion and electron current. $V_f$ is the floating potential, and $V_p$ is the plasma potential [34].**

The plasma is biased at a certain plasma potential $V_p$. Since $m_i$>>$m_e$ and usually $T_e$>>$T_i$, there is a significant imbalance in electron flux to the probe when the bias is equal to $V_p$, resulting in a net positive current. In general, $V_f$ and $V_p$ are unrelated; the relationship between $V_f$ and $V_p$, as indicated in Figure

2.5, is that $V_f$ is negative with respect to $V_p$ such that a probe biased at $V_f$ sets an electric field that repels electrons and attracts ions to achieve zero net current. Assuming that the electron energy distribution function is Maxwellian, the electron current in Region II may be determined by [34]

$$I_e = \frac{1}{4} A_p ne \left(\frac{8kT_e}{\pi m_e}\right)^{1/2} exp\left(\frac{-eV_\phi}{kT_e}\right) \tag{2.7}$$

where $V_\phi = V_p - V$ is the retarding potential, $V$ is the probe bias voltage, and $V_p$ is the plasma potential. This equation assumes that the ion current is small compared to the electron current for $V > V_f$. It should be apparent from Region II that a plot of $I_e$ vs. $V_\phi$ would provide a direct measurement of the electron temperature, $T_e$. Accordingly, finding a proper curve fit in Region II is particularly important for the calculation of $T_e$. Proper mapping of Region II is crucial as it contains very valuable information about the plasma properties; otherwise, curve fitting can be a very tedious procedure, and dubious at best for unreliable or sparse data.

Region I corresponds to net collected currents mostly composed of positive ions. As Figure 2.5 suggests, Region I is an ion saturation region. In Region I the probe has a relatively large negative bias such that most electrons are repelled and the random ion current incident on the sheath edge constitutes the ion saturation current. Therefore, equation 2.6 provides a good estimate of the collected current in Region I. However, this would not be entirely accurate because the sheath edge in the ion saturation region cannot be considered finite unless the ions enter with a finite initial velocity $v_0$ given by the Bohm criterion [34]:

$$\left(\frac{m_i v_0{}^2}{2kT_e}\right)^{1/2} > \frac{1}{\sqrt{2}} \tag{2.8}$$

In other words, equation 2.8 states that for the common circumstance where $T_e >> T_i$, the ions must enter the sheath with an energy of $kT_e$. The ions are accelerated through a "pre-sheath" to acquire this energy. Therefore, a better estimate of the ion saturation current in Region I is given by [34]

$$I_i = \exp\left(-\frac{1}{2}\right) A_p ne \left(\frac{kT_e}{m_i}\right)^{1/2} \tag{2.9}$$

In Region III ($V > V_p$) there is a space-charge field that accelerates the electrons towards the probe and repels ions. In this region it can be assumed that the contribution due to ion current is negligible. Also, increasing $V$ would likely not have a significant effect on the electron current because the electron current is limited by the random flux entering the accelerating field of the probe. For this reason, Region III essentially represents an area of electron saturation current. However, the electron current cannot be determined using equation 2.5. Since $V$ is not equal to $V_p$ in Region III, there is a region of charge imbalance, or sheath, in which an electric field is present surrounding the probe. For cylindrical and spherical probes, variations in $V$ would vary the capture area of the probe, which is defined by the outer dimension of the sheath upon which random electron flux is incident. Therefore, in Region II $A_p$ is a function of $V$. In practice, Region III currents are visibly larger than Region I or Region II currents and therefore, experimental techniques focus on measuring the Region I and II parts of the I-V characteristics to infer the plasma properties from the data.

The equations provided in this section were based on the specific assumptions of the thin-sheath, collisionless operating regime. Thus, when analyzing data, one must be sure that the experimental conditions match the assumptions of the appropriate theory to be applied. In other words, Langmuir probes can operate in many different regimes, as discussed in Section 2.1, and different methods of analyzing the I-V characteristics exist for different operating regimes. It was beyond the scope of this thesis to introduce data analysis methods for all Langmuir probe operating regimes.

## 2.3 Experimental Facility

The characterization of the MEMS Langmuir probes was conducted in a plasma environment similar to reentry conditions because this environment constitutes an upper bound for the technology. As discussed in Chapter 1, the electron number density of the reentry plasma sheath depends on altitude and ranges from $10^{14}$ to $10^{18}$ $m^{-3}$, while the electron temperature ranges from about 0.1 to 1.0 eV. This corresponds to an electron Debye length of approximately 3 μm to 300 μm. We used a tokamak to generate the plasma we utilized in the characterization of the probes. A tokamak is a device in the shape of a torus that uses magnetic confinement to contain plasma (Figure 2.6). Magnetic field lines that move around the torus in a helical shape are required to achieve a stable plasma equilibrium. The helical field is generated by the addition of a toroidal field (traveling around the torus in circles) and a poloidal field (traveling in circles orthogonal to the toroidal field). In a tokamak, the toroidal field is generated by electromagnets surrounding the torus, and the poloidal field is the result of a toroidal electric current that flows inside the plasma. This toroidal electric current is induced inside the plasma with a second set of electromagnets [37].

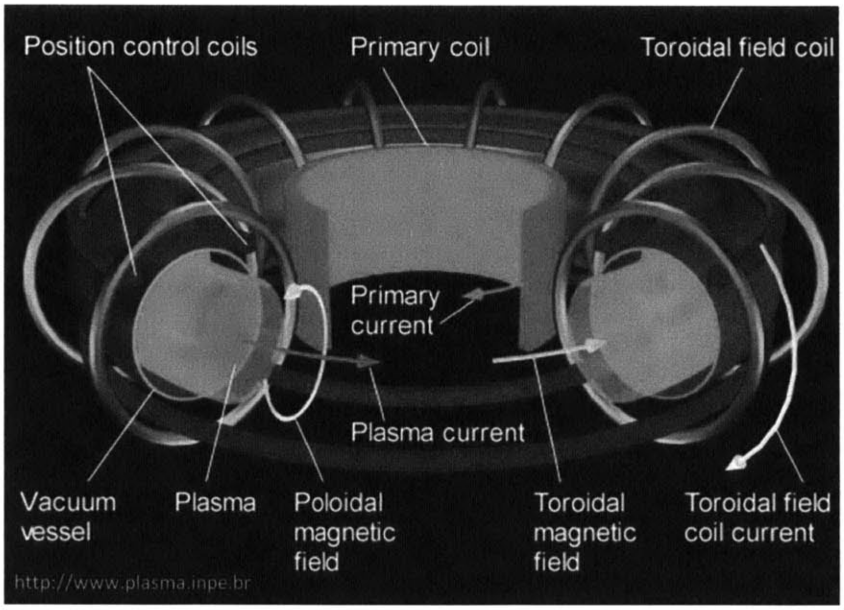

**Figure 2.6: The anatomy of a tokamak, illustrating the magnetic confinement of plasma within a vacuum vessel.**

We used the Versatile Toroidal Facility (VTF) at MIT, shown in Figure 2.7, to characterize our probes. VTF is a tokamak that contains argon plasma to simulate ionospheric conditions, which has a similar electron number density and Debye length compared to the reentry plasma sheath. In VTF, the electron number density is on the order of $10^{17} - 10^{18}$ $m^{-3}$, the electron temperature is approximately 2 – 15 eV, and the electron Debye length is approximately 4 – 90 μm [36,38,39,40,41]. At VTF, plasma was generated in 2 – 20 ms "shots" by 15 kW of microwave power that initiated the breakdown of particles by electron cyclotron resonant heating. The base pressure due to the azimuthally symmetric vacuum chamber was approximately $10^{-6}$ Torr, and the intensity of the toroidal magnetic field was approximately 100 mT.

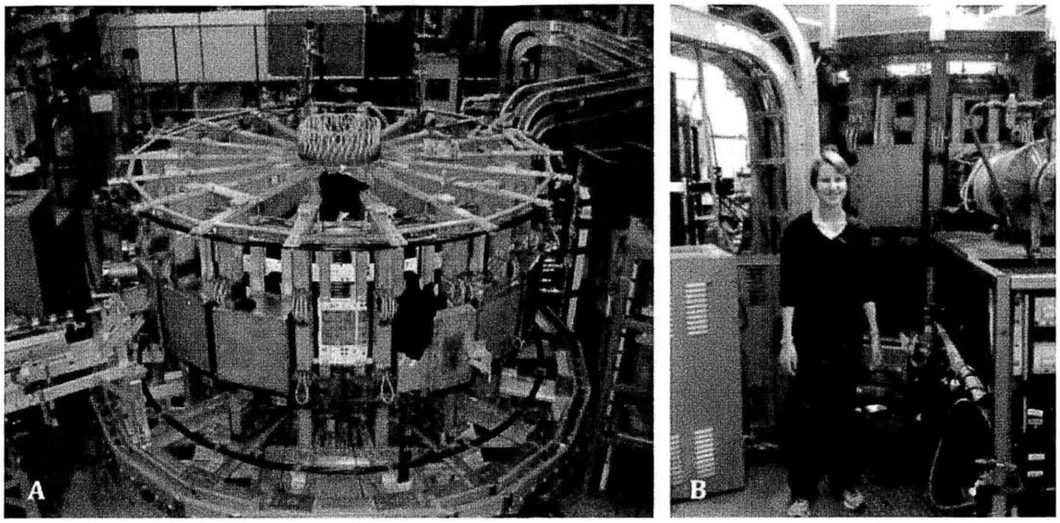

**Figure 2.7: (A) The Versatile Toroidal Facility (VTF) at MIT has an outer diameter of 3.5 m. (B) The author is pictured beside VTF to provide a sense of scale.**

### 2.3.1 Single Langmuir Probe Experimental Investigations

A conventional Langmuir probe was constructed to gain an understanding of how Langmuir probes work and to assess the stability of the plasma in the tokamak at VTF[2]. The tip of the Langmuir probe consisted of a 1 cm-long 1 mm-diameter stainless steel hypodermic needle. The needle was soldered to a 28 AWG Teflon-insulated copper wire encased within an alumina tube for protection against the plasma. The copper wire was soldered to an electrical connector to allow the probe to be biased at a certain voltage. The alumina tube was fastened within a stainless steel vacuum feed-through, which attached to the electrical connector and outer wall of the plasma chamber. Torr-Seal adhesive was used to seal the area below the probe tip to ensure plasma would not leak between the interface of the probe tip and alumina tubing. Photographs of the Langmuir probe are included in Figure 2.8 and Figure 2.9 shows the interior of the tokamak with the probe installed during operation.

---

[2] Purchasing a single Langmuir probe could have resulted in a cost of $24,240 (Hiden Corporation ESPion Langmuir probe and data processing software package).

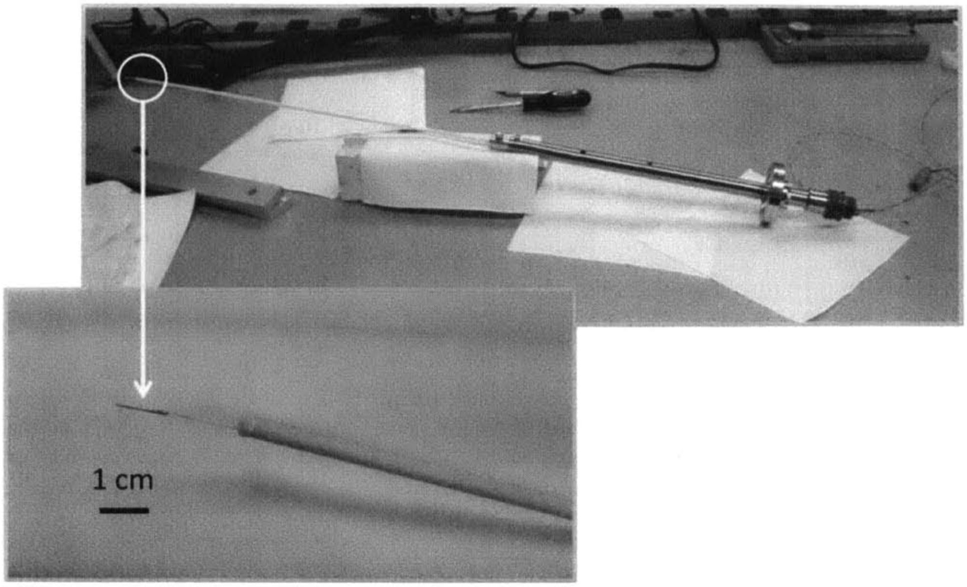

Figure 2.8: Photograph of the single Langmuir probe constructed in-house. The probe tip consisted of a 1 mm-diameter stainless steel hypodermic needle soldered to a thin copper wire and fed through alumina and stainless steel housing.

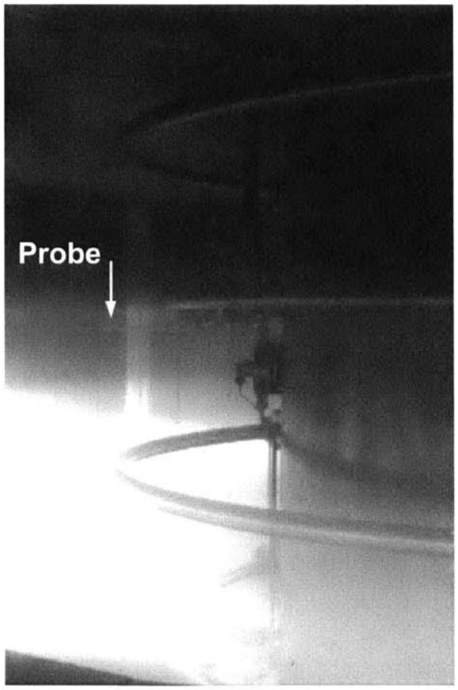

Figure 2.9: An image of the Langmuir probe in plasma within VTF.

During the experiments the probe was biased at various constant voltages, from -90 V to 30 V, using a power supply. The electrical circuit that was used to bias the probe and measure probe current is shown in Figure 2.10.

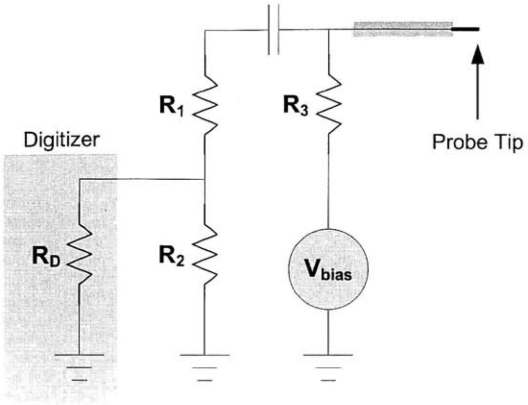

**Figure 2.10: Circuitry to acquire digitized voltage across $R_2$ from the single Langmuir probe operating in plasma at VTF. The voltage across $R_2$ was converted into probe current using equation 2.10. The bias voltage $V_{bias}$ was supplied to the probe using a power supply.**

The circuit was developed by a former student at VTF for operating single Langmuir probes. The circuit consisted of a voltage divider, from which the probe current could be calculated based upon the voltage across the resistor $R_2$. The voltage across $R_2$ was measured and digitized at a frequency of 2 MHz using GE's ICS645B single-ended digitizers. The purpose of the voltage divider was mainly to keep the input of the digitizer in the specified range of 1 V peak-to-peak. The probe current $I_{probe}$ was calculated from the voltage $V_{digitizer}$ across $R_2$ using

$$I_{probe} = \frac{V_{digitizer}}{\dfrac{R_2\left(\dfrac{1}{R_D}+\dfrac{1}{R_2}\right)^{-1}}{R_1+\left(\dfrac{1}{R_D}+\dfrac{1}{R_2}\right)^{-1}}+R_3} \tag{2.10}$$

where $R_D$=500 Ω, $R_1$=680 Ω, $R_2$=15k Ω, and $R_3$=680 Ω. $R_D$ represents the impedance of the digitizer. A sample of the raw data from the probe when biased at -90 V (ion saturation regime) is shown in Figure 2.11. This experimental result demonstrates that the plasma varied significantly during the 20 ms pulse.

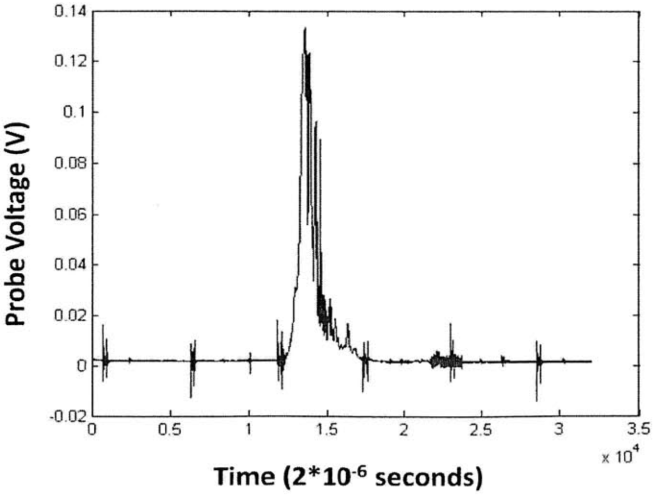

**Figure 2.11: Voltage across $R_2$ vs. time during one of the 20 ms plasma shots. The single Langmuir probe was biased at -90 V.**

Figure 2.12 shows the I-V characteristics of the Langmuir probe constructed from a series of measurements taken at various bias voltages from -90 V to 30 V. It would have been ideal to acquire measurements in 5 V steps, from -90 V to 30 V. Unfortunately, due to a time constraint at VTF, data was only acquired in 5 V steps between 0 V and 30 V, and additional measurements at -90 V were acquired. Hence, much of the ion saturation region is missing from the plot.

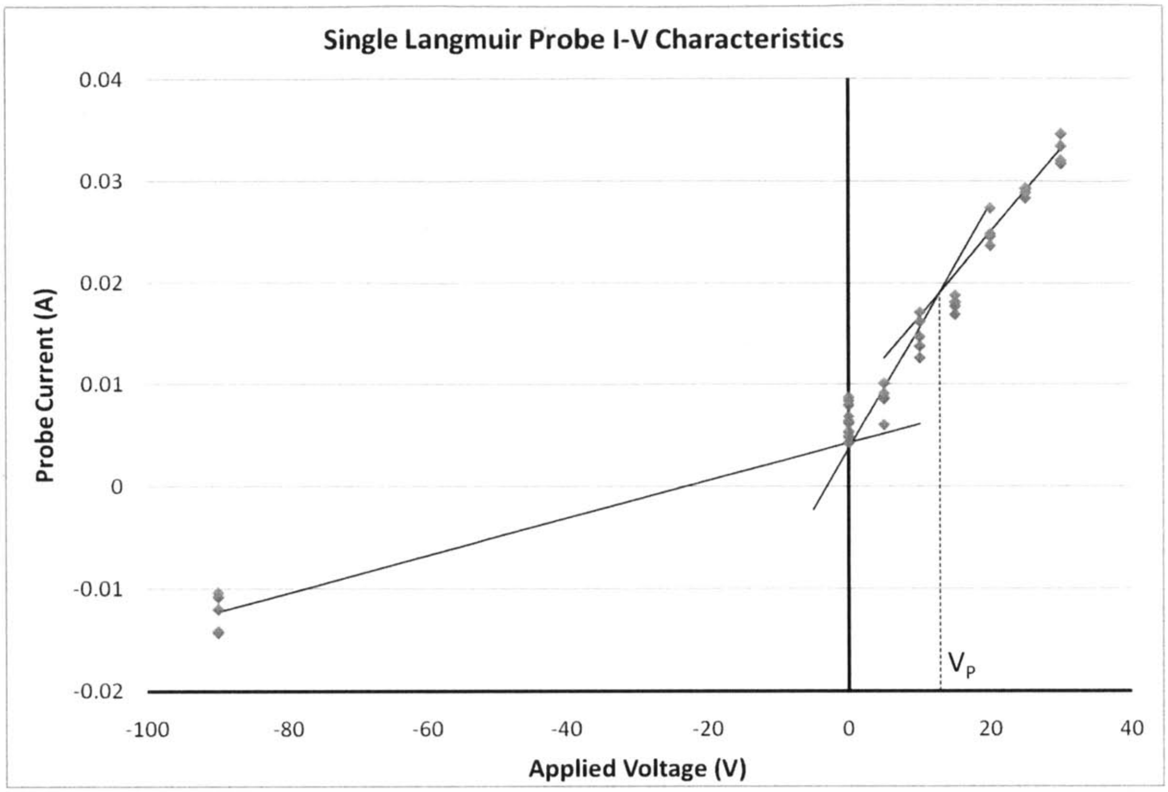

**Figure 2.12: The I-V characteristics of a single Langmuir probe operated in argon plasma at VTF. The electron current is shown as positive current. At least 5 current measurements were taken at each applied voltage. The average ion saturation current is approximately -0.012 Amps, shown at a value of -90 V.**

The procedure for calculating the electron temperature $T_e$ from the I-V characteristics generally involves rearranging the data in the transition region (Region II) to a semi-log plot of electron current $I_e$ versus $V_\phi$. This follows from equation 2.7, where the slope of $ln(I_e)$ versus $V_\phi$ is equal to $e/kT_e$ (or $1/T_e$ for units of $T_e$ in eV). Since $V_\phi=V_p-V$, the plasma potential is required to complete the calculation. Shown in Figure 2.12, $V_p$=12.81 V. In order to extract $I_e$ from the transition region (since the current in the transition region is composed of both ion and electron currents), typically a line is drawn through the ion saturation data points and extrapolated into the transition region, so that the calculation $I_e=I-I_i$ can be carried out. Again, there were not enough data points in the ion saturation region to extrapolate $I_i$ into the transition region, therefore the $T_e$ calculation was performed using just $I$ instead. This is a reasonable approximation because in the transition region, typically $I_e>>I_i$ [31]. The slope of the line of $ln(I)$ versus $V_\phi$ was determined using a linear fit by spreadsheet software, and the calculation of $slope=1/T_e$ resulted in $T_e$=7.435 eV. This temperature falls within the expected range of 2 – 15 eV.

Equation 2.9 was utilized to calculate the electron number density $n_e$, which requires $I_{saturation}$ and $T_e$ as inputs. For $T_e$=7.435 eV and $I_{saturation}$=0.0123 A, $n_e$ was found to be 2.70x$10^{18}$ $m^{-3}$, which falls within the anticipated order of magnitude of $10^{17}$ – $10^{18}$ $m^{-3}$.

Overall, extracting the electron temperature and number density from the I-V characteristics of a single Langmuir probe could be cumbersome due to the curve fitting procedure in the transition region, which requires many data points to achieve good accuracy. Generally, the bias voltage of a single Langmuir probes is swept, covering the range of voltages from the ion saturation region to the transition region. Hence, a major disadvantage of the single Langmuir probe method is that they are limited by the sampling speed of the voltage sweeping. Real-time measurements can be performed with a single Langmuir probe at the expense of complexity and analysis bandwidth because data fitting would be required for every voltage sweep. Considering that there could be thousands of MEMS Langmuir probes attached to a reentry vehicle, implementation and data analysis in real-time could be very challenging. Additionally, Langmuir probes having an applied AC signal, a pulse, or swept DC bias behave as antennas, potentially inducing fluctuations and instabilities in a plasma, which can cause significant perturbations and distorted data. Fortunately, sets of three Langmuir probes can be used to perform real-time measurements in a much simpler manner compared to single Langmuir probes with a dynamic sweep.

## 2.4 Triple Langmuir Probe Theory

Triple Langmuir probe theory was proposed by Chen and Sekiguchi in 1965 for use in collisionless, Maxwellian, non-magnetized plasma [33]. A major advantage of triple Langmuir probes over single Langmuir probes is that the former are capable of performing time-resolved measurements to the limit imposed by the intrinsic time response of the probe itself. Unlike a single Langmuir probe, a triple Langmuir probe does not require a voltage sweep. The probe consists of three identical single Langmuir probes at different static potentials, simplifying the experimental setup and eliminating the curve-fitting post-data analysis required to extract the plasma parameters in single Langmuir probes. Besides the simpler data processing, probe multiplexing is natural in the MEMS implementation since the probes are batch-fabricated as monolithic arrays with very similar specifications; the single probes can then be grouped and operated as triple Langmuir probes.

There are two possible approaches to operate a triple Langmuir probe, i.e., current-mode or voltage-mode. Current-mode operation was proposed first and it was followed by voltage-mode operation, which is a simplification of the current-mode approach. We will describe each technique in the following text while pointing out their pros and cons.

### 2.4.1 Current-Mode Operation

The configuration of the three probes $P_1$, $P_2$, and $P_3$ for operation in current-mode is shown in Figure 2.13. $P_1$ and $P_2$ are biased with respect to each other at the voltage $V_{d2}$, and $P_1$ and $P_3$ are biased with respect to each other at the voltage $V_{d3}$. In general, the probes should be placed close to each other in the plasma to ensure localization of the measurements, but not so close that the thickness of the ion sheath is larger than the separation between the probes, causing interaction effects among the probes. About three Debye lengths of separation between probes are needed to achieve this criterion.

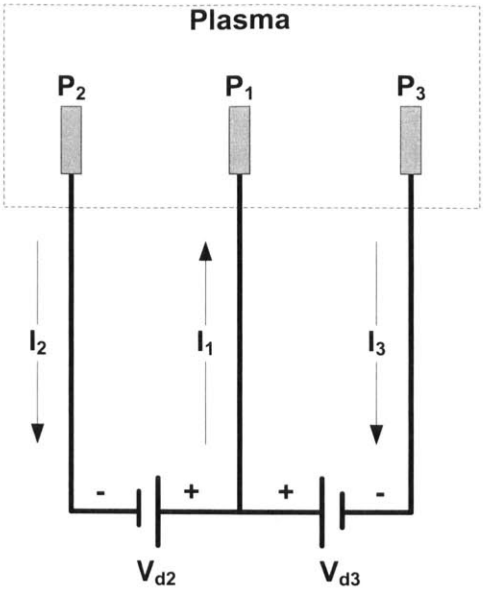

**Figure 2.13: Triple Langmuir probe configuration in current-mode operation [33].**

If the two probe voltages $V_{d2}$ and $V_{d3}$ are zero, the potential of each probe would automatically be fixed at its floating potential and no net current would flow into each probe. Alternatively, if two negative voltages $V_{d2}$ and $V_{d3}$ were applied to probes $P_2$ and $P_3$ with reference to $P_1$, then the potentials of $P_2$ and $P_3$ would become lower than the floating potential, and the currents flowing into $P_2$ and $P_3$ would be mostly ion current. Conversely, the potential of $P_1$ would be higher than the floating potential so that the current flowing into it would be mostly electron current.

Using current-mode to operate triple Langmuir probes, the electron temperature and number density can be calculated using measurements of $I_1$, $I_2$, and $I_3$ when the bias voltages $V_{d2}$ and $V_{d3}$ are supplied between the probes. In the experimental setup, $V_{d2}$ and $V_{d3}$ must be floating, hence batteries or floating power supplies are required. Chen and Sekiguchi performed an experiment to determine how to select the voltages of $V_{d2}$ and $V_{d3}$. While keeping $V_{d2}$ constant at 2 V and varying $V_{d3}$, they discovered that as $V_{d3}$ became small and approached $V_{d2}$, the error in the calculation of the electron temperature became more pronounced; the electron temperature calculated from the measurements of the triple probe was compared to the results of a calibrated single probe. However, when $V_{d3}$ was at least approximately 10 V, the error in the electron temperature was only minor, about 10%, compared to that of a single probe. In general, for plasma temperatures lower than 30 eV, Chen and Sekiguchi recommended using a low value for $V_{d2}$, around 2 V, and a value of at least 10 V for $V_{d3}$ to avoid large errors in the calculation of electron temperature. According to Chen and Sekiguchi, the significant error that occurs for lower values of $V_{d3}$ appears to be caused mainly by a residual difference in space potential among the three probes that is not negligible for low values of $V_{d3}$; it does not appear to be caused by a variation in ion saturation current [33].

Assuming that the geometry of each probe is identical, and the directions of the probe currents $I_1$, $I_2$, and $I_3$ are taken as shown in Figure 2.13, the relationship between the probe currents is

$$I_1 = I_2 + I_3 \qquad 2.11$$

In order to derive the plasma electron temperature and number density, Chen and Sekiguchi first made the following assumptions:

a. The electron energy distribution in the plasma is Maxwellian.

b. The mean free path of the electrons is much larger than both the thickness of the ion sheath around each probe and the probe radius.

c. The thickness of the ion sheath is smaller than the separation between probes, so that interaction effects among the probes are negligible.

d. The ion saturation current is constant with respect to increasing the negative probe potential.

From these assumptions, equations 2.12 – 2.14 were formulated to solve for the plasma electron temperature and number density, where $J_i$ is the ion saturation current density, and $n_e$ is the electron number density [33]:

$$\frac{I_1 + I_2}{I_1 + I_3} = \frac{1 - \exp\left(-\frac{e}{kT_e} V_{d2}\right)}{1 - \exp\left(-\frac{e}{kT_e} V_{d3}\right)} \tag{2.12}$$

$$n_e = \frac{J_i}{\exp\left(-\frac{1}{2}\right) e \left(\frac{kT_e}{m_i}\right)^{1/2}} \tag{2.13}$$

$$J_i = \frac{1}{A_p} \frac{I_3 - I_2 exp\left(-\frac{e}{kT_e}(V_{d3} - V_{d2})\right)}{1 - exp\left(-\frac{e}{kT_e}(V_{d3} - V_{d2})\right)} \tag{2.14}$$

### 2.4.2 Voltage-Mode Operation

Voltage-mode operation is similar to current-mode operation, except that one of the probes is always forced to be at the floating potential by the removal of the external voltage source $V_{d2}$, as shown in Figure 2.14. Therefore, with $V_{d3}$ fixed, the electron temperature and number density can be calculated using the voltage-mode theory through the measurements of $I$ and $V_{d2}$. The measurement of $V_{d2}$ should be taken with a high impedance (> 1 MΩ,) to have essentially zero current between $P_2$ and $P_1$ [33]. In voltage-mode $I_2=0$ and thus $I_1=I_3=I$. Therefore, equation 2.12 reduces to equation 2.15 for the electron temperature, and the number density is given by equation 2.16 [33]:

$$\frac{1 - \exp\left(-\frac{e}{kT_e} V_{d2}\right)}{1 - \exp\left(-\frac{e}{kT_e} V_{d3}\right)} = \frac{1}{2} \tag{2.15}$$

$$n_e = \left(\frac{{m_i}^{1/2}}{A_p} I\right) \frac{\exp\left(\frac{1}{2}\right)}{e(kT_e)^{1/2}\left[exp\left(\frac{e}{kT_e} V_{d2}\right) - 1\right]} \tag{2.16}$$

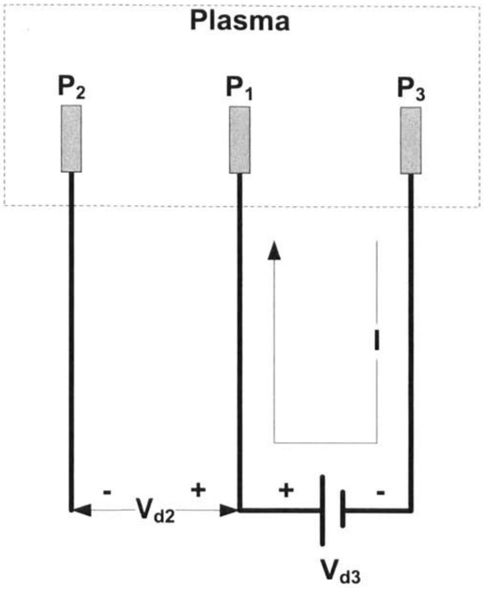

**Figure 2.14: Triple Langmuir probe configuration in voltage-mode operation [33].**

Similar to current-mode, the value of $V_{d3}$ should be at least 10 V to avoid errors associated with the electron temperature [33]. Also, because $V_{d3}$ in equation 2.15 is a fixed voltage from an external source, it is possible to calculate the electron temperature solely based on the measurement of $V_{d2}$. This is a major advantage of the voltage-mode method. However, to ensure a good measurement of $V_{d2}$, the instrumentation must have high input impedance. If high input impedance measurements are not possible, the current-mode operational scheme would likely yield more accurate data for the calculation of the electron temperature. A general disadvantage of the triple probe method is that information about the plasma electron energy distribution function (EEDF) cannot be measured [33]. However, acquiring information about the plasma EEDF is not related to the objectives of this thesis.

## 2.5 Chapter 2 Summary

This chapter provided the theoretical foundation of Langmuir probe plasma diagnostics. It was shown how the I-V characteristics from a single Langmuir probe could be used to estimate the plasma properties. It was also shown that real-time measurements could be conducted using triple Langmuir probes, i.e., sets of three probes that work together while conducting the measurements. Two different modes to collect data from triple Langmuir probes were described.

# 3 MEMS Langmuir Probe Design

In this chapter the design of the multiplexed MEMS Langmuir probes developed in this thesis is presented; the design takes into account thermal, structural, plasma, and microfabrication aspects of the probes using a set of candidate fabrication materials. First, we conducted a heat transfer analysis that uses as input spacecraft reentry heat flux data from the literature. Next, we assess the mechanical performance of the candidate materials due to thermal mismatch. Then, we proposed the geometry of the MEMS Langmuir probes based on the reentry plasma Debye length data found in the literature. Finally, we surveyed the microfabrication technologies available at MIT's Microsystems Technology Laboratories (MTL) to down-select a set of materials and processes to batch-fabricate the MEMS probes, resulting in a design concept. The implementation of the design concept that resulted from this exercise is documented in Chapter 4.

## 3.1 Heat Transfer Considerations

A very rough heat transfer analysis was proposed to estimate the peak temperature of the MEMS Langmuir probes during reentry. The materials that were considered in this analysis were silicon carbide, alumina, platinum, tungsten, nickel, Pyrex, gold, silicon oxide, and silicon nitride; we considered these materials because of their high melting temperatures and because of their feasibility to be processed using microfabrication techniques. This analysis included both dielectric and conductive materials because Langmuir probes consist of an electrically conductive core surrounded by an electrically insulating jacket. However, the analysis did not take into consideration the heat transfer between the dielectric and conductive materials. Instead, the model addresses each material as a 1D semi-infinite solid in contact with heat flux from the plasma sheath (Figure 3.1) to estimate whether the material reaches its melting point during reentry.

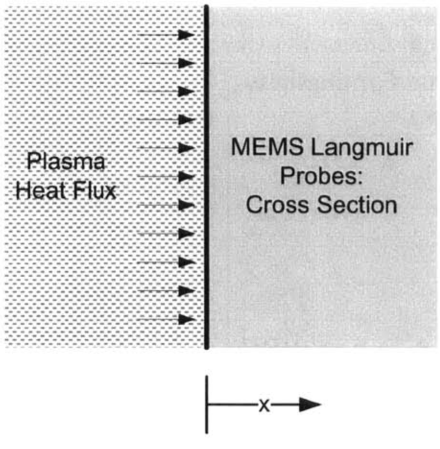

**Figure 3.1: Diagram of transient heat flux into semi-infinite solid.**

The heat transfer analysis did not take into account radiation; furthermore, it only took into consideration the heat transfer into the semi-infinite solid due to conduction. The transient analysis of the temperature on the free surface of a semi-infinite solid, given a constant heat flux, was calculated using equation 3.1, where *T* is the final surface temperature, $T_i$ is the initial surface temperature, $q_0/A$ is the heat flux, $\alpha$ is the thermal diffusivity, and $\tau$ is time [42].

$$T = \frac{2q_0\sqrt{\alpha\tau/\pi}}{kA} - T_i \qquad 3.1$$

The heat transfer analysis estimated the temperature on the external surface of the MEMS Langmuir probes using as input the Space Shuttle reentry heat flux data that we found in the literature [43]. For simplicity, we assumed that the heat flux was constant throughout reentry; in reality, the heat flux varies considerably with respect to velocity and altitude. In the first set of simulations we used the peak heat flux of the Space Shuttle's wing leading edge to estimate an upper bound of the temperature that the probes will reach during reentry; in the second set of simulations we used the average heat flux of the Space Shuttle's windward side to estimate the temperature that a cooler region of the spacecraft (i.e., away from the leading edge) would experience. The Space Shuttle experimental heat flux data utilized in the simulations was measured by radiometers on the STS-2 and STS-3 missions, and accounted for all modes of heat transfer [43]. From the data, the constant peak heat flux is $9.09\times10^5$ $W/m^2$ and the average heat flux is $7.95\times10^4$ $W/m^2$. In the heat transfer analysis the initial pre-reentry surface temperature was set at 394 K based on NASA's temperature measurements of orbiting objects in direct sunlight [44]. For simplification, we assumed that the thermal conductivity and diffusivity of the materials were constant. The thermophysical constants of the different materials included in the heat transfer analysis are provided in Table 3.1. We calculated the final temperatures after 27 minutes of reentry, which is a typical reentry time in Space Shuttle missions.

As shown in Figure 3.2.A, the results of the heat transfer simulations based on the leading edge peak heat flux, the only materials that would not melt are silicon carbide, alumina, and tungsten. As shown in Figure 3.2.B, the results of the heat transfer simulations predict that under the conditions of average windward heat flux, the only materials that melt are Pyrex and silicon oxide. This result for Pyrex was expected because it has the lowest melting temperature and lowest thermal conductivity of all the candidate materials considered; it is also not surprising that silicon oxide melts because it has the second lowest thermal conductivity and third lowest thermal diffusivity compared to the other candidate materials. Table 3.2 indicates the lifespan (time before melting) of the materials in both cases.

**Table 3.1: Thermophysical Constants Utilized in Heat Transfer Model**

| **Material** | **Thermal Conductivity (W/mK)** | **Thermal Diffusivity ($m^2$/sec)** | **Melting Temperature (K)** |
|---|---:|---:|---:|
| **Electrical Conductors** | | | |
| Silicon Carbide | 120.0 | $1.60 \times 10^{-5}$ | 3003 |
| Platinum | 71.6 | $2.57 \times 10^{-5}$ | 2041 |
| Tungsten | 173.0 | $6.91 \times 10^{-7}$ | 3695 |
| Gold | 318.0 | $1.27 \times 10^{-4}$ | 1337 |
| Nickel | 90.9 | $1.89 \times 10^{-7}$ | 1728 |
| **Electrical Insulators** | | | |
| Silicon Nitride | 30.0 | $7.00 \times 10^{-6}$ | 2173 |
| Silicon Oxide | 1.4 | $7.04 \times 10^{-7}$ | 1873 |
| Pyrex | 1.1 | $6.65 \times 10^{-6}$ | 1093 |
| Alumina | 35.0 | $2.50 \times 10^{-6}$ | 2345 |

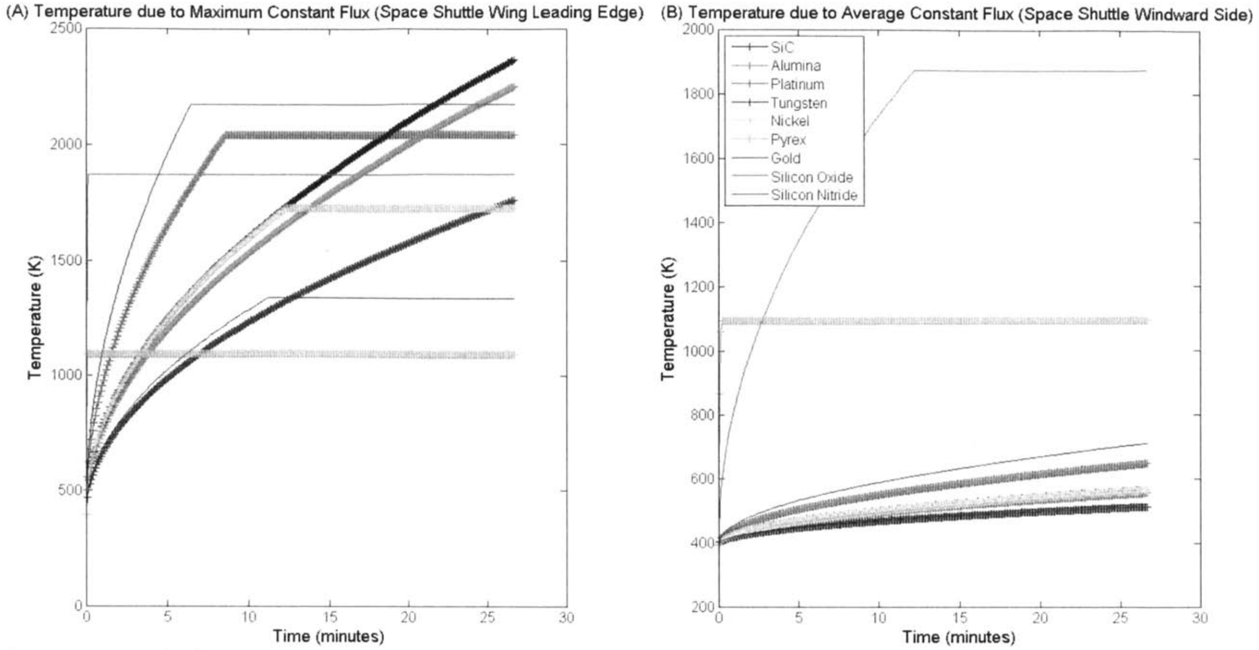

**Figure 3.2: Results from the reentry heat transfer analysis: (A) Surface temperature vs. time due to constant peak reentry heat flux measured on the leading edge of the Space Shuttle's wing; (B) Surface temperature vs. time due to average constant heat flux on the windward side of the Space Shuttle.**

**Table 3.2: Time before Melting during Reentry**

| **Material** | **Lifespan – Peak Heat Flux (minutes)** | **Lifetime – Average Heat Flux (minutes)** |
|---|---:|---:|
| Platinum | 8.67 | n/a |
| Nickel | 12.33 | n/a |
| Pyrex | 0.17 | 0.33 |
| Gold | 11.17 | n/a |
| Silicon Oxide | 0.17 | 12.25 |
| Silicon Nitride | 6.5 | n/a |

It is important to point out that the heat transfer analysis is very rough and conservative. For example, the Space Shuttle experiences peak heat flux during reentry for only about 5 minutes [45]. Therefore, the materials that are predicted to melt due to the peak heat flux conditions would probably survive, with the exception of Pyrex and silicon oxide. Also, the model does not take into account radiation heat transfer; radiation will certainly occur during reentry and it will help to cool down the probes. In addition, a cooling system can be implemented under the plasma diagnostics sensorial skin to prevent melting of the probes. The amount of constant heat flux that each material can withstand during a 27-minute reentry without melting (i.e., the heat flux tolerance) was calculated to estimate the requirements of a cooling system. The amount of cooling required was estimated by subtracting the heat flux tolerance from peak and average reentry heat fluxes. In each case, only the materials that melted before 27 minutes were analyzed. The results are presented in Table 3.3. The reentry heat transfer results presented in Figure 3.2 are reworked in Figure 3.3 to account for the heat flux tolerances and cooling systems of the materials that are predicted to melt due to the peak and/or average reentry heat fluxes. For example, Table 3.3 indicates that Pyrex can withstand a heat flux of $6.60 \times 10^3$ W/$m^2$ without melting during reentry; hence this heat flux was used in equation 3.1 for the model shown in Figure 3.3 to account for the cooling system that Pyrex would have to prevent it from melting.

| Table 3.3: Reentry Heat Flux Tolerance and Cooling System Requirements | | | |
|---|---|---|---|
| **Material** | **Heat Flux Tolerance before Melting (W/m$^2$)** | **Cooling Required during Peak Heat Flux (W/m$^2$)** | **Cooling Required during Average Heat Flux (W/m$^2$)** |
| **Electrical Conductors** | | | |
| Silicon Carbide | $1.74\times10^6$ | n/a | n/a |
| Platinum | $5.10\times10^5$ | $3.99\times10^5$ | n/a |
| Tungsten | $1.52\times10^6$ | n/a | n/a |
| Gold | $5.90\times10^5$ | $3.19\times10^5$ | n/a |
| Nickel | $6.20\times10^5$ | $2.89\times10^5$ | n/a |
| **Electrical Insulators** | | | |
| Silicon Nitride | $4.40\times10^5$ | $4.69\times10^5$ | n/a |
| Silicon Oxide | $5.40\times10^4$ | $8.55\times10^5$ | $2.55\times10^4$ |
| Pyrex | $6.60\times10^3$ | $9.02\times10^5$ | $7.29\times10^4$ |
| Alumina | $9.5\times10^5$ | n/a | n/a |

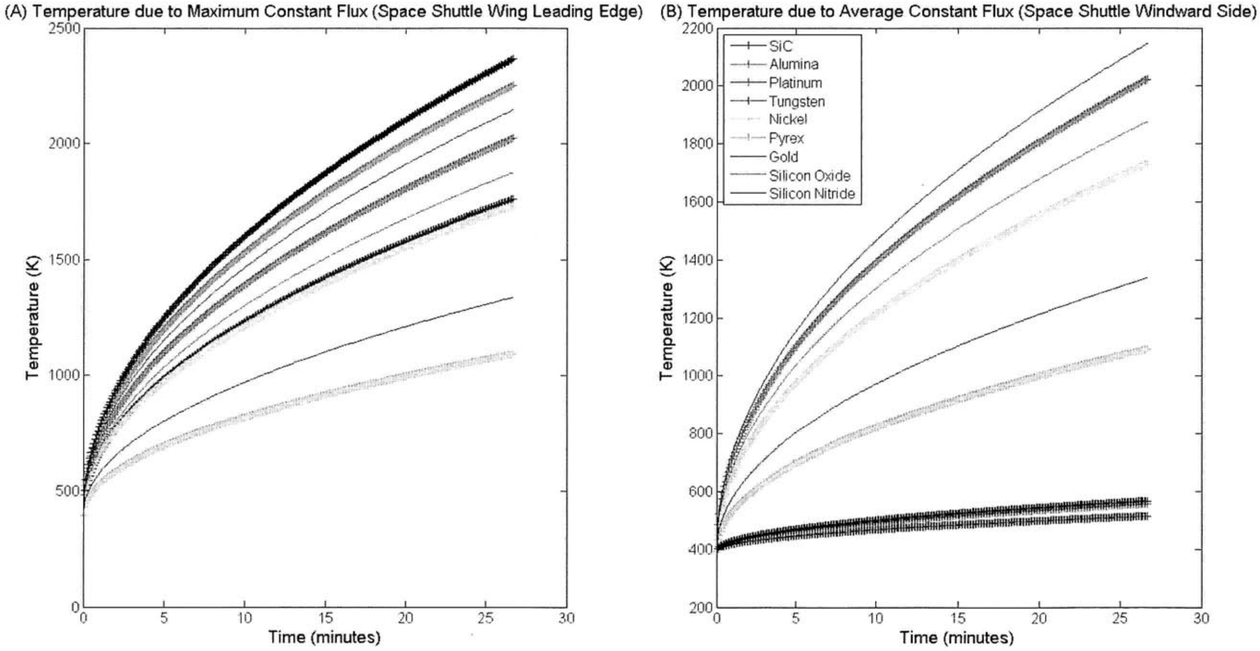

**Figure 3.3: Results from the reentry heat transfer model, where a cooling system was implemented to prevent materials from melting: (A) Surface temperature vs. time due to constant peak reentry heat flux measured on the leading edge of the Space Shuttle's wing; (B) Surface temperature vs. time due to average constant heat flux on the windward side of the Space Shuttle.**

Overall, the heat transfer model in Figure 3.3, which accounts for a cooling system beneath the sensorial skin, indicates that any of the candidate materials could be given further consideration for the manufacture of MEMS Langmuir probes for reentry applications. Accordingly, the relatively high temperatures that the model predicted for each material make the case for an analysis of the mechanical behavior of the probes due to thermal expansion.

## 3.2 Thermal Expansion Considerations

The construction of Langmuir probes entails the pairing of an electrically conductive core with a surrounding electrically insulating jacket. Because different materials have different thermal expansion rates, Langmuir probe materials should be paired together that experience similar changes in dimensions throughout reentry. If the thermal expansion characteristics are not sufficiently similar, structural failures such as delamination and cracking could occur [42]. A simple linear thermal expansion model was utilized to determine which candidate MEMS Langmuir probe materials had similar rates of thermal expansion during the reentry conditions that were modeled in Figure 3.3. The thermal expansion per unit length of a material is equivalent to the thermal expansion coefficient multiplied by the change in temperature relative to the baseline temperature [42]. The linear thermal expansion coefficients utilized in this analysis are presented in Table 3.4.

**Table 3.4: Coefficients of Thermal Expansion**

| **Electrical Conductors** | **Silicon Carbide** | **Platinum** | **Tungsten** | **Gold** | **Nickel** |
|---|---|---|---|---|---|
| Coefficient ($\mu$m/m) | 4.4 | 8.8 | 4.5 | 14.2 | 13.4 |
| **Electrical Insulators** | **Alumina** | **Silicon Nitride** | **Pyrex** | **Silicon Oxide** | |
| Coefficient ($\mu$m/m) | 7.1 | 3.3 | 3.0 | 0.55 | |

We estimated the thermal strain vs. time of the candidate materials during reentry, according to the surface temperatures shown in Figure 3.3. Figure 3.4.A shows the estimates for the peak reentry heat flux case, and Figure 3.4.B shows the estimates for the average reentry heat flux case. It is apparent from Figure 3.4 that none of the materials exhibit identical thermal expansion characteristics during reentry. Under these conditions, the thermal mismatch caused by pairing an electrical insulator with an electrical conductor would result in a net strain between the two materials, which could cause structural failure if the strain is large enough. The net strains due to thermal mismatch between all of the candidate electrical insulators and conductors are shown in Table 3.5. The net strains were calculated using the maximum thermal expansion rates shown in Figures 3.4.A and 3.4.B, which correspond to the worst-case scenario behavior of the materials. Also, Table 3.5 indicates whether the net strain is tensile or compressive. Considering that in a Langmuir probe an electrical insulator jacket surrounds a conductor core, it follows that the two materials are in tension when the thermal expansion rate of the electrical insulator is greater than the thermal expansion rate of the conductor. Conversely, the two materials are in compression when the thermal expansion rate of the electrical insulator is less than the thermal expansion rate of the conductor.

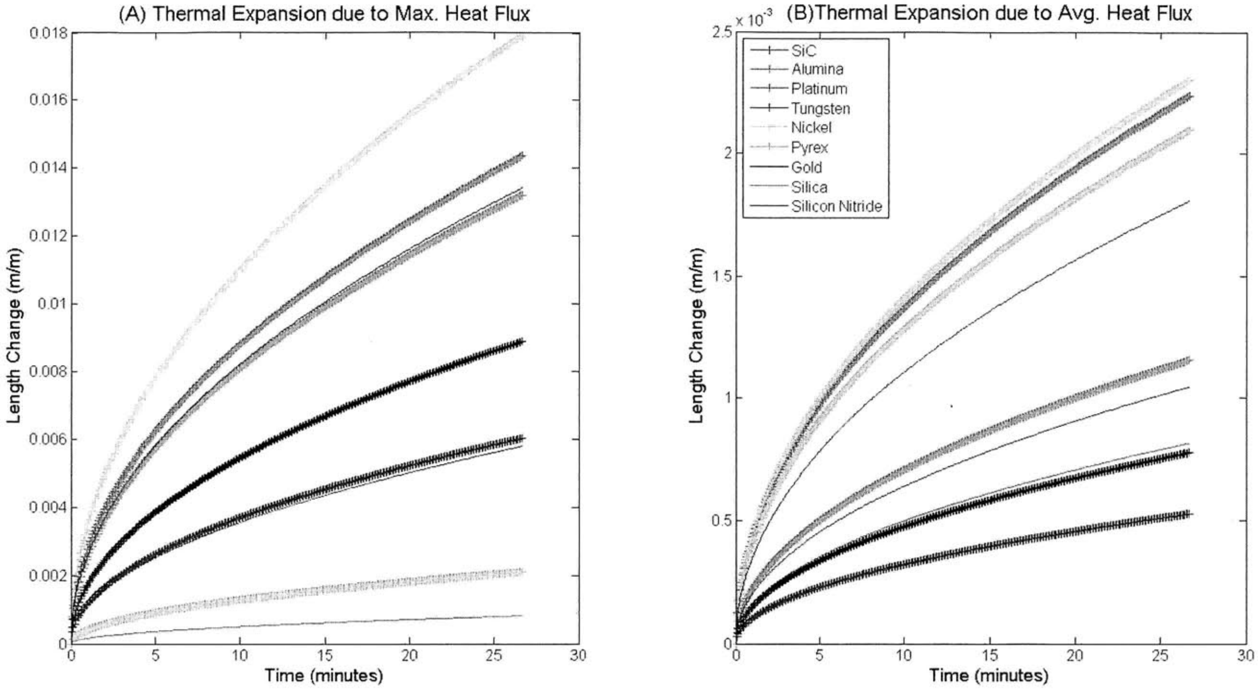

**Figure 3.4: The linear expansion of MEMS Langmuir probe materials during the reentry conditions modeled in Figure 3.3.**

To determine whether the thermal mismatch between two candidate materials would cause structural failure, the net strains in Table 3.5 were compared to the tensile and compressive failure strains of each material. This analysis assumes the worst-case scenario, where one of the materials is perfectly rigid (the dielectric) and the other accommodates all of the strain. As an order of magnitude approximation, the tensile failure strain was calculated as the ratio of the tensile strength to Young's modulus. Likewise, the compressive failure strain was calculated as the ratio of compressive strength to Young's modulus. Table 3.6 summarizes the tensile strength, compressive strength, Young's modulus, and estimated tensile and compressive failure strains for each of the candidate materials. The compressive strengths of the malleable materials (platinum, tungsten, gold, and nickel) are not reported in Table 3.6. This is because malleable materials plastically deform under large compressive stresses before fracture.

**Table 3.5: Net Strain between Candidate MEMS Langmuir Probe Materials**

| | | | | | |
|---|---|---|---|---|---|
| **Peak Reentry Heat Flux** | | | | | |
| | **Silicon Carbide** | **Platinum** | **Tungsten** | **Nickel** | **Gold** |
| **Alumina** | (T)* 0.0025 | (C) 0.0050 | (T) 0.0013 | (C) 0.0055 | (C) 0.0031 |
| **Silicon Nitride** | (C)** 0.0004 | (C) 0.0071 | (C) 0.0008 | (C) 0.0076 | (C) 0.0052 |
| **Pyrex** | (C) 0.00010 | (C) 0.0076 | (C) 0.0013 | (C) 0.0081 | (C) 0.0057 |
| **Silicon Oxide** | (C) 0.0014 | (C) 0.0089 | (C) 0.0026 | (C) 0.0044 | (C) 0.0070 |
| **Average Reentry Heat Flux** | | | | | |
| | **Silicon Carbide** | **Platinum** | **Tungsten** | **Nickel** | **Gold** |
| **Alumina** | (T) 0.00067 | (C) 0.0010 | (T) 0.00042 | (C) 0.0011 | (C) 0.00060 |
| **Silicon Nitride** | (T) 0.00047 | (C) 0.0012 | (T) 0.00022 | (C) 0.0013 | (C) 0.00080 |
| **Pyrex** | (T) 0.0016 | (C) 0.0001 | (T) 0.0013 | (C) 0.0002 | (T) 0.00030 |
| **Silicon Oxide** | (T) 0.00029 | (C) 0.0014 | (T) 0.000037 | (C) 0.0015 | (C) 0.00099 |

***(T) Tensile strain**
****(C) Compressive strain**

**Table 3.6: Tensile Strength, Compressive Strength, Young's Modulus, and Failure Strain**

| **Electrical Conductors** | **Silicon Carbide** | **Platinum** | **Tungsten** | **Gold** | **Nickel** |
|---|---|---|---|---|---|
| Tensile Strength (GPa) | 0.250 | 0.240 | 0.550 | 0.120 | 0.195 |
| Compressive Strength (GPa) | 3.900 | N/A | N/A | N/A | N/A |
| Young's Modulus (GPa) | 450 | 168 | 400 | 79 | 200 |
| Tensile Failure Strain (m/m) | $5.56\times10^{-4}$ | $1.43\times10^{-3}$ | $1.38\times10^{-3}$ | $1.59\times10^{-3}$ | $9.75\times10^{-4}$ |
| Compressive Failure Strain (m/m) | $8.67\times10^{-3}$ | N/A | N/A | N/A | N/A |
| **Electrical Insulators** | **Alumina** | **Silicon Nitride** | **Pyrex** | **Silicon Oxide** | |
| Tensile Strength (GPa) | 0.300 | 0.434 | 0.062 | 0.049 | |
| Compressive Strength (GPa) | 2.10 | 2.76 | 2.00 | 1.10 | |
| Young's Modulus (GPa) | 394 | 310 | 64 | 73 | |
| Tensile Failure Strain (m/m) | $7.61\times10^{-4}$ | $1.40\times10^{-3}$ | $9.69\times10^{-4}$ | $6.71\times10^{-4}$ | |
| Compressive Failure Strain (m/m) | $5.33\times10^{-3}$ | $8.90\times10^{-3}$ | $3.10\times10^{-2}$ | $1.5\times10^{-2}$ | |

The net strains in Table 3.5 were compared to the failure strains in Table 3.6 to estimate which pairs of electrical insulators and conductors will structurally fail due to thermal mismatch during reentry. In the cases where the net strain is compressive, only the failure conditions of the brittle materials (silicon carbide, alumina, silicon nitride, Pyrex, silicon oxide) were evaluated. Table 3.7 identifies the materials that experience structural failure due to thermal mismatch. The results indicate that during the peak reentry heat flux case, all of the electrical insulators are compatible with any of the electrical conductors, except for the case of alumina. Alumina structurally fails due to thermal mismatch when paired with tungsten, nickel, or silicon carbide during the peak reentry heat flux. During the average reentry heat flux, silicon carbide is not compatible with alumina, and Pyrex is not compatible with silicon carbide or tungsten. Otherwise, all other pairs of materials will not structurally fail due to thermal mismatch when subjected to the average reentry heat flux. Overall, there are many combinations of electrical conductors and insulators that are compatible with each under the worst-case scenario assumptions that this thermal mismatch analysis utilized.

**Table 3.7: Structural Failure due to Thermal Mismatch from Peak Reentry Heat Flux**

| **Peak Reentry Heat Flux** | | | | | |
|---|---|---|---|---|---|
| | **Silicon Carbide** | **Platinum** | **Tungsten** | **Nickel** | **Gold** |
| **Alumina** | Both fail | ✓ | Alumina fails | Alumina fails | ✓ |
| **Silicon Nitride** | ✓ | ✓ | ✓ | ✓ | ✓ |
| **Pyrex** | ✓ | ✓ | ✓ | ✓ | ✓ |
| **Silicon Oxide** | ✓ | ✓ | ✓ | ✓ | ✓ |
| **Average Reentry Heat Flux** | | | | | |
| | **Silicon Carbide** | **Platinum** | **Tungsten** | **Nickel** | **Gold** |
| **Alumina** | Silicon Carbide fails | ✓ | ✓ | ✓ | ✓ |
| **Silicon Nitride** | ✓ | ✓ | ✓ | ✓ | ✓ |
| **Pyrex** | Both fail | ✓ | Pyrex fails | ✓ | ✓ |
| **Silicon Oxide** | ✓ | ✓ | ✓ | ✓ | ✓ |

The reentry heat transfer and thermal expansion models presented in this thesis provide a rough estimate of the behavior of nine materials often utilized to microfabricate devices for high-temperature applications. The reentry heat transfer model shows that any of the candidate materials are suitable for reentry applications as long as cooling is provided for materials that would otherwise melt. The thermal mismatch analysis shows that out of the 20 possible combinations of electrical conductor and insulator pairs, three of the pairs would fail due to thermal mismatch under the peak reentry heat flux conditions, and three pairs would fail due to thermal mismatch under the average reentry heat flux conditions. However, because the thermal mismatch analysis considers the worst-case scenario thermal expansion conditions, the material pairs that appear to fail under the current assumptions would need to be modeled more precisely in future work to obtain more conclusive results. The thermal analysis can continue in future work to account for the actual geometry of the MEMS Langmuir probes, and also consider radiation.

While Pyrex has the lowest melting temperature and thermal conductivity of all the candidate materials considered, we speculate that it may be possible for properly cooled Pyrex probes to survive reentry. Moreover, if analyses conducted in future work conclude that Pyrex is not a suitable choice for reentry, leveraging the MEMS Langmuir probe technology to the other candidate materials should be feasible since the batch-microfabrication process we developed is robust and allows different materials to be interchanged. Finally, the MEMS Langmuir probe technology can provide diagnostics for other applications such as tokamaks and nanosatellite scientific payloads. Probes made from Pyrex would represent an advance in the state-of-the-art because the only reported MEMS Langmuir probes utilize polymer insulators [21,26] that have a lower melting temperature compared to Pyrex.

## 3.3 Plasma Dynamics Considerations

The design of the MEMS Langmuir probes also considers the interaction of the Langmuir probe with the reentry plasma. In Chapter 2 it was pointed out that the relationship between the dimensions of the Langmuir probe and the Debye length strongly influence the performance of the probe and the data analysis. In particular, a Langmuir probe would be less likely to perturb the plasma if its diameter is smaller than the Debye length; also, the plasma sheath surrounding a Langmuir probe would interfere with neighboring probes if the probes are spaced closer than 3 Debye lengths apart. Therefore, literature was surveyed to assess the range of the reentry plasma Debye length, and the probes were designed accordingly.

Three RAM-C reentry flight experiments, conducted by the NASA Langley Research Center between 1967 and 1970, utilized Langmuir probes to take measurements of the reentry plasma in the aft flow field of the vehicle. Each payload had a hemispherical nose having a radius of about 6 inches, a $90^0$ half-angle conical body, and an overall length of about 51 inches [18]. A basic diagram of the RAM-C reentry vehicle, with the Langmuir probe location indicated, is shown in Figure 3.5. One of these experiments, i.e., RAM-CII, did not include an ablative heat shield. Therefore, the aft flow field of the RAM-CII reentry vehicle was relatively free of ablation contaminants and the measured plasma could be used to compare with "clean air" theoretical calculations [18]. In general, the measurements from RAM-CII have proven very valuable for determining the validity of numerical plasma models, and for correlation with other in-flight diagnostic measurements. Accordingly, the RAM-CII data was also used to determine the electron Debye lengths that the MEMS Langmuir probes would likely experience during reentry. As plotted in Figure 3.6, the electron Debye length measured by the RAM-CII experimental vehicle ranged from about 3.5–300 μm during reentry, corresponding to altitudes from 57 to 82 km. [18]. Therefore, a probe diameter of about 3 μm or less and a probe-to-probe separation of no less than about 900 μm apart, would meet the design requirements specified at the beginning of this section. These dimensions will be contrasted with the capabilities of the microfabrication techniques available for this project.

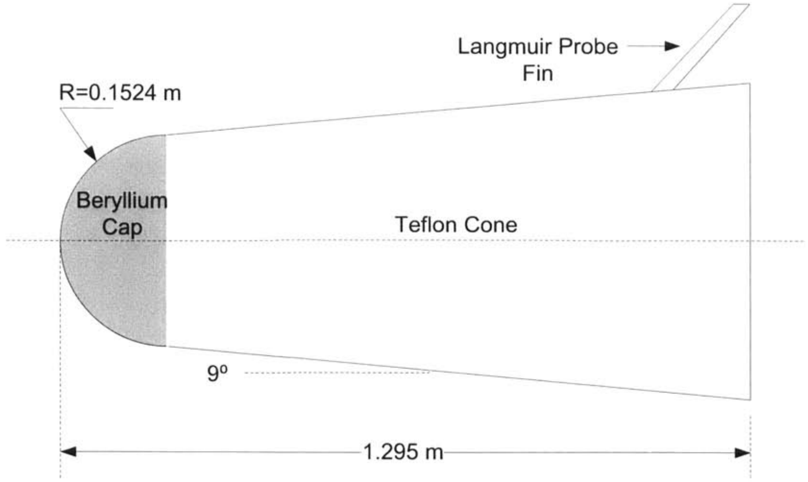

Figure 3.5: RAM-C Experimental Reentry Vehicle with Langmuir Probes in Aft Flow Field [18].

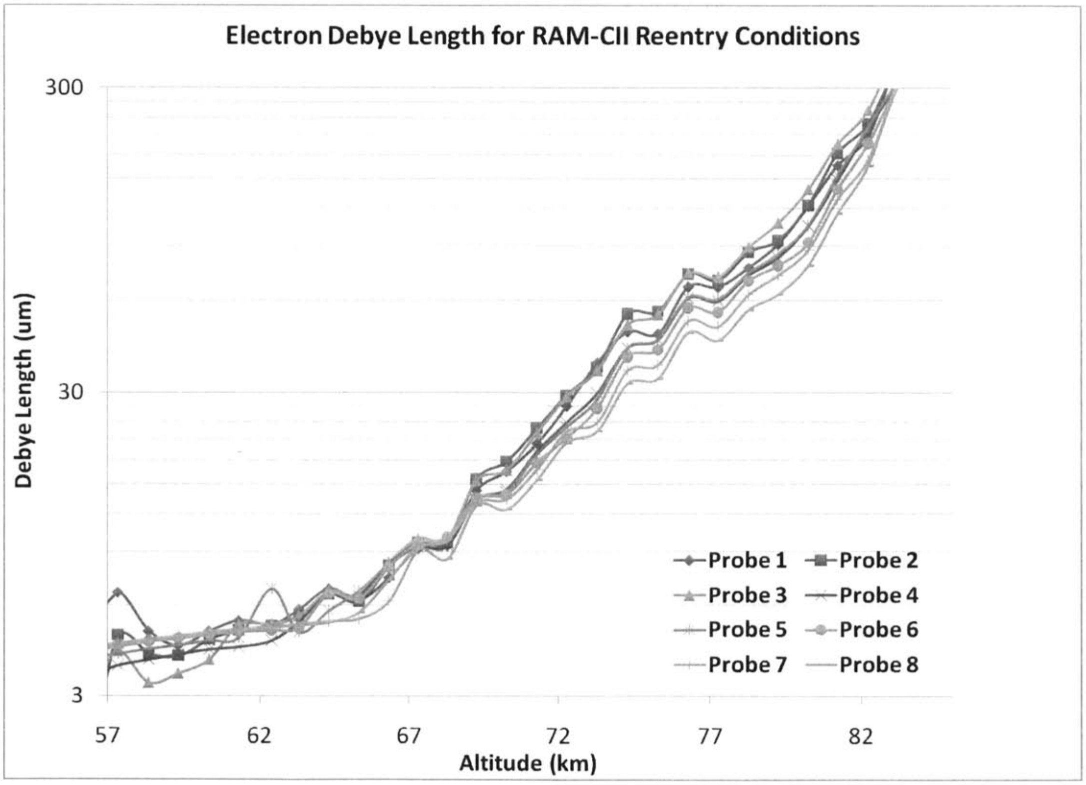

Figure 3.6: The electron Debye length calculated from the RAM-CII Langmuir probe reentry data [18].

## 3.4 Batch-Microfabrication Considerations

The purpose of this thesis is to demonstrate low-cost, miniaturized plasma sensors for space applications that contribute to the paradigm shift in space technology, where missions are visibly smaller, inexpensive, and high performance. Batch-microfabrication is the method proposed in this thesis to manufacture plasma probes that align with this thinking. This section documents the batch-microfabrication considerations that led to the design and manufacturing process of the MEMS Langmuir probes. The design objective of the MEMS Langmuir probes is to construct flat, planar arrays of probes that can be blended onto the outer surface of a reentry vehicle or miniaturized satellite as a sensorial skin. This translated to the design concept of patterning arrays of through-holes in an electrically insulating flat plate, and filling in each hole with an electrically conductive material to form individual probes. The MEMS Langmuir probe design concept is pictured in Figure 3.7. The selection of a batch microfabrication process for developing the MEMS Langmuir probes will begin with a discussion about the options for patterning holes in the electrically insulating flat plate.

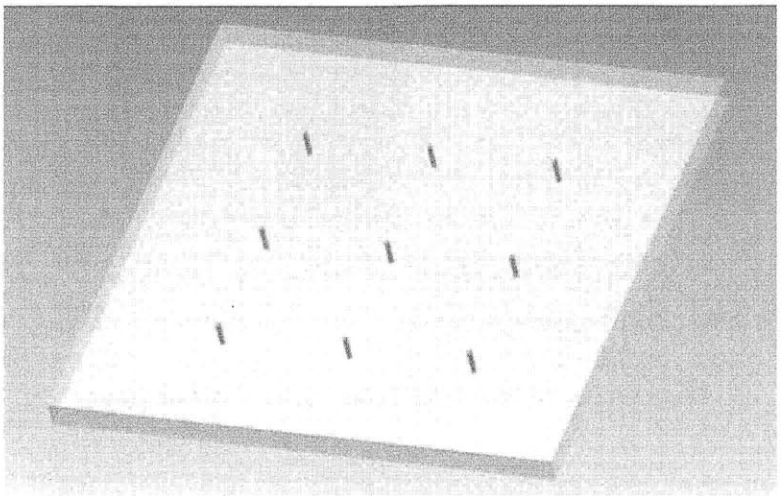

**Figure 3.7: MEMS Langmuir probe design concept showing 9 holes in an electrically insulating flat plate that have been filled in with an electrically conductive material. Each filled hole is an individual MEMS Langmuir probe.**

Three different options were available through both MIT and industry vendors for patterning through-holes (vias) in an electrically insulating flat plate (dielectric substrate). These options included deep-reactive-ion-etching (DRIE), ultrasonic drilling, and laser drilling. A summary of the relevant specifications of each option is provided, followed by an explanation of the down-selection process:

- DRIE is capable of producing holes in silicon wafers that have an aspect ratio of about 1:15. Therefore, the smallest hole that could be produced in a typical 650 $\mu$m-thick silicon wafer would have a diameter of about 43 $\mu$m if the etch is conducted from only one side of the wafer. Using the Bosch process, the holes can have straight or tapered sidewalls, from $0^0$ to $36^0$ depending on the process parameters [46]. Spacing the holes at least 900 $\mu$m apart according to the Debye length considerations is also achievable. However, because silicon is a semiconductor, a dielectric coating would be required after DRIE to meet the requirements of a dielectric substrate.
- Ultrasonic drilling is capable of producing holes in dielectric substrates having diameters as small as 100 $\mu$m, and an aspect ratio of 1:5. Tapered sidewalls up to $30^0$ can be drilled into glass materials such as Pyrex and fused silica, while holes with straight sidewalls can be drilled into other dielectric materials such as un-doped silicon carbide and alumina. The holes can be spaced as close as 1.6 mm apart.
- Laser drilling can in theory produce as small as 100 $\mu$m-diameter tapered holes in dielectric wafers with an aspect ratio of 1:5, similar to ultrasonic drilling. However, laser drilling such small holes at MTL is not an established process so it might require substantial process development.

Drilling of dielectric substrates had lower risk compared to DRIE. While DRIE can produce the smallest diameter holes of all the processes considered, the requisite dielectric coating poses a reliability concern. Coatings have a tendency to peel off silicon wafers, especially due to erosion or stress from thermal cycling. If the dielectric coating peels off, the probes are no longer electrically insulated from each other and they will not operate properly. Because the MEMS Langmuir probes would be operated in plasma environments, thermal cycling and erosion is unavoidable. Also, the high vacuum and particle and photon fluxes in low Earth orbit induce material sputtering [47], and in the case of the Space Shuttle, the probes would be impinged by solid rocket fuel and sea salt at the launch site [43]. Ultrasonic drilling was the lowest risk approach because it was an established process for many different dielectric materials, including the candidate materials considered in the reentry heat transfer analysis. In addition, the process is inexpensive compared to laser machining because it is done in parallel (i.e., all the holes of a substrate can be patterned at the same time), and provides the option for vias with tapered sidewalls. Moreover, ultrasonic drilling produces cleaner holes compared to laser drilling.

The considerations of the plasma Debye length led to a concept of 3 μm-diameter MEMS Langmuir probes, separated by at least 900 μm. The ultrasonic drilling process cannot achieve these dimensions; 100 μm is the smallest diameter that can be drilled (for wafers that are thinner than 0.5 mm), and 1.6 mm is the smallest pitch. Nonetheless, MEMS Langmuir probes having these larger dimensions are still viable because the plasma sheath would be defined by the spacecraft surface instead of the probes. In other words, the plasma would not be perturbed by the larger MEMS Langmuir probes because of their planar, flat construction, which would not protrude into the spacecraft's plasma sheath.

The ultrasonic drilling process can produce holes with straight or up to $30^0$ tapered sidewalls. Tapered sidewalls were selected because we speculated that this geometry would be easier to fill in with an electrically conductive material without the formation of voids. This is because tapered sidewalls provide a measure of horizontal surface area within the line of sight of a deposition along a direction perpendicular to the substrate surface. The tapered ultrasonic drilling process is compatible with glass materials such as Pyrex and fused silica. We opted for Pyrex because of its low cost, wide availability, and relative ease to drill compared to fused silica. Even though Pyrex has the lowest melting temperature of all the candidate materials and a cooling system would be required for reentry applications, Pyrex will not melt in VTF's plasma environment due to the 20-ms duration of the plasma shots. Hence, Pyrex was an appropriate material for constructing proof-of-concept MEMS Langmuir probes that could be tested and validated in a laboratory plasma. In future work, more resilient materials such as silicon nitride or alumina could be substituted for operation in harsher environments.

The final design choice is the selection of the electrically conductive material to fill in the vias in the Pyrex substrate. The reentry temperature analysis considered the performance of tungsten, silicon carbide, gold, and nickel, due to their high melting temperatures and our ability to deposit these materials at MTL or other MIT labs. A summary of the considerations of each option is provided, followed by an explanation of the down-selection process:

- Tungsten can be sputtered at MTL at a deposition rate of about 0.1 – 0.2 nm/second; therefore, to fill the 100-μm diameter holes, a layer of tungsten at least 50 μm thick would be required, resulting in a deposition time of about 139 hours –almost a week-long deposition. In addition, from experience we know that thick sputtered tungsten films crack due to stresses. Therefore, sputtered tungsten was ruled out as an option for the MEMS Langmuir probes.
- Silicon carbide (SiC) can be deposited at MTL using plasma enhanced chemical vapor deposition (PECVD) at a rate of about 0.1 μm/minute; therefore, a 50-μm deposition would therefore require about 8.3 hours. However, PECVD SiC poses several challenges. One concern is the electrical

conductivity of the film; although electrically conductive PECVD SiC can be deposited under some conditions [48], we were unable to replicate the results found in literature; our attempt to develop conductive PECVD SiC has been documented in more detail in Chapter 4. In addition, we found that the PECVD SiC films peeled off our wafers during the annealing process. In general, the main difficulty associated with depositing thick films through thin-film techniques is the large stresses they have, which tend to cause cracking and delamination of the film. Therefore, PECVD SiC was also ruled out as a candidate material for the fabrication of MEMS Langmuir probes. However, it would be relevant in future work to consider non-conductive SiC substrates as a substitute for Pyrex in high temperature applications for MEMS Langmuir probes.

- Gold was a promising candidate for filling in the vias because it can be electroplated to thicknesses of more than 125 μm, which is sufficient to fill in the largest vias we had in our design. Also, gold has excellent corrosion resistance, thermal conductivity, and electrical conductivity. The primary advantage of gold was our access to a MEMS electroplating tool at MIT's Lincoln Laboratory (Lexington, MA), which has a tuned gold electroplating process that we could leverage for our needs. The "Iko" tool at Lincoln Laboratory electroplates gold onto a gold seed layer. Several experiments were performed using the Iko tool to develop a process for filling in vias having a gold seed layer, which have been documented in Chapter 4. However, completely filled-in vias were not produced as a result of these experiments because the plating rate in our experiments was slow and the process readily consumed plating chemicals.
- Like gold, nickel was a promising choice because it can be electroplated easily to thicknesses of more than 125 μm, which is sufficient to fill in the largest vias we had in our design. Also, nickel has excellent corrosion resistance and electrical conductivity, and has a higher melting temperature compared to gold. Moreover, nickel is cheaper than gold, and it can be electroplated using an autocatalytic (electroless) process, which produces a smoother surface texture compared to electroplated gold. Like electroplated gold, electroless nickel requires a gold seed layer. However, because our electroless nickel plating equipment was not designed specifically for MEMS applications, it was unclear whether electroplated nickel could fill in vias as small as 100 μm in diameter. Therefore, we first explored outsourcing the nickel plating process. After discarding this possibility, we pursued electroless nickel in our own laboratory, and from experimentation, presented in Chapter 4, we confirmed that electroless nickel plating can fill in the vias. In addition, the deposition rate of electroless nickel was faster compared to electroplated gold using the Iko tool.

Arrays of different sizes and diameters were fabricated to explore the MEMS Langmuir probe technology. For example, denser arrays of smaller diameter probes would be more suitable for measuring plasmas with smaller Debye lengths, such as tokamak plasma, ionospheric plasma, or the reentry plasma sheath at lower altitudes. Conversely, larger diameter probes in less dense arrays would be more suitable for measuring the reentry plasma sheath at higher altitudes, or for miniaturized satellites to characterize the plasma environment in low Earth orbit [49]. The MEMS Langmuir probes were designed in arrays containing $2\times2$, $4\times4$, or $5\times5$ probes. The separations between the probes in these arrays are 4, 2, and 1.6 mm, respectively (the maximum probe density would be 39 probes/cm$^2$ if the probes are arranged in square packing). The diameters of the probes are 100, 150, 200, or 250 μm with 30$^o$ tapered sidewalls, all produced by ultrasonic drilling into Pyrex wafers. The Pyrex wafers were 100 mm in diameter and they were divided into 1 cm-square dies, with each die containing a single probe array, i.e., 60 arrays per wafer. A summary of the material and geometrical selections of the MEMS Langmuir probes are presented in Table 3.8.

| **Table 3.8: Material and Geometry Selections of the MEMS Langmuir Probes** | | | |
|---|---|---|---|
| **Material Selections** | | | |
| Planar Dielectric Substrate | 100 mm Pyrex wafer | | |
| Metal Probe Material | Electroless nickel on gold seed layer | | |
| **Geometry** | | | |
| **Array Size** | **2×2 (4 probes)** | **4×4 (16 probes)** | **5×5 (25 probes)** |
| Via Diameter ($\mu$m) | 100, 150, 200, 250 | 100, 150, 200, 250 | 100, 150, 200 |
| Taper | 30° | 30° | 30° |
| Pitch (mm) | 4 | 2 | 1.6 |
| Arrays per Wafer | 32 | 16 | 12 |
| Maximum Density (probes/cm$^2$) | 4 | 25 | 39 |

## 3.5 Chapter 3 Summary

In this chapter, the design specifications of the MEMS Langmuir probes were determined based on heat transfer, plasma, mechanical, and microfabrication considerations. The proposed MEMS Langmuir probes are composed of a Pyrex flat plate having ultrasonically drilled tapered vias filled in with electroless nickel. Each nickel-filled via is an individually addressable Langmuir probe. The diameter of the probes range from 100 – 250 $\mu$m, and are arranged in arrays of 2×2, 4×4, and 5×5 probes. The separations between probes in these array sizes are 4, 2, and 1.6 mm, respectively. The fabrication steps of this MEMS Langmuir probe design concept are documented in Chapter 4, and the driving electronics are documented in Chapter 5.

# 4 Fabrication of the MEMS Langmuir Probe Arrays

In this chapter the fabrication of the MEMS Langmuir probes is documented, including the experimental investigations that led to the selection of the material and process for manufacturing the conductive core of the probes. As specified in Chapter 3, the proposed design of the MEMS Langmuir probes consists of metalized tapered vias embedded in a Pyrex planar substrate (Figure 4.1). Therefore, the key fabrication challenges of the MEMS Langmuir probes are

(a) Patterning arrays of tapered vias in the Pyrex substrate using a batch-microfabrication process, and

(b) Developing a batch-microfabrication process to fill in the vias with metal

The process to pattern arrays of tapered vias into Pyrex substrates was outsourced to the company Bullen Ultrasonics (Eaton, OH). The company patterned the substrates using our layout and a proprietary ultrasonic drilling process. Several electrically conductive materials were explored for filling in the vias, including PECVD doped silicon carbide, electroless nickel, and electroplated gold. From experiments we determined that plating electroless nickel was the most suitable process for making filled-in vias. Section 4.1 describes the fabrication aspects of the Pyrex wafer; Section 4.2 focuses on the experimental investigations that led to the selection of electroless nickel for filling in the vias; Section 4.3 presents the final microfabrication process and Section 4.4 summarizes the final microfabrication results.

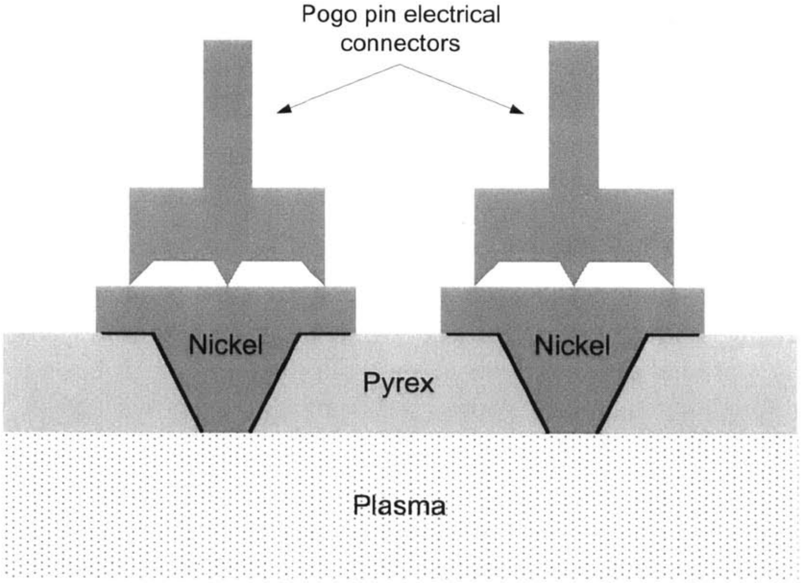

**Figure 4.1: Schematic cross section of a Langmuir probe array in plasma with pogo pin electrical connectors on the opposite side. The taper of the vias facilitates the deposition of the seed metal into the vias.**

## 4.1 Pyrex Substrate Design and Processing

The fabrication process of the multiplexed MEMS Langmuir probes began with 100 mm-diameter, 0.5 mm-thick Pyrex (Corning 7740) wafers patterned with various arrays of tapered vias; the dies were 1 cm-wide squares and each die contained an array of $2\times2$, $4\times4$, or $5\times5$ vias with $30^0$ taper. The diameter of the narrow side (i.e., plasma side) of the tapered vias ranged from 100 to 250 $\mu$m. The spacing between the vias in the $2\times2$, $4\times4$, and $5\times5$ arrays were 4 mm, 2 mm and 1.6 mm, respectively. Each Pyrex wafer had 60 dies in total. The dies were small enough to fit through the dedicated ports in the VTF after being packaged for characterization. A summary of the different die configurations that were included in the layout is shown in Table 3.8 (see Chapter 3). The fabrication of the MEMS probes continued by sawing the Pyrex wafers into dies; we die-sawed the wafers to increase the number of samples per wafer available to the filling-in experiments. In order to accurately diesaw the Pyrex wafers, contact photolithography on an airbrushed photoresist film was conducted to define diesaw lines onto the Pyrex wafer. The die-sawing process yielded 9.76 mm-square dies because the die-saw blade was 0.24 mm thick and the original die pitch was 10 mm. The layout of vias that were ultrasonically drilled into the Pyrex wafer included features to make the alignment between the contact mask and the wafer feasible. The wafers were coated with photoresist on both sides to protect the Pyrex from particle contamination during the die-sawing process. A photo of the dies after sawing is shown in Figure 4.2.

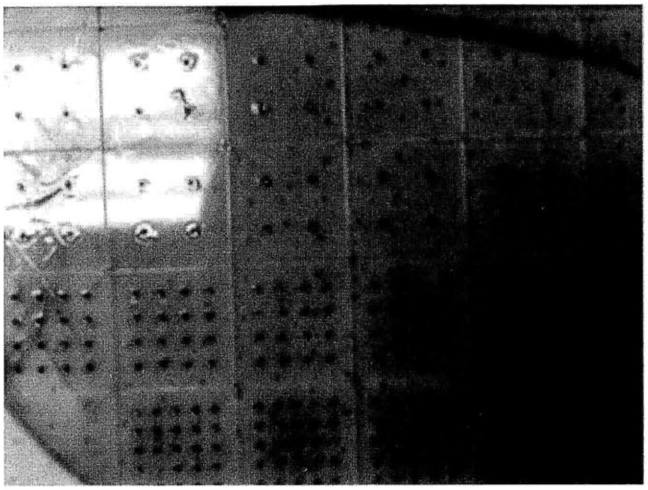

**Figure 4.2: Pyrex wafer after die-sawing. As reference, each die is a square, 1 cm-wide. The dies appear attached to each other because the wafer was attached to an adhesive backing during the die-sawing process.**

## 4.2 Via Metallization Process Development

The fabrication of the MEMS Langmuir probe arrays requires the deposition of thick films that are electrically conductive and conformal; for example, films at least 50 μm thick are required to fill in the 100 μm-diameter vias, and similarly, films at least 125 μm thick are required to fill in the 250 μm-diameter vias. Therefore, after surveying the microfabrication methods available at MTL, we decided to explore electroplating methods to fill in the vias.

Electroplating requires a metal seed layer on top of the area to be electroplated. Typically, sputtered or evaporated gold is chosen as a seed layer due to its high purity, low chemical reactivity, and high electrical conductivity; in our case, we sputtered a gold seed layer because we knew from prior experience that sputtered films have better conformality than evaporated films. However, gold does not adhere well to Pyrex; therefore, a titanium adhesion layer was sputtered onto the Pyrex vias before the gold deposition. We used tapered holes to make sure that the sidewalls of the vias were completely coated, and also to prevent the creation of voids that disconnected the upper metallization (in contact with the pogo pins) from the lower metallization (in contact with the plasma). Bullen's technology can pattern holes in Pyrex with up to 30° taper; we specified the vias with the maximum taper to increase the odds of success in the filling-in process. A shadow mask was used to deposit the metal seed only into the vias. The shadow mask, pictured in Figure 4.3, allowed the processing of up to 16 Pyrex dies at the same time. A concept drawing of the sputtering process using the shadow mask is shown in Figure 4.4. Several experiments were conducted to estimate the best electrodeposition approach, and we also explored coating the metallization with silicon carbide for enhanced protection using plasma enhanced chemical vapor deposition (PECVD). The final version of the process flow is reported in Section 4.3.

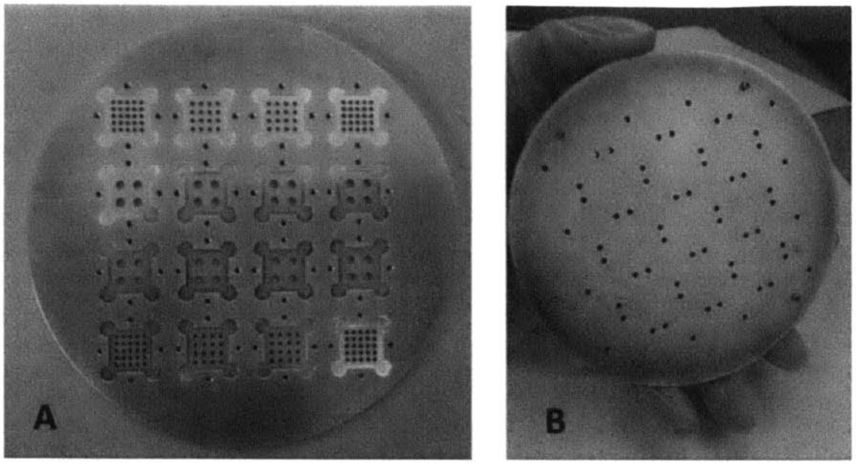

**Figure 4.3: Aluminum shadow mask for sputtering titanium and gold into the Pyrex vias (A). The shadow mask worked together with a fastening plate (B).**

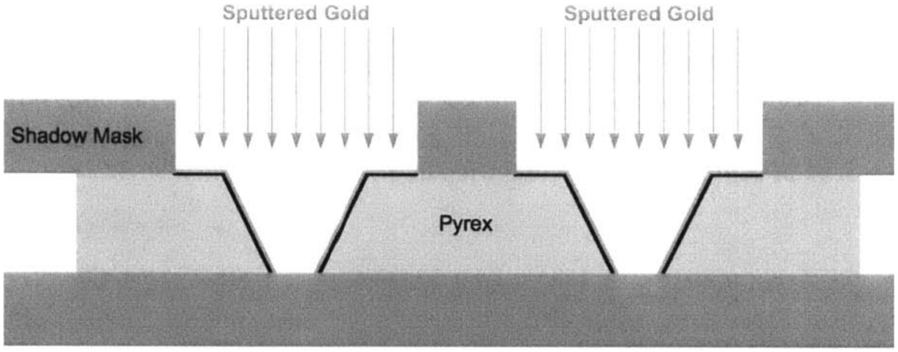

**Figure 4.4: Cross section of the concept of using a shadow mask to fill in vias with a metal seed.**

### 4.2.1 Exploration of Silicon Carbide Coatings for Metalized Vias

Doped silicon carbide (SiC) was explored as a coating material of the MEMS Langmuir probes due to its high melting temperature (2730 °C), low electrical resistance, and great chemical stability [50]. The vias could then be filled in later with electroplated metal, as shown in Figure 4.5. A literature search was conducted to assess whether it would be possible to replicate existing processes for doped SiC films in our fabrication facility. In one reference, SiC films were doped to a resistivity of almost 0.1 Ω cm during a low pressure chemical vapor deposition (LPCVD) process that occurred at a relatively high deposition temperature of about 800 °C [51]. These SiC films were doped with gaseous $NH_3$ (5% in $H_2$) as a precursor for nitrogen. In another reference, PECVD SiC films were doped using ion implantation followed by annealing at 1100 °C for 2 hours, resulting in a resistivity of about 0.1 Ω cm [48].

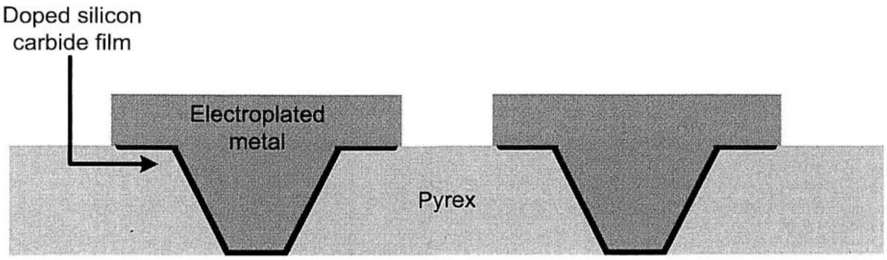

**Figure 4.5: Doped silicon carbide film could be used to protect the metallization against the harsh reentry plasma.**

We preliminarily explored the development of a doped PECVD SiC film recipe by modifying an undoped PECVD SiC process available at MTL. In these experiments the SiC films were deposited onto silicon wafers with 1 μm of thermal oxide so that the electrical conductivities of the films could be measured. The preparation of the samples started with 150 mm n-Si <100> wafers that were RCA cleaned. Then, 1 μm of thermal oxide was grown at 1050 °C. Shortly before the SiC deposition, the wafers were broken into smaller pieces and cleaned in piranha solution (i.e., a 3:1 mixture of sulfuric acid and hydrogen peroxide) to remove organic contaminants. In the PECVD reactor (ST Systems), the PECVD SiC films were deposited from appropriate gaseous mixtures of methane (310 sccm), argon (700 sccm), silane (45 sccm), and phosphine (2%, 22 sccm; phosphine was the doping gas) while the wafer pieces were maintained at a temperature of approximately 300 °C. The deposition rate was approximately 0.1 μm/min. PECVD SiC films having thicknesses between 0.5 μm and 3 μm were deposited onto both sides of the wafer pieces to compensate the stress. A portion of the samples was annealed at 650 °C or 950 °C in nitrogen for 30 minutes directly following deposition. Figure 4.6 summarizes the matrix of combinations that we tried in these experiments.

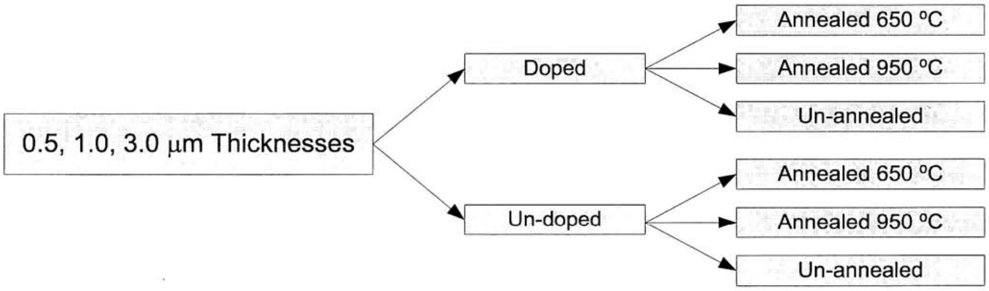

**Figure 4.6: Doped and un-doped SiC films were deposited at various thicknesses and annealed at various temperatures for 30 minutes. A total of 18 samples were processed.**

All of the SiC films thicker than 0.5 μm delaminated during annealing. Delamination may have occurred due to stress from thermal expansion and/or excessive annealing temperature ramp-up rate. The electrical conductivities of the remaining samples (un-annealed films and 0.5 μm-thick annealed PECVD SiC films) were measured with a 4-point probe. The measurements indicated that all samples were electrical insulators. A likely explanation for this result is that the deposition temperature was too low for the SiC to form crystalline structures, and therefore, there were not enough vacancies for dopants to be incorporated. Furthermore, the 4-point probe measurements on the surviving annealed samples indicated that annealing did not help improve the electrical conductivity of the SiC film. Therefore, although doped SiC films have been produced by others [48,51], we were unable to replicate the results in our facility and further investigations are needed to accomplish this.

### 4.2.2 Exploration of Electroplated Gold for Metalized Vias

We decided to explore gold electroplating to fill in the vias because of three key reasons. First, gold has excellent electrical and thermal conductivity and it also has excellent corrosion resistance. Second, the inertness of gold prevents the formation of electrically insulating surface oxides that could interfere with the operation of the probes. Third, electroplated gold serves a variety of functions in the microelectronics industry and therefore, it is a mature microfabrication process. This section describes the experiments we conducted to develop a gold electroplating step to fill in the vias.

An "Iko" tool from ElectroChemical Systems, Inc (Knoxville, TN) was utilized for the gold electroplating experiments. The tool is located at MIT's Lincoln Laboratory. The tool consisted of a 63 $^{0}$C temperature-controlled plating bath in a ventilated enclosure. A wafer holder connected to the cathode was immersed in the bath, and the anode was connected to a reciprocating device hovering in the bath above the wafer. The reciprocating anode is a specialized apparatus that pulses the plating solution near the wafer's surface, helping to remove air bubbles and improve the quality of the electroplated gold. The plating bath consisted of Techni Gold 434HS solution from Technic, Inc. (Cranston, RI), which is a premixed solution that electroplates onto surfaces having a gold seed layer. The specifications of the gold plate include 99.99% purity, 0.3 m$\Omega$/cm$^2$ contact resistance, and 18.5 g/cm$^3$ density. Plating was performed at the recommended current of 3 Amps/ft$^2$. The tool is specifically tailored for MEMS processes, but at that time there was no in-house recipe developed for filling in vias.

The first experiments involved Pyrex dies that were field coated with a sputtered film stack of titanium (0.05 $\mu$m) and gold (0.25 $\mu$m); the dies were coated on the surface that would not be exposed to the plasma (this would result in connected probes after electroplating). The shadow mask was introduced in subsequent experiments to deposit the seed layer only into the vias. In all experiments the dies were affixed to a 150 mm-diameter silicon handle wafer using electroplating tape (3M 470). The handle wafer was coated with a similar sputtered film stack to provide electrical contact between the Iko's wafer holder and the vias.

In the first electroplating experiment, four Pyrex dies were affixed to a handle wafer. The remaining exposed area of the handle wafer, minus a 0.5 cm-border left for electrical contact between the wafer and the holder, was hand-painted with AZP4620 photoresist and then baked for 1 hour at 90 $^{0}$C. After electroplating for approximately 18 hours, much of the photoresist peeled off and clogged the plating bath's filtration system; this also caused gold to plate on areas of the handle wafer, resulting in depletion of the gold electroplating solution. Nonetheless, examination of the vias with scanning electron microscopy (SEM), shown in Figure 4.7, confirmed that it is possible to conformally electroplate gold within the vias to form probe structures. The deposition rate was approximately 17 $\mu$m/hr on the surface of the dies, but much slower within the vias, suggesting a species depletion mechanism in the deposition similar to microloading in plasma etching. This experiment yielded partially filled-in vias but longer plating times should result in completely filled-in vias.

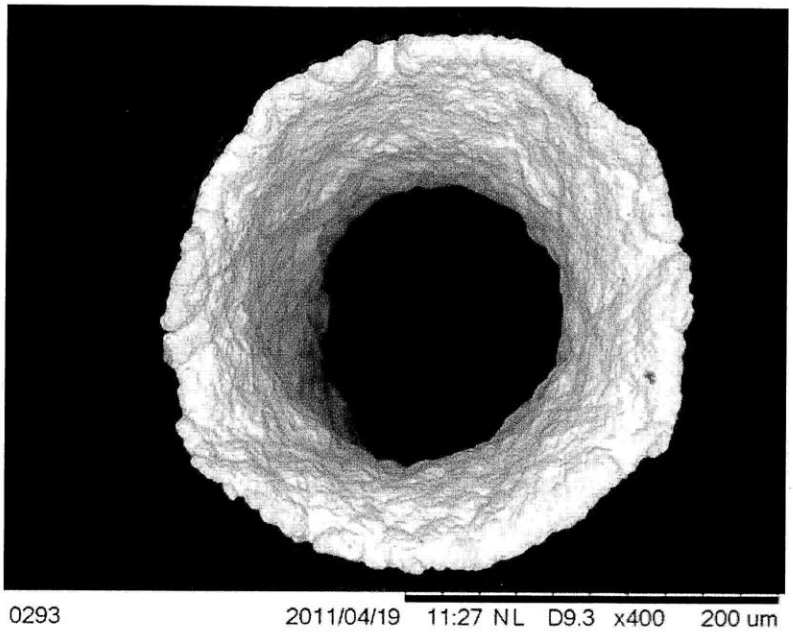

**Figure 4.7: SEM of electroplated gold inside a via as seen from the plasma side from the first electroplating experiment, demonstrating the conformality of the deposited film.**

A second electroplating experiment was carried out for 22 hours and 21 minutes. The second experiment was identical to the first experiment except that in this experiment 9 dies were involved and the exposed surface of the handle wafer was covered with electroplating tape instead of photoresist, as shown in Figure 4.8.A. Unfortunately, the electroplating tape was not as effective as hoped in stopping electroplating of the unwanted areas. As shown in Figure 4.8.B, many areas beneath the tape were electroplated, particularly the areas where the electroplating tape was overlapped. For this reason, all the dies of the second experiment firmly attached to the handle wafer. The handle wafer was etched away using an $SF_6$-based plasma recipe in a deep-reactive-ion-etching (DRIE) tool; approximately 2.5 hours were required to etch the handle wafer (the handle wafer was about 650 µm thick). In future experiments care was taken to not overlap the electroplating tape, which allowed the dies to be dismounted from the handle wafer with ease.

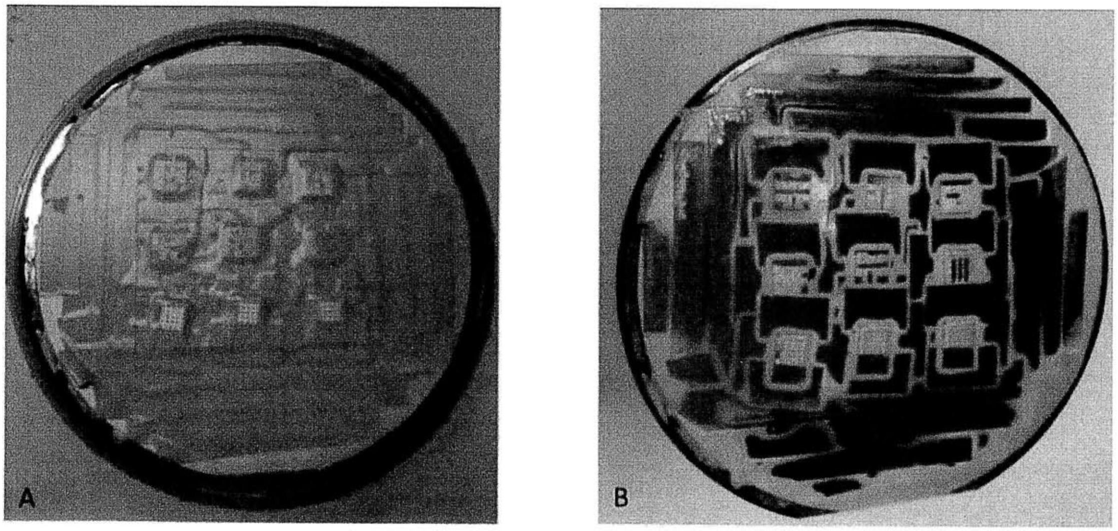

**Figure 4.8: (A) Sample used in the second experiment before plating. (B) Sample used in the second experiment after plating and removal of the electroplating tape. Electroplating occurred in some of the areas masked by the tape.**

A third electroplating experiment was conducted, this time including dies that were processed using the shadow mask shown in Figure 4.3. The shadow mask allowed the titanium/gold film stack to be sputtered only into the vias, electrically isolating each via (Langmuir probe) from the others. The third experiment was unsuccessful at filling in the vias using electroplated gold. This result was caused by lack of electrical connection between the seed layer in the vias and the seed layer on the handle wafer. Although we knew that there was no electrical connection between the vias and the handle wafer before the electroplating had begun, we had hoped that the electroplating process would cause gold to plate upwards from the seed layer on the handle wafer and into the vias, eventually making electrical contact with the vias. However, this was not the case. After approximately 7.5 hours of plating, there was still no electrical contact between the vias and the handle wafer. Worse yet, because there was no electrical contact, the gold plating solution etched away the gold seed layer, exposing the titanium adhesion layer. This occurred because the gold electroplating solution contains cyanide, which has the ability to etch gold when electroplating is not taking place. The exposed titanium adhesion layer can be seen on the dies pictured in Figure 4.9. Based on this experiment, we conclude that a sufficient electrical connection between the bottom of the dies and the handle wafer is required in order to successfully electroplate into the vias. This can be achieved by either bonding the dies to the handle wafer (thermal compression), or, by coating the surface of the dies that makes contact with the handle wafer with a sputtered titanium/gold film stack.

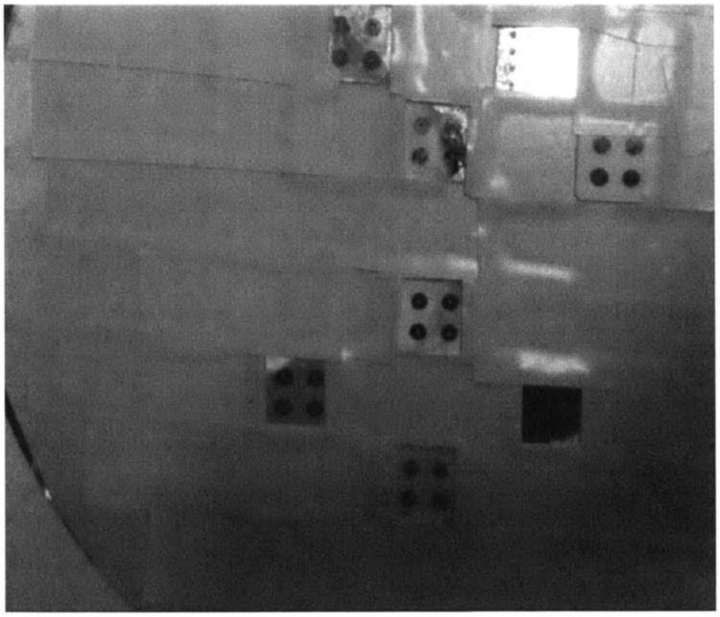

**Figure 4.9: Dies with exposed titanium film due to etching of the gold electroplating seed layer.**

A fourth gold electroplating experiment was conducted; in this case, the surface of the dies that makes contact with the handle wafer was coated with a sputtered titanium/gold film stack to facilitate the electrical contact between the dies and the handler wafer. As shown in Figure 4.10, at the end of this experiment the vias were not completely filled-in. The process concluded prematurely after approximately 13.5 hours because the gold in the electroplating solution had depleted. For this reason, the electroplated gold shown in Figure 4.10 has a rough appearance.

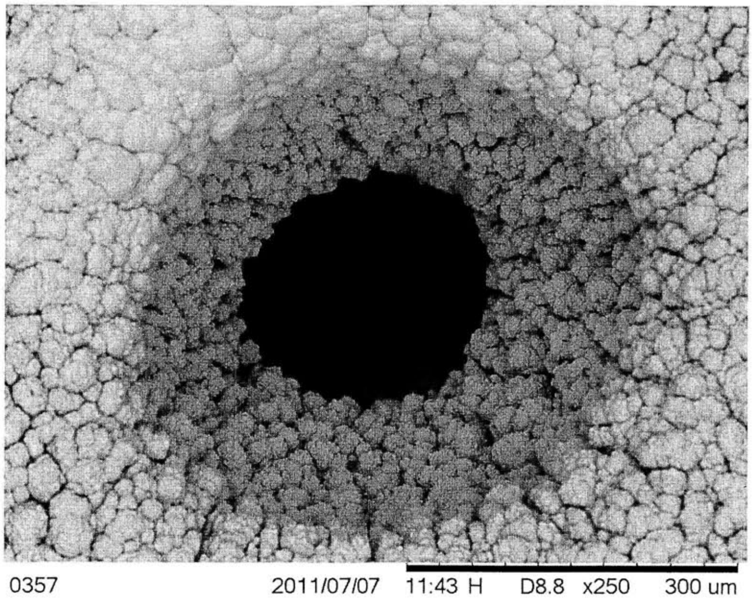

**Figure 4.10: SEM of the gold metallization inside a via produced by the fourth electroplating experiment. The rough appearance of the gold is a result of the depletion of gold in the electroplating solution.**

We also contemplated using electroless gold to fill in the vias. Electroless (autocatalytic) plating involves the presence of a chemical reducing agent in solution to reduce metallic ions to the metal state [52]. Electroless plating does not require external electrical power: instead of having an anode, the metal is supplied by a metal salt in aqueous solution; instead of having a cathode to reduce the metal, there is an electrically conductive substrate to serve as the cathode, while a reducing agent in the aqueous solution provides electrons. Electroless plating only takes place on catalytic surfaces such as gold, rather than occurring throughout the entire solution, which is ideal for our shadow mask approach. However, a brief exploration of the electroless gold process revealed that it would not have been viable for filling in relatively large, 100 μm-diameter vias. Specifically, the deposition rate of electroless gold is comparatively low (0.1 μm/hour), the plating baths tend to have short lives (15 minutes), and the thickness of the deposition is sensitive to stirring [53,54].

### 4.2.3 Exploration of Electroless Nickel for Metalized Vias

Electroless plating of nickel was explored to fill in the vias of the MEMS Langmuir probes. The potential advantages of electroless nickel plating include lower porosity compared to traditional electroplating and hence better corrosion resistance [52]. The chemicals for plating electroless nickel were procured from Caswell, Inc. (Lyons, NY). These chemical solutions included nickel sulfate (i.e., Part A), and the reducing agent composed of sodium hypophosphite and ammonium hydroxide (i.e., Part B). The chemical formulas and pH of Part A and B can be found in Table 4.1. The composition of the plating bath was specified by the volume ratio of 1:3:16 of Part A, Part B, and distilled water, respectively. Electroless nickel plating occurs at approximately 90 °C, just below the boiling point of the solution. An immersion heater provided by Caswell, Inc. was placed at the bottom of the plating bath to maintain a temperature of approximately 90 °C during the plating process. A thermocouple provided feedback to ensure the temperature within the bath was relatively stable and uniform, within plus or minus 2 °C of the 90 °C set point. In addition, mist control balls, which can be seen in the laboratory setup in Figure 4.11, were used to help decrease the evaporation rate of the plating chemicals and contain heat within the plating bath.

**Table 4.1: Components of Electroless Nickel Solution**

| Solution Name | Chemical Formula | pH |
|---|---|---|
| **Part A:**<br>Nickel Sulfate (45 wt %) | $NiSO_4.(H_2O)_6$ | 3.5 |
| **Part B:**<br>Sodium Hypophosphite (25 wt %)<br>Ammonium Hydroxide (1 wt %) | $NaH_2PO_3.H_2O$<br>$NH_3$ | 5.5 |

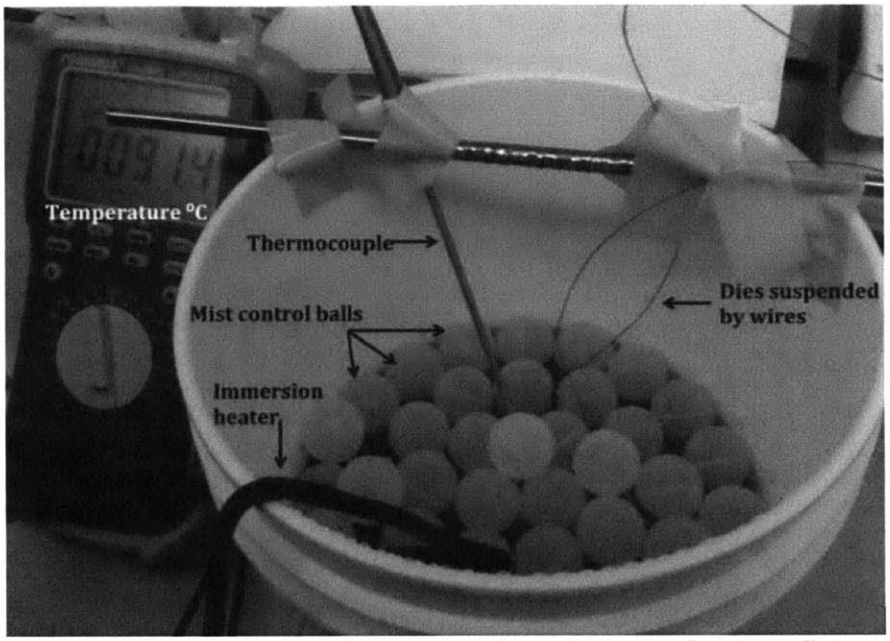

Figure 4.11: Laboratory setup of electroless nickel plating process from Caswell, Inc.

We conducted an electroless nickel plating experiment using Pyrex dies that had been processed at Lincoln Laboratory (i.e., the electroplated gold from Lincoln Laboratory served as a seed layer for the electroless nickel process). After the gold electroplating process at Lincoln Laboratory partially filled in the vias, the dies were dismounted from the handle wafer by removing the electroplating tape. Then, photoresist was painted onto the top of the dies and soft-baked. The gold film on the plasma side of the die was then etched using Transene TFA (etch rate 28 A/sec @ 25 °C), and the titanium adhesion layer was etched away using Transene TFTN (etch rate 50 A/sec @ 85 °C). The photoresist was then removed with acetone, after which the die was rinsed in deionized water and dried with a nitrogen gun. Finally, the dies were suspended into the bath using a wire sling and electroless nickel plating was conducted. The electroless nickel plating process was performed for 2 hours.

Electroless nickel plating occurs on catalytic surfaces such as gold, hence the handle wafer was omitted because it was not required to provide electrical contact from a cathode to the vias. However, the consequence of not using a handle wafer is that the growth of electroless nickel is uninhibited at the probe tips and mushrooms outward, resulting in rounded probes tips that are wider than the diameter of the vias and protrude from the surface of the Pyrex substrate. While this structure is still appropriate for Langmuir probes as a sensorial skin, it is less optimal for blended body applications where the Debye length of the plasma is smaller than the diameter of the probes. In other words, because the probe tips are not flat, they would not be level with respect to the outer surface of a spacecraft and could perturb its plasma sheath.

The results of the 2-hour electroless nickel process are shown in Figure 4.12. This image confirms that electroplated gold is an adequate seed layer for electroless nickel, and that electroless nickel can produce a smooth surface, regardless of the roughness of the electroplated gold, such as the sample pictured in Figure 4.10. The deposition rate of the electroless nickel was found to be approximately 25 μm/hour. The results of this experiment suggest that electroless nickel is suitable to fill in the vias because of its larger deposition rate, conformality, and smoothness of the deposited material.

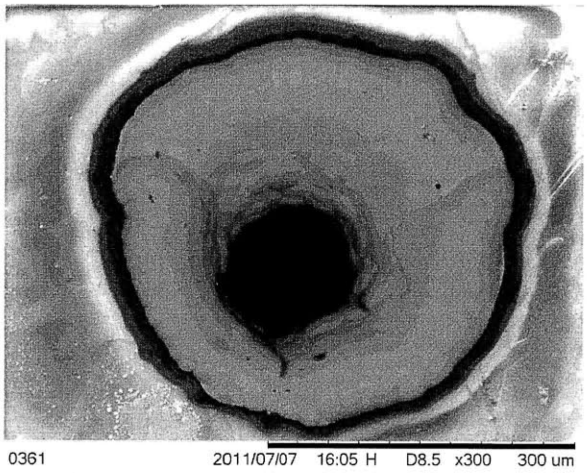

**Figure 4.12: SEM of a 200 μm-diameter metalized via as seen from the plasma side of the probe. The via was partially filled with electroplated gold from the fourth gold electroplating experiment, and then partially filled with electroless nickel deposition.**

## 4.3 Fabrication Process Flow of the MEMS Langmuir Probe Arrays

The multiplexed MEMS Langmuir probes developed in this thesis consist of an array of electroless nickel vias embedded into a flat Pyrex substrate. The fabrication process of these devices began with a 100-mm Pyrex wafer that had arrays of vias that were ultrasonically machined by a vendor (Bullen Ultrasonics, Eaton, OH) (Figure 4.13.A). Contact photolithography on an airbrushed photoresist film was then conducted to transfer die-saw lines onto the Pyrex wafer (Figure 4.13.B). The wafer was then die-sawed (Figure 4.13.C). After this, the dies were cleaned using a piranha bath (Figure 4.13.D). After cleaning, the vias were coated with a 0.05 μm Ti/0.25 μm Au sputtered film stack using the shadow mask shown in Figure 4.3; the coating was applied on the side of the substrate that will not be exposed to the plasma when in operation (Figure 4.13.E). Finally, the dies were immersed in an electroless nickel plating bath for 4 hours to fill in the vias and complete the devices (Figure 4.13.F).

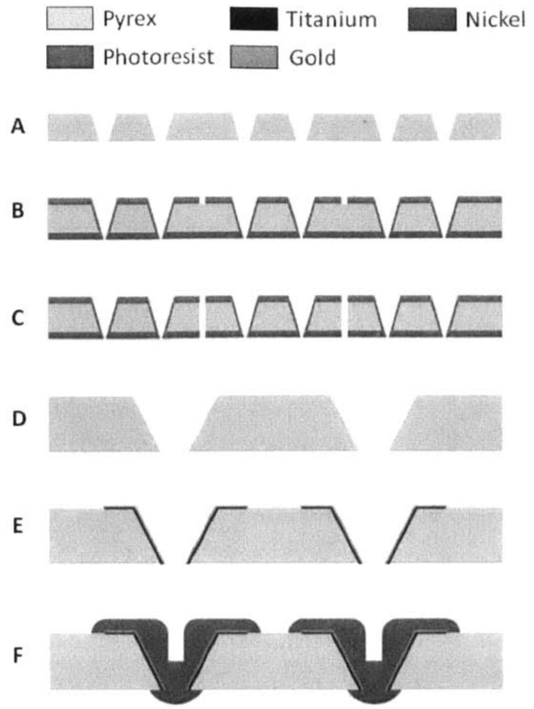

Figure 4.13: Process flow to fabricate arrays of MEMS Langmuir probes (A) Ultrasonic drilling of the Pyrex wafer; (B) Transfer of die-saw lines using contact lithography; (C) Die-sawing of Pyrex wafer; (D) Dies cleaned using a piranha bath; (E) Sputtered Ti/Au film stack is deposited into the vias using a shadow mask; (F) Electroless nickel plating of vias.

The completed devices are shown in Figure 4.14. Based on our electroplating experiments, it was determined that the holes visible in the figure do not go through the vias and that they are the result of the way the nickel deposited into the vias. An SEM of the plasma-facing side of an array with 100 μm-diameter vias at the plasma side is shown in Figure 4.15. While the original diameter of the plasma-facing side of the vias was 100 μm, the electroless nickel deposition increased the probe tip diameter to 600 μm. This structure was produced because a handle wafer was not utilized during the plating process to inhibit the growth of the electroless nickel at the probe tips. Figure 4.16 is an SEM of a broken die showing the device structure.

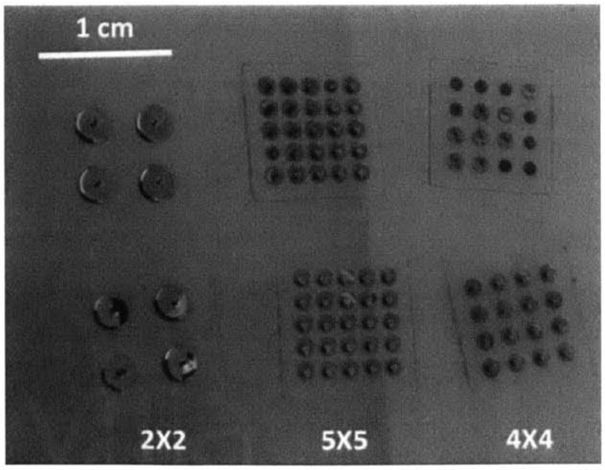

Figure 4.14: Various array sizes of MEMS Langmuir probes.

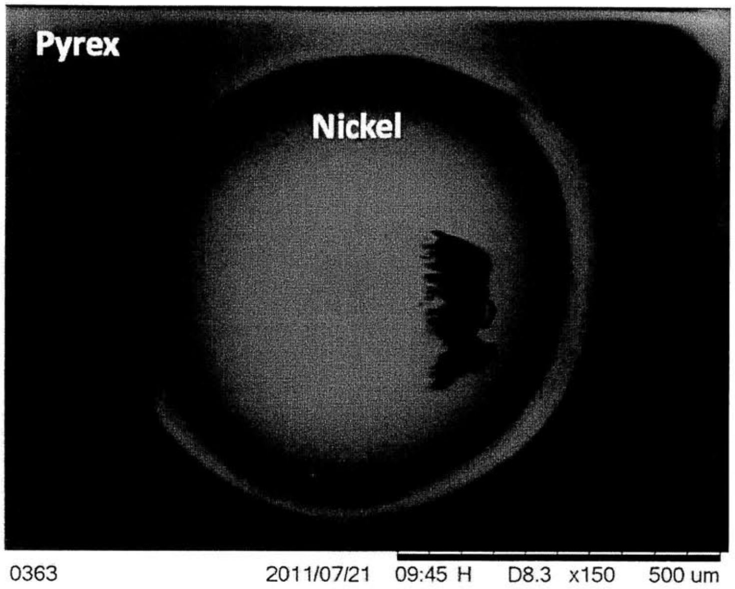
Pyrex
Nickel
0363
2011/07/21 09:45 H D8.3 x150 500 um

**Figure 4.15: SEM of the plasma side view of a 600-μm diameter MEMS Langmuir probe from a 2×2 array containing 100 μm-diameter vias. The smudge on the nickel probe is residue from graphite tape that was used for taking other SEMs.**

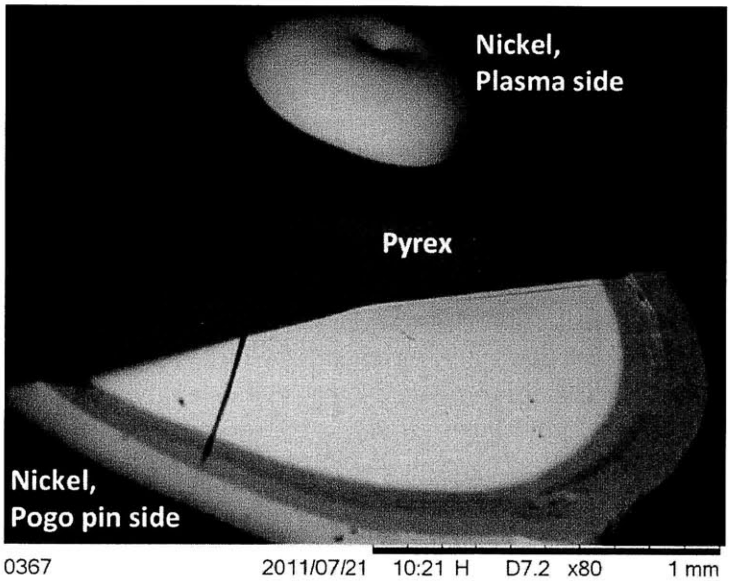
Nickel,
Plasma side
Pyrex
Nickel,
Pogo pin side
0367
2011/07/21 10:21 H D7.2 x80 1 mm

**Figure 4.16: Cross section view of a MEMS Langmuir probe part of a 2×2 probe array. The titanium adhesion layer remained attached to the electroless nickel on the pogo-pin side of the probe when the die was broken to create this cross section view. The titanium adhesion layer is the lighter colored inner circle on the pogo pin side.**

## 4.4 Chapter 4 Summary

This chapter documented the experimental investigations that led to the batch fabrication of multiplexed MEMS Langmuir probes consisting of arrays of electroless nickel vias in a Pyrex wafer. The experimental characterization of the MEMS Langmuir probes is documented in Chapter 5, including a description of the testing apparatus, driving electronics, testing procedure, and data analysis.

# 5 Experimental Characterization of Multiplexed MEMS Langmuir Probes

The MEMS Langmuir probes were preliminarily tested as triple Langmuir probes in plasma at MIT's Versatile Toroidal Facility (VTF). The performance of the MEMS probes was compared with the performance of a homemade macro-scaled triple Langmuir probe that was tested in VTF at the same time and under the same conditions. This chapter describes the experimental apparatus used in the characterization of the MEMS probes: macro probe, MEMS test fixture, and driving circuitry. In addition, the experimental procedure, data, and data analysis of the MEMS and macro Langmuir probes are also presented.

## 5.1 Experimental Apparatus

### 5.1.1 Macro Triple Langmuir Probe Design and Fabrication

A conventional triple Langmuir probe was constructed to benchmark the performance of the MEMS Langmuir probes. The conventional probe consists of three 0.61 mm-diameter tungsten wires with 1 cm free length and 1-mm probe-to-probe separation. The surface area of each tungsten probe is nearly 70 times larger than the surface area of a MEMS probe; this way, the macro-scaled probes would collect higher currents using the same driving circuitry, which should result in more accurate estimates of the plasma parameters than the estimates from the MEMS plasma probe data. The probe tips extend 64 cm from VTF's ceiling into the plasma environment; this depth is the location where the densest plasma can be accessed. A schematic of the macro probe is shown in Figure 5.1 and the fabricated triple Langmuir probe is shown in Figure 5.2, including a close-up of the probe tips.

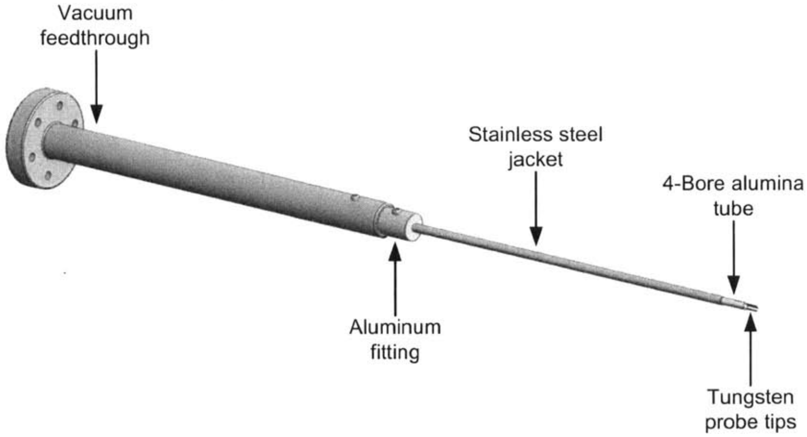

**Figure 5.17: The primary components of the conventional triple Langmuir probe.**

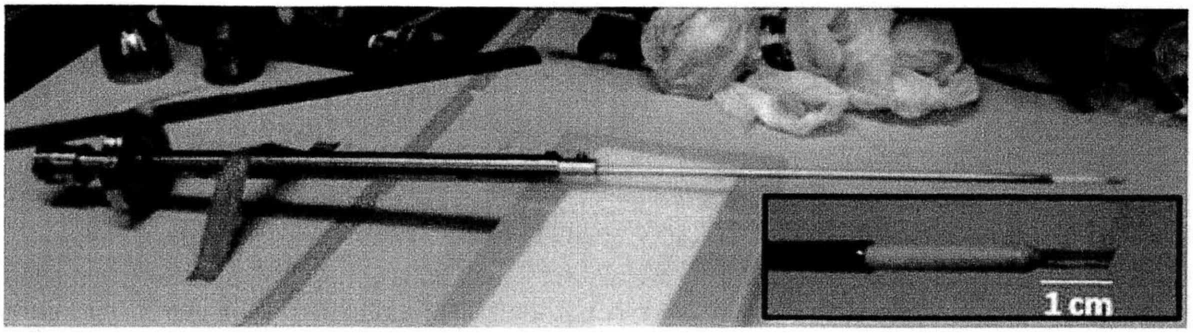

**Figure 5.18: Completed conventional triple Langmuir probe (top), and detail of the tungsten probe tips (bottom).**

The dimensions of the conventional and MEMS probes are presented in Table 5.1. The surface area of the conventional probe is approximately 70 times larger than the surface area of the MEMS probe, i.e., a macro probe tip collects about 70 times the current collected by each MEMS probe. Generally, larger currents can be measured more precisely and therefore, the conventional probe serves as a benchmark for the performance of the MEMS probes. We only tested a 2×2 MEMS Langmuir probe die.

**Table 5.1: Comparison of Conventional and MEMS Triple Probe Dimensions**

| | Diameter (mm) | Pitch (mm) | Surface Area (mm$^2$) |
|---|---|---|---|
| **Conventional Probe** | 0.61 | 1 | 19.46 |
| **MEMS Probe** | 0.60 | 4 | 0.28 |

### 5.1.2 MEMS Triple Langmuir Probe Test Fixture and VTF Installation

The MEMS triple Langmuir probe was installed in VTF approximately 60 degrees away from the conventional probe due to the arrangement of the available ports on VTF's ceiling. Similar to the conventional probe, the MEMS probe was extended to a depth of approximately 64 cm into the plasma chamber from the ceiling. The test fixture of the MEMS probe consists of a custom machined aluminum die holder and an extension rod, pictured in Figure 5.3; the fixture also provides an electrical connection to the probes via pogo pins. The die holder was fastened to the extension rod via a threaded connection and a vacuum feedthrough was attached to the extension rod so the MEMS probe can be tested at VTF.

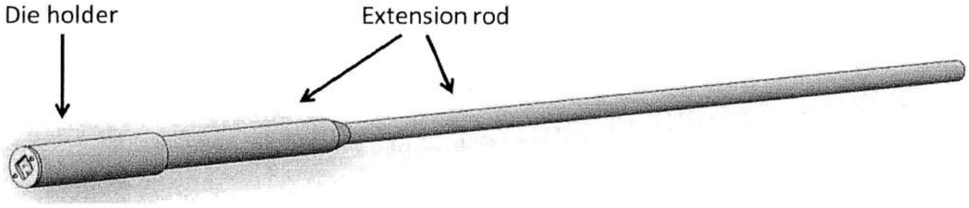

**Figure 5.19: The test fixture for the MEMS Langmuir probes.**

A diagram of the assembly of a die into the test fixture is shown in Figure 5.4. The die is secured in place inside the die holder between pogo pin electrical connectors and an aluminum faceplate. The pogo pins are press-fit into a custom machined Vespel fixture that provides electrical insulation between the pogo pins. The current Vespel fixture contains a 2×2 array of pogo pins, which is compatible with a 2×2 array of MEMS Langmuir probes. 28 AWG shielded twisted wires were soldered to the ends of the pogo pins not in contact with the die. Shielded twisted wires were chosen to help eliminate electrical interference. A photo of the die holder before the die was installed is shown in Figure 5.5.A, while Figure 5.5.B is a photo of the die installed in the die holder.

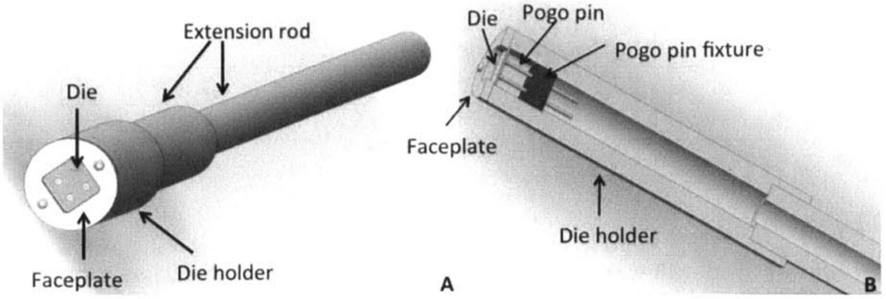

**Figure 5.20: (A) Schematic of the MEMS Langmuir probe test fixture; (B) Cross-section of the MEMS probe test fixture.**

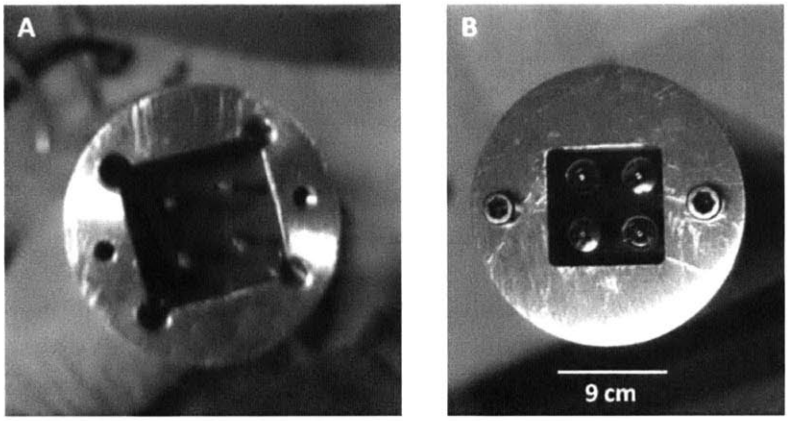

**Figure 5.21: (A) The brown vespel pogo pin fixture and gold pogo pins are shown within the die holder before the die was installed; (B) The MEMS die installed into the die holder and secured with the faceplate.**

### 5.1.3 VTF Plasma Parameters and Experimental Considerations

Knowledge about VTF's plasma parameters is required to benchmark the performance of the conventional and MEMS probes. Unfortunately, at the time of testing the probes VTF was under construction and the plasma diagnostics equipment had not yet been installed. Therefore, a literature search was conducted to determine the range of the electron temperatures and number densities that had been recorded in the past at VTF. The electron temperatures ranged from 2 – 15 eV and the number densities were on the order of $10^{17}$ – $10^{18}$ $m^{-3}$ [36,38,39,40,41]. The electron temperature is consistent throughout the plasma, while the density is highest in the center of the plasma chamber and lowest around the edges [39]. In the preliminary experimental characterization conducted in this thesis, the probes were installed such that the highest plasma densities could be accessed. It would have been more valuable to also test the probes in a variety of different plasma conditions to verify that the probes can perform properly at different operational points; this could have been easily done by varying the insertion distance of the probe, as a smaller insertion distance would access plasma of the same temperature but visibly less dense.

We estimated the current that our macro triple probe and MEMS probe would collect based on the single Langmuir probe data discussed in Chapter 2. The current collected by a Langmuir probe is proportional to surface area; hence the surface areas of the conventional and MEMS triple probes were compared to the surface area of the single Langmuir probe to estimate the current that the triple probes would collect. The criterion we used was the ion saturation current and the results of this exercise are presented in Table 5.2. These estimates indicate that the driving electronics must be capable of accurately measuring currents lower than $10^{-4}$ A. This discussion continues in more detail in Section 5.1.4, where the design and capabilities of the driving electronics are presented.

**Table 5.2: Estimation of Ion Saturation Current Collected by the Conventional and MEMS Triple Probes**

| | Surface Area ($mm^2$) | Ion Saturation Current (A) |
|---|---|---|
| **Single Probe** | 32.20 | $1.20\times10^{-2}$ |
| **Conventional Triple Probe** | 19.46 | $7.25\times10^{-3}$ |
| **MEMS Triple Probe** | 0.28 | $1.05\times10^{-4}$ |

### 5.1.4 Driving Electronics

The conventional and MEMS triple Langmuir probes were operated using the current-mode scheme (Chapter 2). In the literature, triple probe currents have been measured successfully with oscilloscope current probes, which do not draw current from the triple probe circuitry and hence do not hinder the operation of the probes [55]. Unfortunately, the current probes are not able to measure the small currents that we anticipate the MEMS probes will generate. Therefore, we developed suitable driving circuitry to collect the data. This section describes the driving circuitry and the testing that was performed to ensure that the circuit could measure current in the $10^{-4} - 10^{-2}$ A range.

#### *5.1.4.1 Circuit Description*

The driving circuit, shown in Figure 5.6, accomplishes two primary objectives. First, it supplies bias voltages between the probes using batteries that are floating; second, the driving circuitry provides voltage measurements across resistors $R_4$ and $R_5$, and across $R_9$ and $R_{10}$, which can be converted into measurements of the probe currents $I_2$ and $I_3$ using the following expressions:

$$I_2 = \frac{V_1}{\left(\frac{1}{R_4}+\frac{1}{R_D}\right)^{-1}} + \frac{\left[\frac{V_1\left[R_2+\left(\frac{1}{R_4}+\frac{1}{R_D}\right)^{-1}\right]}{\left(\frac{1}{R_4}+\frac{1}{R_D}\right)^{-1}} - \frac{V_2\left[R_3+\left(\frac{1}{R_5}+\frac{1}{R_D}\right)^{-1}\right]}{\left(\frac{1}{R_5}+\frac{1}{R_D}\right)^{-1}}\right]}{R_1} \tag{5.1}$$

$$I_3 = \frac{V_4}{\left(\frac{1}{R_{10}}+\frac{1}{R_D}\right)^{-1}} + \frac{\left[\frac{V_4\left[R_8+\left(\frac{1}{R_{10}}+\frac{1}{R_D}\right)^{-1}\right]}{\left(\frac{1}{R_{10}}+\frac{1}{R_D}\right)^{-1}} - \frac{V_3\left[R_7+\left(\frac{1}{R_9}+\frac{1}{R_D}\right)^{-1}\right]}{\left(\frac{1}{R_9}+\frac{1}{R_D}\right)^{-1}}\right]}{R_6} \tag{5.2}$$

The circuit supplied 9 V and 18 V between the probes. In Chapter 2, it was mentioned that the bias voltages should be around 2 V and 10 V to obtain accurate measurements of the electron temperature, according to Chen and Sekiguchi [33]. However, a more general rule of thumb is that the higher bias voltage should be larger than the electron temperature to ensure that the electrons saturate [55]; also, the two bias voltages should not be equal to each other in order to avoid error in the measurement of the electron temperature [33]. Since the electron temperatures of VTF's plasmas were reported in the range of 2 – 15 eV, we selected 18 V as the higher bias voltage instead of 10 V, which was supplied by two 9 V-batteries in series. For the lower bias voltage, we intended to supply 3 V, but an error in the setup resulted in a 9 V bias instead. This will clearly affect the accuracy of the probe estimates as a wrong choice of bias voltages in a triple Langmuir probe can cause 50% or more of difference between its estimates of the plasma parameters and the estimates from single Langmuir probe data [33]. Therefore, the experiments reported in this thesis should be seen as a preliminary characterization of the devices and a proof-of-concept of the testing rig, instead of the validation of a microfabricated instrument. In future work, the bias voltages should be optimized by comparing the estimated plasma parameters with the estimates from single Langmuir probe data using 2 V and 30 V as staring guesses of the bias voltages.

The four voltage dividers, i.e., $R_2$ and $R_4$, $R_3$ and $R_5$, $R_7$ and $R_9$, and $R_8$ and $R_{10}$, were introduced to ensure the 2 MHz voltage digitizers (GE ICS645B) measuring $V_1$, $V_2$, $V_3$, and $V_4$ would not see more than 1 V peak-to-peak. The values of the resistors in the voltage dividers are $R_2=R_3=10$ kΩ, $R_7=R_8=100$ kΩ, and $R_4=R_5=R_9=R_{10}=1$ kΩ. The resistors labeled $R_D$ correspond to the impedance (500 Ω) of the voltage digitizers. The resistors $R_1$ and $R_6$ were changed from 100, 1k, 10k, 100k, to 1M Ω, depending on what values provided the most optimal measurements of $I_2$ and $I_3$.

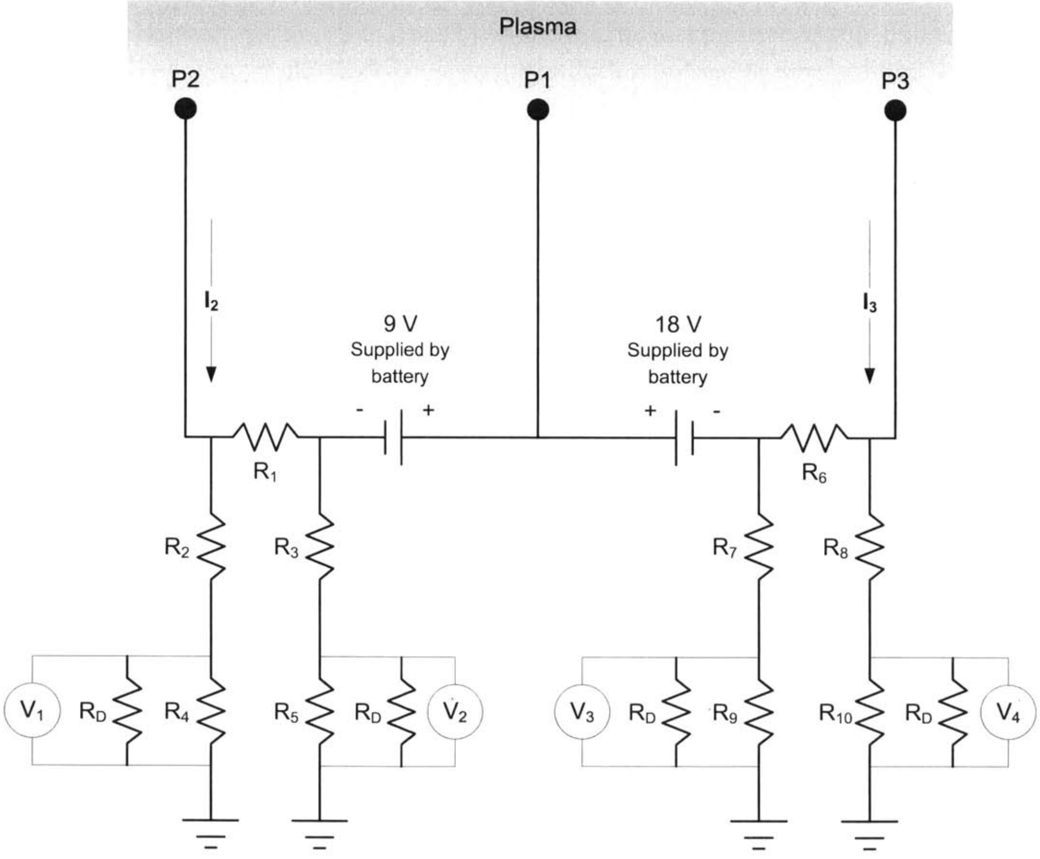

**Figure 5.22: Schematic of the circuit used to drive the conventional and MEMS triple Langmuir probes at VTF.**

### 5.1.4.2 *Circuit Characterization*

We tested the driving circuit without plasma to determine if it was working as expected, and also to select values for $R_1$ and $R_6$ that would provide the best measurements of $I_2$ and $I_3$. The performance of the circuit could be affected by non-idealities such as parasitic resistance due to the long wires between the circuit and voltage digitizers, errors in resistor values, and contact resistance. The circuit was tested by supplying a known current $I_2$ and by measuring $V_1$ and $V_2$. The same test was repeated for $I_3$, whereby $V_3$ and $V_4$ were measured. A source-measure unit (SMU, Keithley 237) supplied the current $I_2$ or $I_3$, and another two SMUs measured $V_1$ and $V_2$, or $V_3$ and $V_4$. The SMUs were operated by our own LabVIEW script to automatically supply the currents and measure the voltages. The currents $I_2$ and $I_3$ ranged from $10^{-7}$ to $10^{-2}$ A. $R_1$ and $R_6$ were changed from 100, 1k, 10k, 100k and 1 MΩ. The SMUs were set to acquire 32 voltage measurements total for each current and resistor combination tested; these measurements were then averaged to obtain 1 final measurement for each combination. The measured voltages $V_1$, $V_2$, $V_3$, and $V_4$ and the corresponding resistor values $R_1$ and $R_6$ were substituted into equations 5.1 and 5.2 to back-calculate the applied currents $I_2$ and $I_3$. A ratio of the applied current to the estimated current was introduced to compare how accurately the applied currents $I_2$ and $I_3$ were calculated using the measurements of $V_1$, $V_2$, $V_3$, and $V_4$. In 32 out of the 60 measurements, equations 5.1 and 5.2 provided an accurate estimate of $I_2$ and $I_3$, where the ratio of applied current to estimated current was within the range of 0.9 – 1.1 (i.e., the range where the estimated current is equal to within ±10% of the of the actual current). This indicates that losses due to contact resistance or long wires do not have a significant impact on the $I_2$ and $I_3$ measurements under certain conditions. A summary of these experiments is shown in Table 5.3.

**Table 5.3: Applied current-to-measured current ratio for $I_2$ and $I_3$. Combinations where the measured current is within 10% of the applied current are shown in black.**

| | **Applied Current $I_2$ (A)** | | | | | |
|---|---|---|---|---|---|---|
| **Resistor $R_1$ (Ω)** | **$10^{-7}$** | **$10^{-6}$** | **$10^{-5}$** | **$10^{-4}$** | **$10^{-3}$** | **$10^{-2}$** |
| **100** | -0.00907 | -0.119 | -17.2 | **1.06** | **0.968** | **0.964** |
| **1k** | -0.0885 | -2.94 | 1.14 | **1.01** | **1.00** | **1.00** |
| **10k** | -1.15 | 1.25 | **1.02** | **1.01** | **1.00** | **1.00** |
| **100k** | 5.29 | **1.10** | **1.01** | **1.01** | **1.00** | **1.00** |
| **1M** | 10 | **1.09** | **1.01** | **1.01** | **1.00** | **1.00** |
| | **Applied Current $I_3$ (A)** | | | | | |
| **Resistor $R_6$ (Ω)** | **$10^{-7}$** | **$10^{-6}$** | **$10^{-5}$** | **$10^{-4}$** | **$10^{-3}$** | **$10^{-2}$** |
| **100** | -0.00099 | -0.00904 | -0.104 | 0.829 | 0.439 | -0.305 |
| **1k** | -0.00898 | -0.0935 | -0.833 | **0.974** | 0.887 | 1.76 |
| **10k** | -0.0805 | -3.89 | 1.14 | **0.99** | **0.989** | **1.05** |
| **100k** | -1.41 | 1.22 | **1.02** | **1.00** | **1.00** | **1.01** |
| **1M** | 1.68 | 1.11 | **1.01** | **1.00** | **1.00** | **1.00** |

The estimated current collected by the MEMS probe is on the order of $10^{-4}$ A, which means that currents as small as $10^{-5}$ A need to be resolved. Moreover, the estimated current collected by the conventional probe is on the order of $10^{-2}$ A, which means that currents as small as $10^{-3}$ A need to be resolved. Nonetheless, since we did not actually know whether the estimated currents were accurate, we selected appropriate values for the resistors $R_1$ and $R_6$ based on the larger range of $10^{-7}$ to $10^{-2}$ A. However, the results in Table 5.3 indicate that none of the resistors can provide accurate measurements of currents as small as $10^{-7}$ A, and only $R_1$=100k or 1M Ω can accurately measure down to $10^{-6}$ A. As the currents increase, more resistor options are available. In general, the characterization of the driving circuitry shows that each resistor $R_1$ and $R_6$ has associated with it a valid range of currents that can be accurately measured, and this is considered in the analysis of the data collected from the probes during the VTF experiments.

The sensitivity of the voltage digitizers is also considered. From our driving circuit characterization experiments, the SMU's indicated that the measured voltages corresponding to $10^{-7}$ A were on the order of $10^{-5}$ V. The voltage digitizers can take measurements as low as $3 \times 10^{-5}$ V, which is not adequate for measuring probe currents on the order of $10^{-7}$ A for any resistor $R_1$ or $R_6$. However, this is not necessarily a hindrance because the driving circuitry itself is not accurate in the range of $10^{-7}$ A for any resistor $R_1$ or $R_6$. At best, the voltage digitizers can measure voltages corresponding to probe currents on the order of $10^{-6}$ A for any resistor $R_1$ or $R_6$, which is compatible with the range of accuracy of the driving circuitry.

An additional consideration is the thermal electron voltage (about 26 mV), which is a potential source of noise [56]. According to our experiments, the voltage measurements $V_1$, $V_2$, $V_3$, and $V_4$ are the same order of magnitude as the thermal electron voltage when $I_2$ and $I_3$ are on the order of $10^{-4}$ A or less, for any resistor value. This suggests that the MEMS probe data captured using this circuit do not have good signal-to-noise ratio, and corroborates our claim that the data should be seen as a preliminary characterization. Future work should include modifying the circuit to increase the range and accuracy of the measurements; this can be readily be done by using operational amplifiers.

## 5.2 Experimental Setup and Procedure

After the probes were installed at VTF, they were connected to the driving circuitry, and the driving circuitry was connected to the voltage digitizers using twisted pairs of 28 AWG wires to reduce interference. The driving circuitry for each probe was arranged on a breadboard; the breadboards were positioned within 20 cm of their respective probe. The driving circuitry for the two probes was setup identically, and the resistors $R_1$ and $R_6$ were setup such that $R_1$=$R_6$; this way, the data from both probes could be directly compared to each other. Also, to ensure the measurements collected by the driving circuitry were repeatable, five plasma shots were measured for each value of $R_1$=$R_6$. The values of $R_1$=$R_6$ that were utilized during the plasma tests included the values presented in Table 5.3: 100, 1k, 10k, 100k, and 1M $\Omega$. Therefore, with five different values of $R_1$=$R_6$, and 5 shots for each value, 25 total shots were taken in plasma. A LabVIEW interface developed by former students at VTF collected data from the voltage digitizer channels that were utilized to measure $V_1$, $V_2$, $V_3$, and $V_4$ for each probe. Data was collected only during the plasma shot and a brief period before and after. The plasma shots were approximately 3 ms long, and data was acquired in a window that began 6 ms before the shot to 7 ms after the shot, providing a total of 16 ms of data per shot. The single Langmuir probe characterization reported in Chapter 2 was tested using 20 ms plasma shots, rather than the 3 ms plasma shots that were used in these experiments. Although 20 ms plasma shots would have been more stable and provide better data, this setup was not available at VTF at the time that the MEMS probe was tested.

In order to identify the interference of various devices turning on and off, and to corroborate when the actual plasma events began, measurements were also acquired from the probes without plasma. It was determined that the period of time when there is minimal interference from external devices occurs from 6.25 – 9.0 ms during the plasma shot (i.e., during the time the plasma was on). The voltage digitizers collect data at a rate of 2 MHz, i.e., 5500 data points were collected during each plasma event. In future work, the driving circuitry should be placed inside a metal box (Faraday cage) to shield it from background noise.

## 5.3 Data Analysis

### 5.3.1 Data Analysis Procedure

The data analysis procedure accomplishes two key functions. First, it determines whether the collected data is accurate by checking whether the measured currents $I_2$ and $I_3$ fall within the range of accuracy for the corresponding resistor $R_1$ and $R_6$ in the driving circuit. Second, the procedure implements current-mode theory, as described in Chapter 2, to estimate the electron temperature $T_e$, number density $n_e$, and Debye length $\lambda_D$ from the MEMS probe and conventional probe data. These estimates were compared with the expected range of values at VTF. The data analysis procedure was carried out in Matlab, and it includes the following general steps:

1) Load raw VTF data files into Matlab.
2) Select the data corresponding to the 6.25 – 9.0 ms interval.
3) Calculate the probe currents $I_1$, $I_2$, and $I_3$ from the voltage data $V_1$, $V_2$, $V_3$, and $V_4$ using equations 5.1 and 5.2. Each time interval contains multiple data sets, each data set has a different estimated current set.
4) Determine whether the magnitude of $I_2$ and $I_3$ fall within the range of accuracy of the corresponding resistors $R_1$ and $R_6$, and check whether $I_2<I_3$.
5) Calculate $T_e$ and $n_e$ using equations 2.12 and 2.13. The solution for $T_e$ utilizes a Newton-Raphson algorithm to numerically solve the nonlinear equation 2.12. The algorithm used 0.3 eV as an initial guess for $T_e$ and the error tolerance was $10^{-5}$, which provided the best conditions for convergence. Each time interval contains multiple data sets, each data set has a different estimated $T_e$ and $n_e$.
6) Calculate $\lambda_D$ using equation 2.2. Each time interval contains multiple data sets, each data set has a different estimated $\lambda_D$.
7) Calculate the mean and standard deviations of $T_e$, $n_e$, and $\lambda_D$ over the course of all plasma shots corresponding to a particular value of $R_1$ and $R_6$, and compare the averaged data to the expected range of VTF plasma parameters.

### 5.3.2 Results

The raw voltage data for the conventional probe and the MEMS probe is shown in Figure 5.7 and Figure 5.8, respectively. Each plot shows the voltage data of all five shots for a particular value of $R_1=R_6$. The large peaks in the data indicate interference due to devices at VTF turning on and off. The interval from 6.25 – 9.0 ms that contains the plasma shot data was corroborated using the plots on the bottom right of Figures 5.7 and 5.8, where data was collected without plasma. The data were used to calculate the probe currents, shown in Figure 5.9 for the conventional probe and in Figure 5.10 for the MEMS probe.

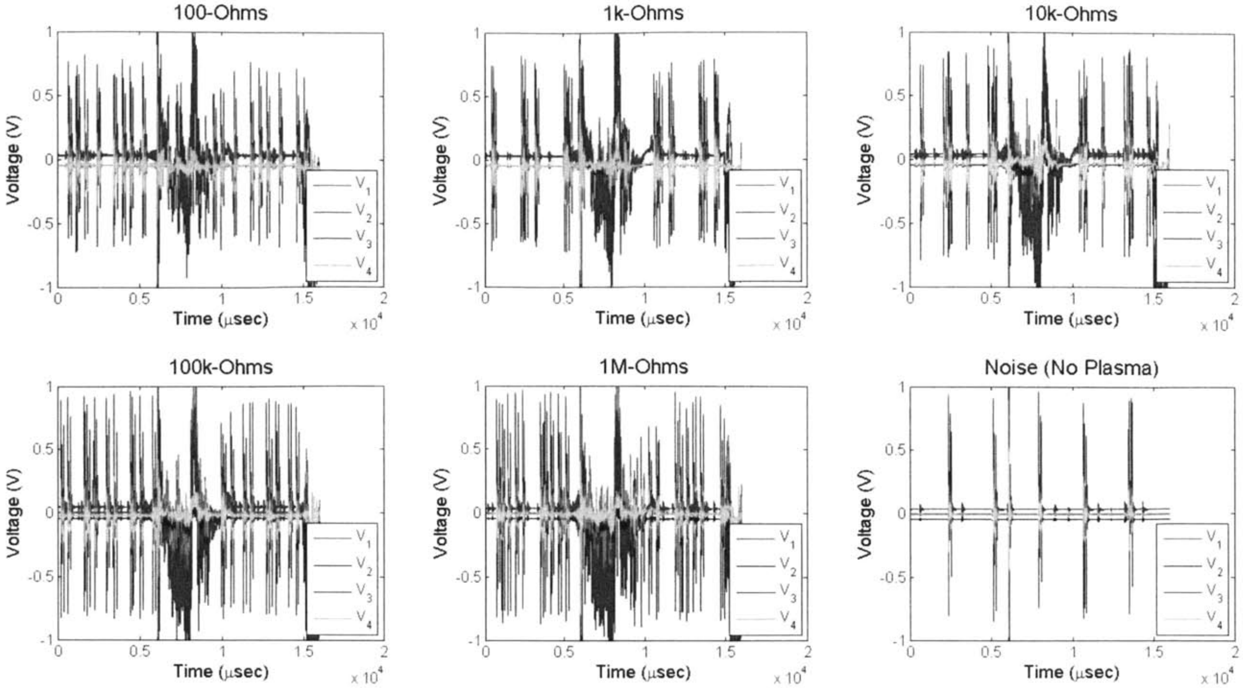

**Figure 5.23: Conventional triple probe raw voltage data corresponding to each value of $R_1$=$R_6$ in the driving circuitry.**

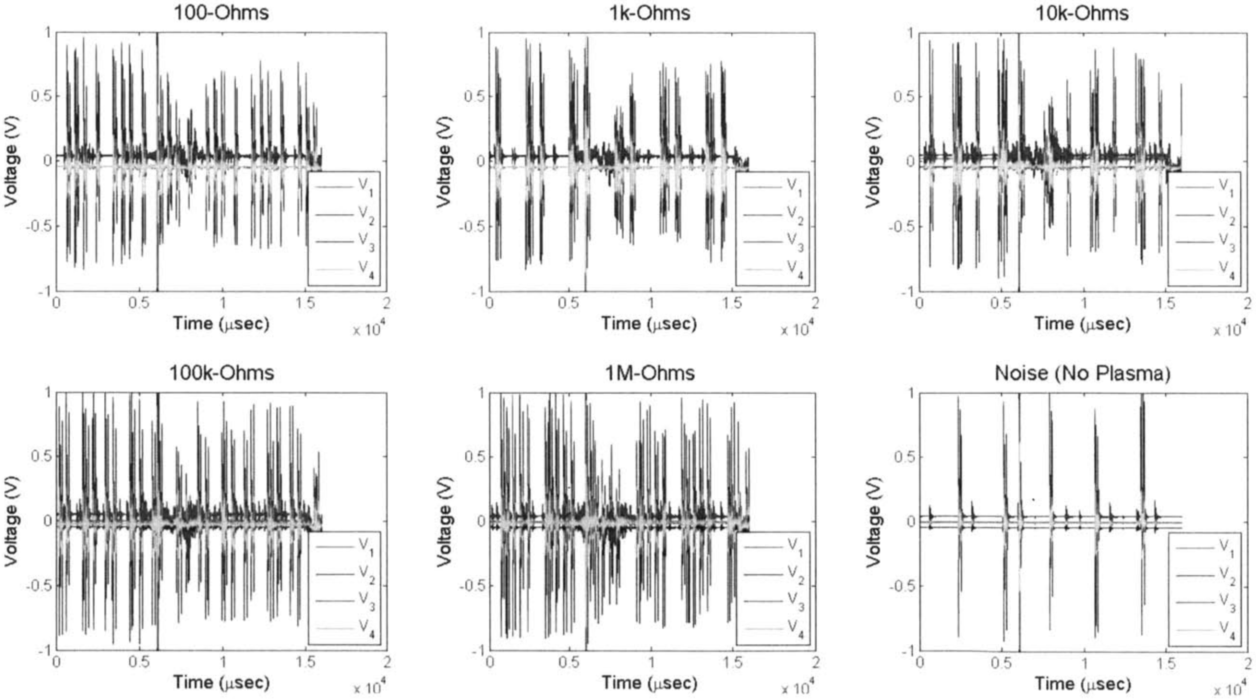

**Figure 5.24: MEMS probe raw voltage data corresponding to each value of $R_1$=$R_6$ in the driving circuitry. Each plot contains data from 5 plasma shots, except for the noise plot on the lower right, which contains 1 shot.**

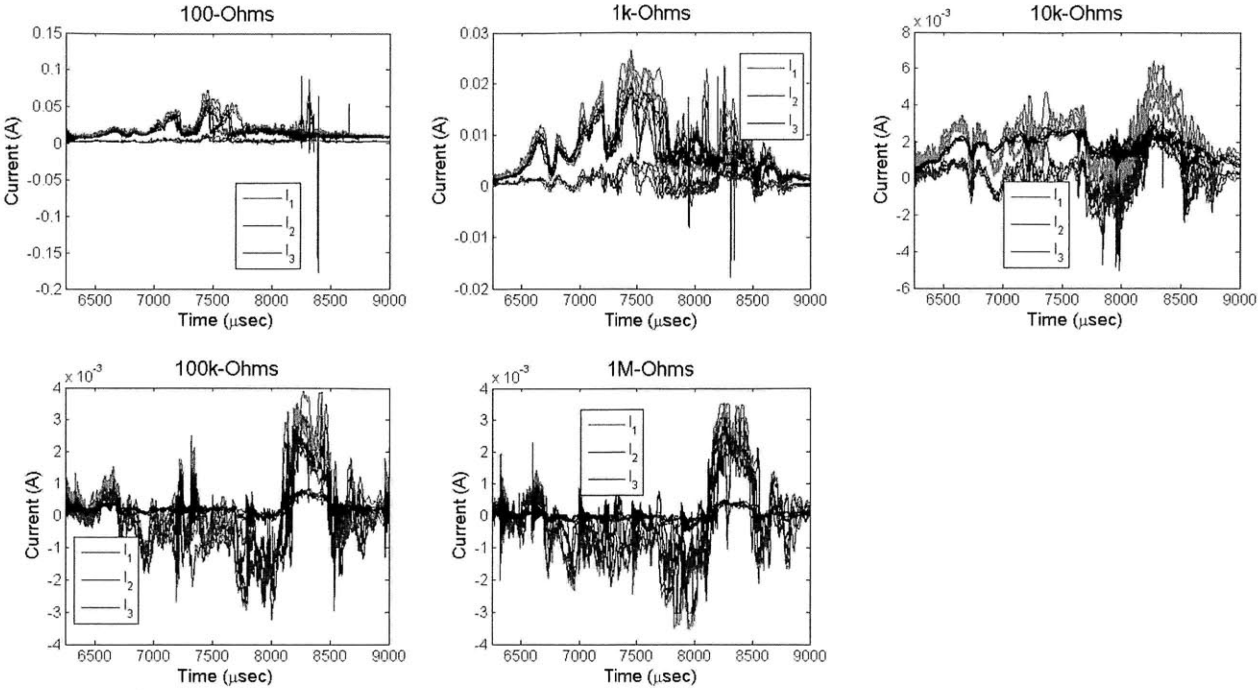

**Figure 5.25: Conventional probe currents $I_1$, $I_2$, and $I_3$, corresponding to each value of $R_1$=$R_6$ in the driving circuitry. Each plot contains data from 5 plasma shots.**

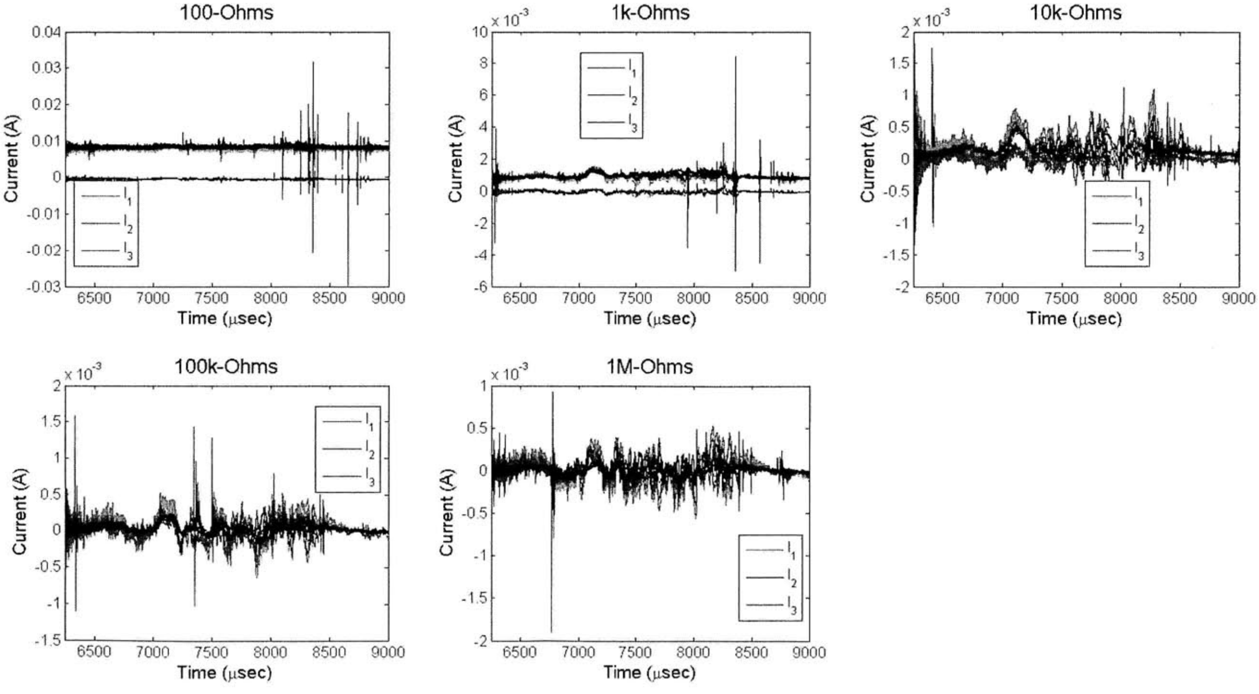

**Figure 5.26: MEMS probe currents $I_1$, $I_2$, and $I_3$, corresponding to each value of $R_1$=$R_6$ in the driving circuitry. Each plot contains data from 5 plasma shots.**

The estimated probe currents are within the range of accuracy of the driving circuitry, except for the measurements of $I_3$ that were taken using $R_1$=$R_6$=100 and 1k Ω for both the conventional and MEMS probes. Given our knowledge about the behavior of the driving circuitry in Table 5.3, we can conclude that the measurements of $I_3$ are overestimated when $R_6$=100 or 1k Ω by as much as an order of magnitude. The plots where $R_1$ and $R_6$ are 100, 1k, and 10k Ω show that the magnitude of $I_2$ is less than the magnitude of $I_3$, which indicates that the probes and driving circuitry are setup properly [33]. However, in the plots where $R_1$ and $R_6$ are 100k and 1M Ω, there is a lot of fluctuation and it is generally the case that $I_2<I_3$ does not hold. While high variation in the data is expected due to VTF's plasma instabilities, the fact that $I_2<I_3$ does not hold when $R_1$ and $R_6$ are 100k or 1M Ω is an indication of interference that is not related to fluctuating plasma parameters and that the data from these resistors is flawed for both the conventional and MEMS probes. The interference occurring at higher resistance values is likely caused by thermal (Johnson) noise, which is proportional to the magnitude of the resistance.

In the case of the MEMS probe where $R_1$=$R_6$=100 and 1k Ω, the data appears relatively flat and the instability of the plasma is not apparent. This is because the measurements are nearly equal to the thermal electron voltage, which is about 26 mV at 300 K [56]. This means that thermal voltage noise dominates the measurements of $I_2$ and $I_3$, which is why the data appear relatively flat in these cases. This also indicates that the measurements of $I_2$ and $I_3$ under these conditions are flawed.

To summarize, the measurements taken with $R_1$=$R_6$=100k and 1M Ω are flawed due to thermal noise for both the conventional and MEMS probes; the MEMS probe measurements taken when $R_1$=$R_6$=100 and 1k Ω are flawed as well because the thermal voltage is of the same order of the measurements; in addition, the data taken with $R_1$=$R_6$=100 and 1k Ω cannot be used to estimate $I_3$ in both the MEMS and the conventional probes because the circuit cannot accurately measure such currents. Therefore, the only combination left to analyze for both probes is $R_1$=$R_6$=10k Ω.

The mean and standard deviation of the electron temperature, number density, and electron Debye length were calculated across all five shots for $R_1$=$R_6$=10k Ω in the driving circuitry. The electron temperature corresponding to the conventional probe data and the MEMS probe data are shown in Figure 5.11. The number density and Debye length data are shown in Figures 5.12 and 5.13, respectively.

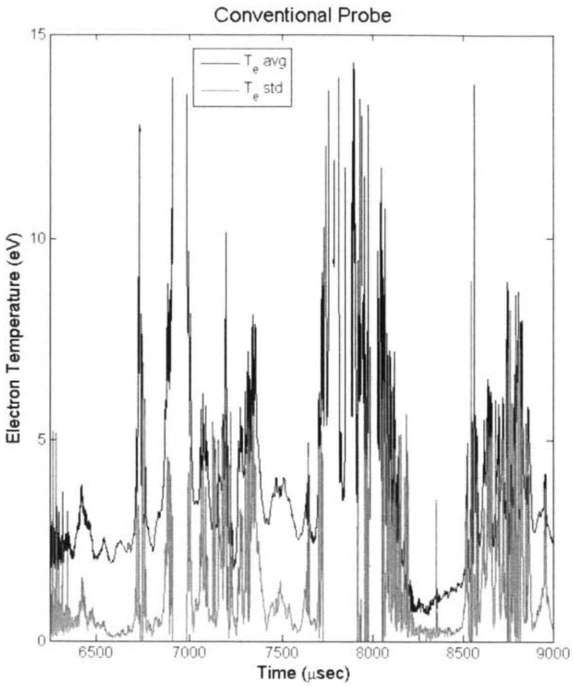

**Figure 5.27:** **The average and standard deviation of the electron temperature of five plasma shots from the conventional probe and MEMS probe data, corresponding to $R_1$=$R_6$=10k Ω in the driving circuitry.**

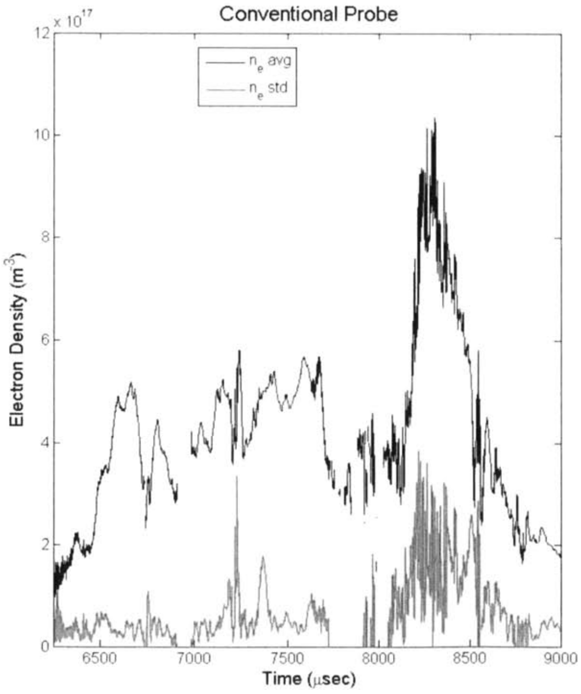

**Figure 5.28:** **The average and standard deviation of the electron temperature of five plasma shots from the conventional probe and MEMS probe data, corresponding to $R_1$=$R_6$=10k Ω in the driving circuitry.**

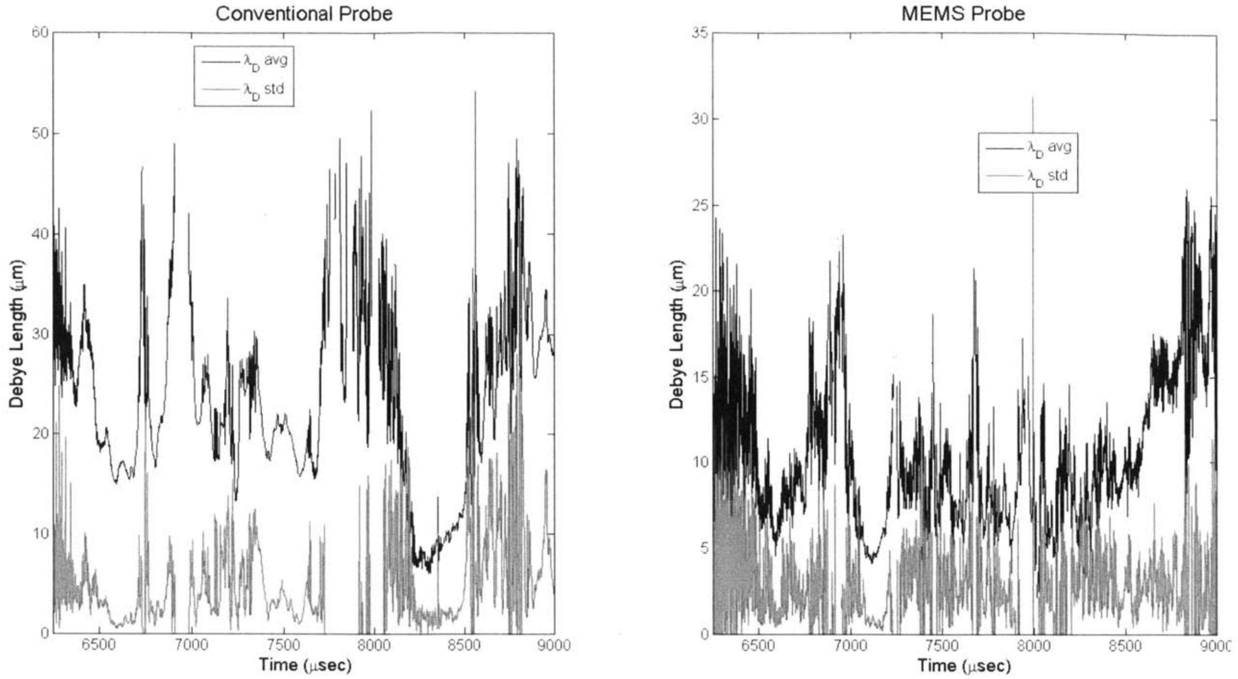

**Figure 5.29: The average and standard deviation of the electron Debye length of five plasma shots from the conventional probe and MEMS probe data, corresponding to $R_1$=$R_6$=10k Ω in the driving circuitry.**

## 5.4 Discussion

A side-by-side comparison of the plasma parameters extracted from the conventional and MEMS probe data is presented in Table 5.4. In this table, the plasma parameters have been averaged across the period of all five plasma shots corresponding to $R_1$=$R_6$=10k Ω, and the standard deviations are included in parenthesis as error bounds. Table 5.4 also includes the reported range of VTF's plasma parameters for comparing to the experimental data.

**Table 5.4: Average Plasma Parameters from 10k Ω Data**

| | Conventional Probe Data | MEMS Probe Data | VTF Reported Data |
|---|---|---|---|
| $T_e$ (eV) | 3.45 (±1.89) | 4.31 (±2.06) | 2 – 15 |
| $n_e$ ($m^{-3}$) | $4.14\times10^{17}$ ($\pm1.70\times10^{17}$) | $2.94\times10^{18}$ ($\pm1.56\times10^{18}$) | $10^{17} - 10^{19}$ |
| $\lambda_D$ (μm) | 22.69 (±8.13) | 10.08 (±4.06) | 3.32 – 91.03* |

***Based on the minimum to maximum $\lambda_D$ calculated using equation 2.2 for $T_e$ = 2 – 15 eV and $n_e \approx 10^{17} - 10^{19}$ $m^{-3}$**

Because the conventional probe serves as a benchmark for the MEMS probe, we first compared whether the conventional probe data falls within the range of VTF's reported plasma parameters. Then, we compared the performance of the MEMS probe to the conventional probe because they were operated under the same conditions and therefore, they should estimate similar plasma parameters.

The results in Table 5.4 indicate that the average electron temperature, density and Debye length from the conventional probe data fall within the range of VTF's reported plasma parameters. Further comparison cannot be made because the VTF did not have plasma diagnostics in operation.

The estimates of the plasma parameters from the MEMS probe should be similar to estimates of the plasma parameters from the conventional probe because they sensed the same plasma. Therefore, any MEMS probe data in Table 5.4, including the error bounds, that does not at least partially overlap the conventional probe data is considered flawed. From this exercise we found that the MEMS probe data falls completely within the range of VTF's plasma parameters, but only the electron temperature data overlaps the conventional probe's data. Therefore, the electron density and Debye length estimates from the MEMS probe are flawed or are related to different plasma conditions. There are two tentative explanations for this result. First, the plasma in VTF is isothermal and shows strong density variations; it is possible that the MEMS probe was sampling a visibly denser region that is at the same temperature. Second, the mismatch between the MEMS and conventional probe measurements could be the result of the smaller SNR on the MEMS probe data. Because the driving circuits utilized for both probes were the same, we can assume that both circuits were susceptible to the same amount of noise. However, because the currents from the MEMS probe are visibly smaller than the currents from the conventional probe, the MEMS probe data has a lower SNR and therefore, the MEMS probe is prone to overestimate the plasma parameters. This is apparent in how the MEMS probe predicts higher electron temperatures and densities compared to the conventional probe, which leads to a lower Debye length.

The circuit we have used in the characterization of the probes is more appropriate for collecting data from the conventional probe. The SNR of the circuit must be improved to acquire measurements from the MEMS probe that better agree with the conventional probe measurements. The SNR can be increased by including filters and operational amplifiers in the driving circuitry. In addition, more data should be taken in other plasma conditions to verify that the improved setup and tuning of the driving circuitry is sound. Because the plasma parameters at VTF cannot be varied at this time, a simple way to measure different plasma parameters would involve shortening the probes' extension rods and/or installing the probes in different areas to provide access to plasma regions with different plasma parameters. In addition, the lower bias voltage in the driving circuitry should be changed from 9 V to 2 V, and the higher bias voltage should be changed from 18 V to 30 V to collect better data. Moreover, the electronics should be placed inside a metal box (Faraday cage) to avoid interference from background noise. Additionally, single-probe measurements using the MEMS probes must be conducted to benchmark the performance of the triple probe setup and optimize the circuitry to obtain real-time accurate estimates of the plasma parameters.

## 5.5 Chapter 5 summary

A MEMS triple Langmuir probe was tested in plasma at VTF. The performance of the MEMS probe was benchmarked by a conventional triple Langmuir probe that was tested in VTF at the same time and under the same conditions. The test results preliminarily suggest that the conventional probe could acquire good-quality data using a particular setup of the driving circuitry; the MEMS probe could acquire good-quality data if the SNR of the circuitry is improved. More experiments are needed to confirm these results, which should include setting the right bias voltages and varying the plasma parameters to verify that the MEMS probe we developed is a valid scientific instrument. This can easily be done by measuring different regions of VTF's plasma (i.e., shortening the extension of the package into the plasma, and/or installing the devices in different locations).

# 6 Summary, Conclusions, and Recommendations for Future Work

In this thesis a planar array of batch-microfabricated MEMS Langmuir probes was designed, fabricated, and preliminarily characterized in plasma. The technology is intended to be used in applications such as reentry plasma diagnostics and nanosatellite scientific payloads.

## 6.1 Summary of MEMS Langmuir Probe Fabrication and Experimental Setup

A rough analysis of reentry heat transfer and plasma data, in addition to our microfabrication capabilities, led to the selection of a MEMS Langmuir probe design and a batch-microfabrication process. The batch-microfabrication process aligns with the new paradigm in space missions where hardware is miniaturized, high-performance, and mainstream affordable. The MEMS Langmuir probes were constructed by filling-in with electroless nickel 100 μm-diameter tapered vias machined into a Pyrex substrate, resulting in individually addressable probes having 600 μm-diameter tips. The filled-in vias were arranged in planar arrays on the Pyrex substrate, forming sensor tiles that could envelop the outer surface of a reentry vehicle and also be used as plasma sensor in a nanosatellite. The highest density arrays that were fabricated consist of 25 probes per 1 cm-square tile, having 1.6 mm separation between probes with square packing. Up to 45 probes per 1 cm-square tile can be achieved with this design if the probes are arranged in a hexagonal packing.

## 6.2 Summary of Experimental Setup, Procedure, Data Analysis, and Results

A test fixture was created to install the MEMS probes in VTF's plasma chamber. The MEMS Langmuir probes were operated in the triple probe configuration to acquire real-time measurements of the plasma parameters at VTF. In addition, a conventional triple probe was developed and tested at the same time and with the same driving circuitry as the MEMS probe to benchmark its performance. We developed and characterized a homemade circuit to operate the probes, while the real-time data was collected using 2 MHz voltage digitizers.

The data from the MEMS and the conventional probes were analyzed according to the current-mode triple Langmuir probe theory. Analysis of the data revealed that most of the data were flawed. The electron temperature, number density, and Debye length were estimated from the useful data, preliminarily confirming that the MEMS probes are capable of acquiring real-time data within the range of VTF's reported plasma parameters. However, the measurements acquired by the MEMS probe did not align with the electron density and Debye length data acquired by the conventional probe and therefore, more work is needed to validate the MEMS Langmuir probe technology.

## 6.3 Conclusions and Recommendations for Future Work

The ability of the MEMS Langmuir probes to acquire real-time measurements of VTF's plasma parameters justifies further consideration of low-cost, miniaturized plasma sensors for reentry plasma diagnostics and nanosatellite scientific payloads. The technology will become viable for these particular applications through improvements of the probe design and driving circuitry. In this section, several modifications are recommended to be conducted in future work.

In order for the Pyrex probes to survive the reentry plasma environment, cooling must be provided. However, the MEMS probes can also be constructed from materials that are more resilient compared to the Pyrex. The batch-microfabrication process of the MEMS probes reported in this thesis can accommodate many different materials. For example, in high-temperature applications, silicon carbide, alumina, or silicon nitride substrates could be interchanged with Pyrex. A better thermal analysis will help identify the best geometry and material selections for the harsh reentry conditions.

Environmental testing would be necessary to verify the results of the thermal analysis and determine the ability of the probes to withstand ablation and sputtering.

The diameter of the probe tips can be further decreased. In this thesis, we intended to fabricate probes as small as 100 μm-diameter, but a flaw in the samples used with the electroless nickel process resulted in 600 μm-diameter probe tips (there was no barrier to stop the deposition of nickel on the probe tips while the vias were filling in). Probe tips smaller than 600 μm-diameter can be achieved using a variation of the batch-microfabrication process reported in this thesis. The Pyrex dies (or full wafers) can be bonded to a handle wafer using thermal compression, such that the probe tips are located at the interface of the wafer stack. In this way, electroless nickel will fill in the vias while the handle wafer prevents electroless nickel from mushrooming out beyond the 100 μm-diameter probe tips. In addition, the ability of the batch-microfabrication process to fill in vias with straight sidewalls should be tested. MEMS Langmuir probes fabricated from vias with straight sidewalls would have higher packing density compared to the probes with tapered sidewalls reported in this thesis.

MEMS Langmuir probes of different array sizes should be tested to determine whether pitch and/or packing density influence the measured plasma parameters. In this thesis, MEMS probes were fabricated in arrays containing 2×2, 4×4, and 5×5 probes, having a pitch of 4 mm, 2 mm, and 1.6 mm, respectively. Only one 2×2 array was tested in plasma and the results were reported in this thesis.

The signal to noise ratio (SNR) of the driving circuitry must be increased in order to improve the accuracy of the measurements of the MEMS probe. While the MEMS probe data provided measurements that were within the range of VTF's reported plasma parameters, they did not agree with the estimates of the electron density and Debye length from the conventional probe data. A higher SNR can be achieved by including filters and operational amplifiers in the MEMS probe driving circuitry. Also, the driving circuitry of both the conventional and MEMS probes should be placed inside a metal box. These improvements are particularly important if the future MEMS probes are fabricated with smaller diameters. Also, the driving circuitry should be operated with 2 V and 30 V bias voltages, which should provide better estimates of the plasma parameters compared to the 9 V and 18 V bias voltages utilized in this thesis.

The MEMS Langmuir probes must be tested as single probes to accomplish two goals: (i) provide data and estimates of the plasma parameters to optimize the triple probe driving circuit, and (ii) conduct fine spatial measurements of a plasma region – one of the key features of the technology we preliminarily characterized in this thesis. Finally, the MEMS probes should be tested under different plasma conditions to ensure that the tuning of the driving circuitry is sound. This can be accomplished by testing the probes in a different part of the plasma at VTF, or by performing the tests at other plasma facilities.

# 7 References

[1] L.C. Scalabrin and I.D. Boyd, "Numerical Simulation of Weakly Ionized Hypersonic Flow for Reentry Configurations," in 9th *AIAA/ASME Joint Thermophysics and Heat Transfer Conference*, San Francisco, CA, 2006, p. 1.

[2] K.M. Lemmer et al, "Using a helicon source to simulate atmospheric re-entry plasma densities and temperatures in a laboratory setting," *Plasma Sources Sci. Technol.* 18 (2009) 025019, pp. 1-8.

[3] R. Savino et al, "Plasma Radiofrequency Interactions Around Atmospheric Re-Entry Vehicles: Modeling and Arc-Jet Simulation," *The Open Aerospace Journal*, 3 (2010) pp. 76-85.

[4] *Lockheed Martin Trident II D5* [Online]. Available: http://www.lockheedmartin.com/products/TridentIID5.index.html

[5] U.S. Air Force (2010, July 7). *LGM-30G Minuteman III Factsheet* [Online]. Available: http://www.af.mil/information/factsheets/factsheet.asp?id=113

[6] J.P. Rybak and R.J. Churchill, "Progress in Reentry Communications," *IEEE Trans. Aerosp. Electron. Syst.*, vol. aes-7, no. 5, pp. 879-894, Sep. 1971.

[7] R. Lehnert and B. Rosenbaum, "Plasma Effects on Apollo Re-entry Communication," *NASA TN D-2732*, pp. 1-5, Mar. 1965.

[8] Encyclopedia Astronautica. *Soyuz 5* [Online]. Available: http://astronautix.com/flights/soyuz5.htm

[9] *Columbia Accident Investigation Board Report Volume 1*, Aug. 2003.

[10] Kennedy Space Center Frequently asked questions [Online]. Available: http://www.nasa.gov/centers/kennedy/about/information/shuttle_faq.html#10

[11] J. Mueller et al, "MEMS micropropulsion activities at JPL" in 2nd *International Conference on integrated Micro/Nanotechnology for Space Applications*, Pasadena, CA, 1999.

[12] J. Mueller, "Thruster options for microspacecraft: a review and evaluation of existing hardware and emerging technologies," AIAA97-3058, 1997.

[13] D. Collins et al, "Miniature, low-cost highly autonomous spacecraft – a focus for the new millennium," in *IAF papers* 95-U.2.06, Oslo, Norway, 1995.

[14] L. H. Krause et al, "Microsatellite missions to conduct midlatitude studies of equatorial ionospheric plasma bubbles," *Advances in Space Research*, vol. 36, no. 12, pp. 2474-2479, 2005.

[15] H.R. Bredfeldt et al, "The use of ion-probes in reentry physics," *Stanford Research Inst. Tech. Rept. 26*, 1965.

[16] J.L. Poirier et al, "Effects of the reentry plasma sheath on microwave antenna performance: Trailblazer II rocket results of 18 June 1967," *USAF Cambridge Research Labs. Rept. ARCRL-69-0354*, 1969

[17] W.E. Scharfman, "Operation of electrostatic flush probes in thin plasma layers," Stanford Research Inst., Contract 60192 under DAHC60-69-C-0008, 1969.

[18] W.L. Jones, Jr., and A.E. Cross, "Electrostatic Probe Measurements of Plasma Surrounding Three 25000 Foot Per Second Reentry Flight Experiments," in *The Entry Plasma Sheath and Its Effects on Space Vehicle Electromagnetic Systems*, vol. 1, NASA Special Publ. SP-252, pp. 109-136, 1971.

[19] B. W. van Oudheusden, "Compressibility Effects on the Extended Crocco Relation and the Thermal Recovery Factor in Laminar Boundary Layer Flow," *J. Fluids Engineering*, vol. 126, pp. 32-41, 2004.

[20] R.R. Costa et al, "Atmospheric Reentry Modeling and Simulation," *J. Spacecraft*, vol. 39, no. 4, pp. 636-639, 2002.

[21] J.A. Stillman et al,"MEMS Electric-Field Probes for Laboratory Plasmas," *J. MEMS*, vol. 18, no. 5, pp. 983-989, Oct. 2009.

[22] S. Y. Bae et al, "High Performance MEMS Micro-Gyroscope," *Proc. SPIE*, 4755, 556 (2002).

[23] J.Z. Wilcox et al, "Electron Induced Luminescence and X-ray Spectrometer (ELXS) Development: Progress Report," in *2003 Aerospace IEEE Conference*, paper #1138 reprinted in the conference proceedings, vol. 2, March 8-15, 2003, pp. 2/569-2/579.

[24] M. Young et al, "The Knudsen compressor as an energy efficient microscale vacuum pump," in *2nd NASNJPL Miniature Pumps Workshop*, Pasadena, CA, 2002.

[25] J. Qiu et al, "A Centrally-Clamped Parallel-Beam Bistable MEMS Mechanism," in *Proc. IEEE MEMS 2001 Conference*, Switzerland, 2001, p. 353.

[26] L. F. Velásquez-García et al, "A Micro-fabricated Linear Array of Electrospray Emitters for Thruster Applications," *J. MEMS*, vol. 15, no. 5, pp. 1260-1271, 2006.

[27] L. F. Velásquez-García et al, "A Planar Array of Micro-fabricated Electrospray Emitters for Thruster Applications," *J. MEMS*, vol. 15, no. 5, pp. 1272-1280, 2006.

[28] B. Gassend et al, "A Microfabricated Planar Electrospray Array Ionic Liquid Ion Source with Integrated Extractor," *J. MEMS*, vol. 18, no. 3, pp. 679-694, 2009.

[29] P. Pribyl et al, "Debye size microprobes for electric field measurements in laboratory plasmas," *Rev. Sci. Instrum.*, 2006 ©American Institute of Physics. doi:10.1063/1.2198730.

[30] D. R. Jenkins, *Space Shuttle: The History of the National Space Transportation System*. Voyageur Press, 2007.

[31] I.H. Hutchinson, *Principles of Plasma Diagnostics*, 2nd ed. Cambridge, United Kingdom: Cambridge University Press, 2005.

[32] F.F. Chen, "Lecture Notes on Langmuir Probe Diagnostics," in *Mini-Course on Plasma Diagnostics*, IEEE-ICOPS Meeting, Jeju, Korea, 2003.

[33] S. Chen and T. Sekiguchi, "Instantaneous Direct-Display System of Plasma Parameters by Means of Triple Probe," *J. Appl. Phys.*, vol. 36, no. 8, pp. 2363-2375, Aug. 1965.

[34] B.E. Cherrington, "The Use of Electrostatic Probes for Plasma Diagnostics – A Review," *Plasma Chemistry and Plasma Processing*, vol. 2, no. 2, pp. 113-140, 1982.

[35] V.I. Demidov, "Electric probes for plasmas: The link between theory and instrument," *Rev. Sci. Instrum.*, vol. 73, no.10, pp. 3409-3439, 2002.

[36] N. K. Katz, "Experimental Investigation of the Trigger Problem in Magnetic Reconnection," Ph.D. dissertation, Dept. Physics, MIT, Cambridge, MA, 2010.

[37] J.P. Freidberg, *Plasma Physics and Fusion Energy*, Cambridge, United Kingdom: Cambridge University Press, 2008.

[38] *Magnetic Reconnection Experiments on VTF: The Machine* [Online]. Available: http://www.psfc.mit.edu/research/physics_research/vtf/machine.html

[39] D.F. Beals, "Characterization of a Hot Cathode Helimak Plasma," M.S. thesis, Dept. Elect. Eng., MIT, Cambridge, MA, 1994.

[40] W.R. Fox, "Experimental Study of Current Driven Turbulence During Magnetic Reconnection,“ Ph.D. dissertation, Dept. Physics, MIT, Cambridge, MA, 2009.

[41] D.T. Moriarty, "Laboratory Studies of Ionospheric Plasma Processes with the Versatile Toroidal Facility (VTF)," Ph.D. dissertation, Dept. Nuclear Eng., MIT, Cambridge, MA, 1996.

[42] J.P. Holman, *Heat Transfer,* 10th ed. New York: McGraw-Hill, 2010.

[43] K.W. Iliff and M.F. Shafer, "Space Shuttle Hypersonic Aerodynamic and Aerothermodynamic Flight Research and Comparison to Ground Test Results," *NASA TM 4499*, Jun. 1993.

[44] *John F. Kennedy Space Center Frequently Asked Questions* [Online]. Available: http://science.ksc.nasa.gov/pao/faq/faqanswers.htm

[45] *Temperature Variations During Orbit and Reentry of the Space Shuttle* (2007, Oct. 25) [Online]. Available: http://www.columbiassacrifice.com/$D_temperature.htm

[46] N. Roxhet, et al, "A method for tapered deep reactive ion etching using a modified Bosch process," *J. Micromech. Microeng.* 17 (2007), pp. 1087-1092.

[47] L. Yan and J.A. Woollam, "Optical modeling of iridium thin film erosion under oxygen plasma conditions," *Dept. of Electrical Engineering Faculty Publications*, University of Nebraska, Lincoln, NE, 2004.

[48] A.R. Oliveira et al, "Electrical Characterization of Undoped, N- and P-Type Thermal Annealed PECVD SiC Films Deposited on Transparent Insulator Substrates," *ECS Trans.*, 2009 © The Electrochemical Society. doi: 10.1149/1.3183713.

[49] K. Thorne (Mar. 30, 2005). *Chapter 19: The Particle Kinetics of Plasma* [Online]. Available: http://www.pma.caltech.edu/Courses/ph136/yr2004/0419.1.K.pdf

[50] M. Mehregany and C.A. Zorman, "SiC MEMS: opportunities and challenges for applications in harsh environments," *Thin Solid Films* 355-356(1999), pp. 518-524.

[51] J. Zhang et al, "Electrical, mechanical, and metal contact properties of polycrystalline 3C-SiC films for MEMS in harsh environments," *J. Surf. Coat.*, 2007 ©Elsevier B.V. doi:10.1016/j.surfcoat.2007.05.007.

[52] M. Schlesinger, "Electroless Deposition of Nickel" in *Modern Electroplating*, 5th ed. M. Schlesinger and M. Paunovic, Eds. New York: Wiley, 2010.

[53] H.O. Ali and I.R.A. Christie, "A Review of Electroless Gold Deposition Processes," *Gold Bull.,* vol. 4, no. 17, pp. 118-127, 1984.

[54] *Transene Company, Inc. Bright Electroless Gold* [Online]. Available: http://www.transene.com/au.html

[55] L.T. Byrne, "Langmuir Probe Measurements in the Plume of a Pulsed Plasma Thruster," M.S. thesis, Dept. Mech. Eng., WPI, Worcester, MA, 2002.

[56] A.R. Hambley, "Diodes" in *Electrical Engineering Principles and Applications*, 3rd ed. Upper Saddle River, NJ: Pearson Education, Inc., 2005, ch. 10, sec. 10.2, p. 446.